UNIVERSITÀ DEGLI STUDI DI PADOVA

UNIVERSITA' DEGLI STUDI DI PADOVA

Dipartimento di Ingegneria Industriale DII

Corso di Laurea Magistrale in Ingegneria Aerospaziale

Development of an Active Themal Louver for CubeSats Controlled via SMA Actuator

Relatore: prof. Alessandro Francesconi

Dario Franchin 1154557

Anno Accademico 2018/2019

Acknowledgements

As a final step during the university path, this work of thesis was carried out thanks to the Erasmus+ scholarship granted by the Department of Industrial Engineering (DII) at the University of Padova; the funding helped to sustain the mobility period to Munich, Germany, and proved a fundamental contribution to lower the expenses.
A large acknowledgement is due to the hosting insitution, the Technical University of Munich (TUM) and its Faculty of Mechanical Engineering, for providing infrastructures, research material and supervision during the semester-long work and development. The final implementation and success of the project was possible thanks to the funding provided by the German Aerospace Center (DLR) and the Chair of Astronautics (LRT) at TUM.
A special thank you goes to the students, the researchers and the other people of LRT, and in particular to Florian Schummer, for the patience and the availability shown during the various steps of the work, and also for the helpful supervision through the whole stay at the Chair. The working environment was among the best ever experienced, and everyone's enthusiasm for space-related research and activities was contagious.
A big thank you goes to all the people who gave their support in some way and to varying degrees during this amazing experience, either from the next door at the department or from other countries, providing support and encouragement.
A final credit goes to the city of Munich itself, which I discovered day by day, during long explorations and walks among traditional Bavarian culture and modernity.

Abstract

In recent years, CubeSats proved to be valuable resources both for commercial and scientific purposes, leading to a significant technological development in terms of payloads and on-board instrumentation. The employment of more advanced technology usually implies a higher power consumption, and a consequently increased amount of waste heat. The typical, passive thermal control systems currently employed on small satellites, such as paints and coatings, may not be sufficient to guarantee a proper thermal stability, and therefore more elaborate and efficient systems are required. Based on the actuator IRESA (Intelligent Redundant Spacecraft Actuator), under development at the Chair of Astronautics of the Technical University of Munich, a new design for a compact, reliable, active thermal control system for CubeSats is proposed. IRESA is a shape-memory-alloy-based, low-power-consuming, high-force-per-unit-mass actuator embedded on a PCB, compatible with the lateral panel of a 1U CubeSat. IRESA produces a linear displacement of 3.5 mm exploiting the contraction of redundant SMA wires heated efficiently through the Joule effect; the displacement can be converted into rotation, allowing the actuator to operate a variety of subsystems. The design presented in this thesis for the TCS consists of an external louver moved by IRESA, capable of modifying the emissivity of a small radiator or regulate the power emission from the inner part of the satellite to space. The design of the louver was obtained studying the louvered surfaces employed over the last fifty years in larger satellites and adapting the geometry to the features of the actuator, with the general design driver of a minimum complexity for the assembly. Therefore, a configuration with a single blade was chosen and implemented; like its larger counterparts, it reaches and maintains every angular position between the fully closed and fully open conditions, performing a 90 degrees rotation; the linear displacement of the SMA wires is converted into rotation by a simple lever principle. The proposed subsystem meets the CubeSat Design Standard in terms of geometry and compatibility with a CubeSat of at least 2U. This work of thesis was carried out at the Chair of Astronautics of the Technical University of Munich, and the system is now in a prototype state: good results were obtained during the first functional tests, assessing the correct performance under laboratory conditions.

Sommario

Negli ultimi anni i nanosatelliti CubeSat si sono dimostrati validi strumenti per scopi sia commerciali che scientifici, portando ad un progressivo sviluppo tecnologico per quanto concerne payload e strumentazione di bordo. L'utilizzo di tecnologie più sofisticate è spesso legato ad un maggior consumo di potenza, e dunque ad un maggior calore di scarto: i tipici sistemi di controllo termico passivo finora impiegati in questi piccoli satelliti, quali vernici e rivestimenti termici, potrebbero non essere più in grado di garantire una corretta stabilità termica, rendendo necessari dei sistemi più raffinati ed efficienti. In questa tesi viene presentato un design innovativo per un sistema di controllo termico (TCS) attivo per CubeSat compatto, affidabile e basato sull'attuatore IRESA (Intelligent Redundant Spacecraft Actuator), sviluppato presso la Technical University of Munich. IRESA è un attuatore operante grazie a metalli a memoria di forma (SMA) e caratterizzato da un basso consumo di potenza e da una elevata forza per unità di massa; l'attuatore è integrato in una scheda elettronica compatibile con il pannello laterale di un CubeSat da una unità. IRESA è in grado di produrre uno spostamento lineare pari a 3.5 mm sfruttando la contrazione di coppie di fili di SMA riscaldate tramite effetto Joule; lo spostamento lineare può essere convertito in rotazione, consentendo all'attuatore una maggiore versatilità. Il design presentato in questa tesi consiste in un modulatore di emissione (louver) azionato da IRESA e in grado di regolare la potenza dissipata da un piccolo radiatore. Il design finale adottato deriva da uno studio dei sistemi preesistenti e utilizzati in satelliti di dimensioni maggiori durante gli ultimi cinquant'anni e da un adattamento della tecnologia alle caratteristiche dell'attuatore, mantenendo come direttiva principale una riduzione della complessità totale dell'assieme. Come conseguenza, si è scelto di implementare una geometria semplificata e costituita da un singolo pannello mobile, in grado di compiere una rotazione di 90 gradi ed azionato tramite un meccanismo a leva che sfrutta la contrazione fornita dall'attuatore. Il design presentato aderisce alla CubeSat Design Standard (CDS) in termini di ingombri, ed è compatibile con un CubeSat di almeno due unità (2U). Come risultato del lavoro, un prototipo è stato realizzato e testato presso la Cattedra di Astronautica (LRT) della Technical University of Munich, e buoni risultati sono stati ottenuti in termini di risposta del sistema in condizioni di laboratorio.

Contents

List of Figures

List of Tables

List of Acronyms and Symbols

TCS		Thermal Control System
1U, 2U, 3U		One-unit, Two-unit, Three-unit
CDS		CubeSat Design Standard
SMA		Shape Memory Alloy
SME		Shape Memory Effect
M_s, M_f, A_s, A_f	[K]	SMA characteristic temperatures
IRESA		Intelligent Redundant Spacecraft Actuator
ROM		Range Of Motion
HDRM		Hold Down and Release Mechanism
APM		Antenna Pointing Mechanism
SADM		Solar Arrays Drive Mechanism
LEO		Low Earth Orbit
ϵ_{eff}		Effective emissivity of a radiator
σ_n	$\left[\frac{\mathrm{W}}{\mathrm{m^2K^4}}\right]$	Boltzmann constant
ECSS		European Commitee for Spacecraft Standardisation
F_{ij}		View factor between surfaces i and j
ϕ	[deg]	Louver opening angle
q_{pl}	[W]	Payload waste heat
T_r	[K]	Radiator and payload temperature
IR		Infra-Red
ϵ_r		IR emissivity of the radiator
ϵ_l		IR emissivity of the louver
α_r		Absorption coefficient of the radiator in the visible spectrum
α_l		Absorption coefficient of the louver in the visible spectrum
θ	[deg]	Solar radiation incidence angle
J_s	$\left[\frac{\mathrm{W}}{\mathrm{m^2}}\right]$	Solar power per unit area
d	[m]	Total stroke used in the design
D	[m]	Distance between the axes of the hinges of the louver
PEEK		Polyether Ether Ketone

1 Introduction

1.1 Small satellites and new spacecraft technologies

Originally born in the early 2000s as research and educational tools, miniaturised satellites have been attracting increasing interest over the last years, and they are now starting to be employed also as low-cost resources for a wide range of space missions, both from a scientific and a commercial point of view.
The reduction in volume and mass allows for these satellites to be placed into orbit in large quantities with a single launch: up to a hundred picosatellites can be stored in one single fairing, and be successfully deployed in orbit.
These satellites are defined as picosatellites but they are usually referred to as CubeSats, due to the fact that the standard size of these spacecrafts is enclosed in a small cube of 10x10x10 cm, with a maximum mass of 1.33 kg. Larger variants based on this standard are also widespread and regulated in a precise way. Their external geometry consists substantially in a multiple of the cubic, fundamental unit, which takes the name of 1U (one-unit) CubeSat: the larger variants get the intuitive name of 2U, 3U, 6U or 12U CubeSats, in which the digit represents the number of repetitions of the fundamental unit. An example of CubeSats of different sizes is shown in figure 1.1.

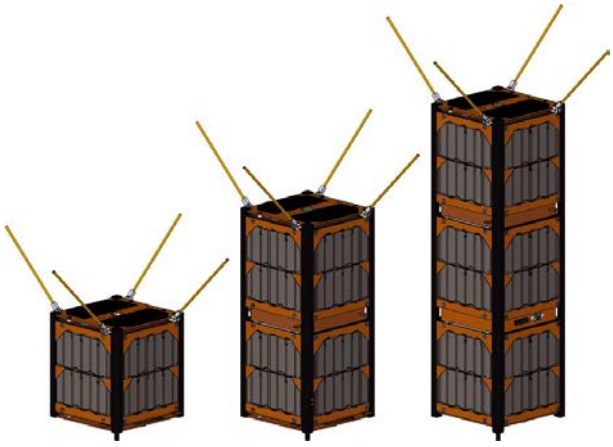

Figure 1.1: Three different variants of picosatellites; from left to right, a 1U CubeSat (approximately 10x10x10 cm), a 2U CubeSat (appr. 10x10x20 cm) and a 3U CubeSat (appr. 10x10x30 cm). Digital image, figure from published paper. Bedington, R. et al. (2016). *Nanosatellite experiments to enable future space-based QKD missions*

As CubeSats grow in popularity and range of use their complexity grows as well, thus making the miniaturisation and the adaptation of the traditional technology

employed in the last decades on larger spacecraft necessary for the future development of these small satellites. The main challenge in the design process lies in obtaining an acceptable performance while ensuring a low power consumption and a low mass for the system; some components typical of larger satellites and with long flight heritage do not show good adaptability when miniaturised, therefore new solutions are constantly implemented, tested and sent into orbit, confirming the still important role of CubeSats as technology demonstrators.

Innovative technologies based on new generation materials play a fundamental role in the implementation of these solutions. As addressed in the next sections of this thesis one class of smart materials in particular, referred to as shape memory alloys (SMA), fits perfectly in the segment of light weight, low mass and low power consumption technology. After a general introduction on the main physical properties of shape memory alloys, given in section 2, the new generation actuator for CubeSats IRESA is presented in section 3: in the current version IRESA is capable of a smooth, high force output, providing both linear displacement and rotational motion depending on the specific necessity.

The core of the thesis is dedicated to the development of an active thermal control system (TCS) for a 2U CubeSat based on the IRESA actuator, proving the good suitability and functioning of the mechanism. Sections 4, 5, 6 and 7 cover the whole development of the subsystem, starting from the general requirements of the the technology and later focusing on the progressive definition of the design, ending with the description of the produced prototype and the first functional tests.

Section 8 briefly summarises the various activities conducted and the achievements obtained, also providing a short insight on a possible evolution of the design, showing the versatility of the subsystem over a wide range of applications and configurations.

1.2 CubeSat Design Standard (CDS)

The CubeSat Design Standard (CDS) is the fundamental regulation to be adopted when designing a payload or a subsystem for a CubeSat, in order for the satellite to obtain the necessary approval and be successfully deployed into orbit [1].

The standards contained in the CDS refer to various aspects, such as dimensions, structural properties, type of materials, telecommunications systems and electric and electronic components. The set of regulations is fundamental due to the particular deployment procedure of CubeSats, shown in figure 1.2: before the launch, these small satellites are stacked inside housings which are part of the deployment system, and they remain in this enclosure for all the different ascent phases of the launch vehicle.

Only when the orbital altitude is reached a panel opens at one end of the deployer, and one ore more satellites are pushed out via the action of a spring-preloaded platform at the bottom of the enclosure. It is fundamental that a satellite does not cause any failure during the deployment procedure, for example by remaining stuck inside the enclosure. This particularly negative situation is avoided by leaving a proper empty space at the edges of the satellite, where aluminum structures (defined as rails) are placed in order for them to slide on matching metallic tracks inside the deployer. These aluminum elements are also useful in providing the necessary structural strength to the satellite. It is very important to adhere to the specified dimensions when designing a CubeSat structure or any subsystem with one or more protruding elements, otherwise the procedure of deployment might be impaired and one or more satellites could be lost before the beginning of the operations.

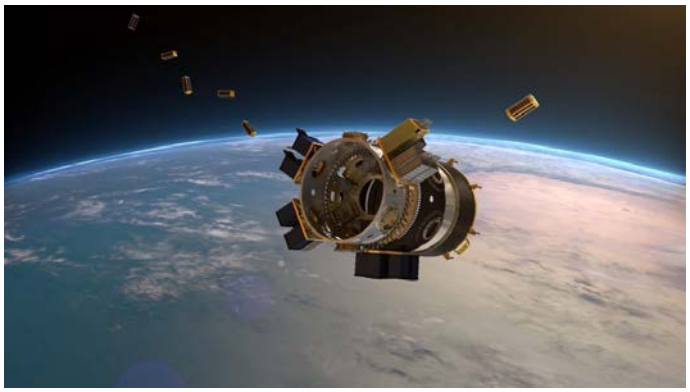

Figure 1.2: A complete deployment system by SpaceX with many deployers attached, rendered during the release of the satellites into orbit. Digital rendered image. Released by SpaceX. 2018.

Element	Direction	Dimension [mm]
Satellite body	X	113
Satellite body	Y	113
Satellite body	Z	227±0.2
Edge rail	X	8.5
Edge rail	Y	8.5
Edge rail	Z	227±0.2

Table 2: The dimensions for a 2U CubeSat as specified by the CDS.

This section outlines the main standards regarding the maximum size of a pico-satellite in the three dimensions of the external envelope in order to be qualified as a 2U CubeSat. The standard dimensions for the specified type of satellite are reported in figures 1.3 and 1.4, and also in table 2 (with respect to the frame of reference reported in the picture, as specified in the CDS).
The design of the subsystem reported in this thesis complies with the dimensions reported in this section, both in the Z direction and in terms of protrusion outside the rails.

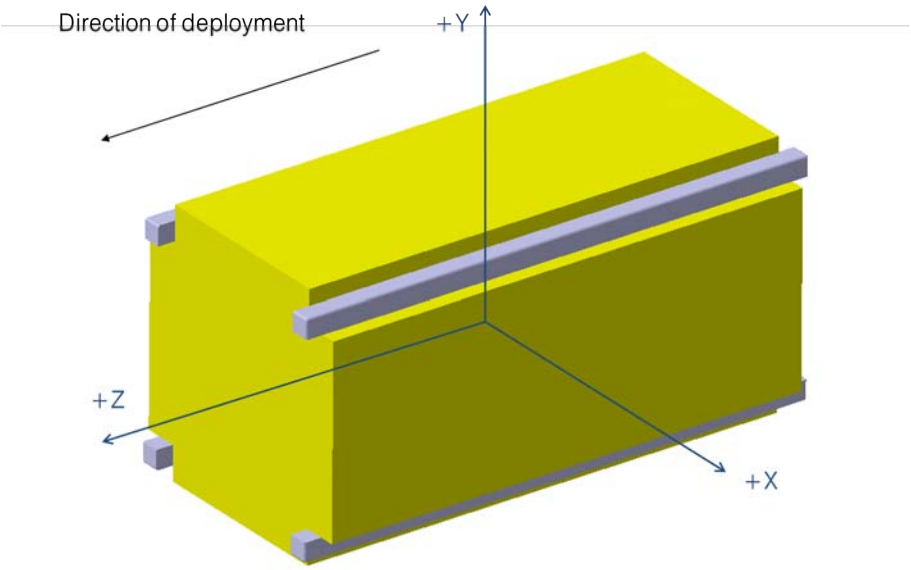

Figure 1.3: A simplified 3D model of a 2U CubeSat, showing the frame of reference specified by the CDS; the +Z axis direction coincides with the direction of deployment.

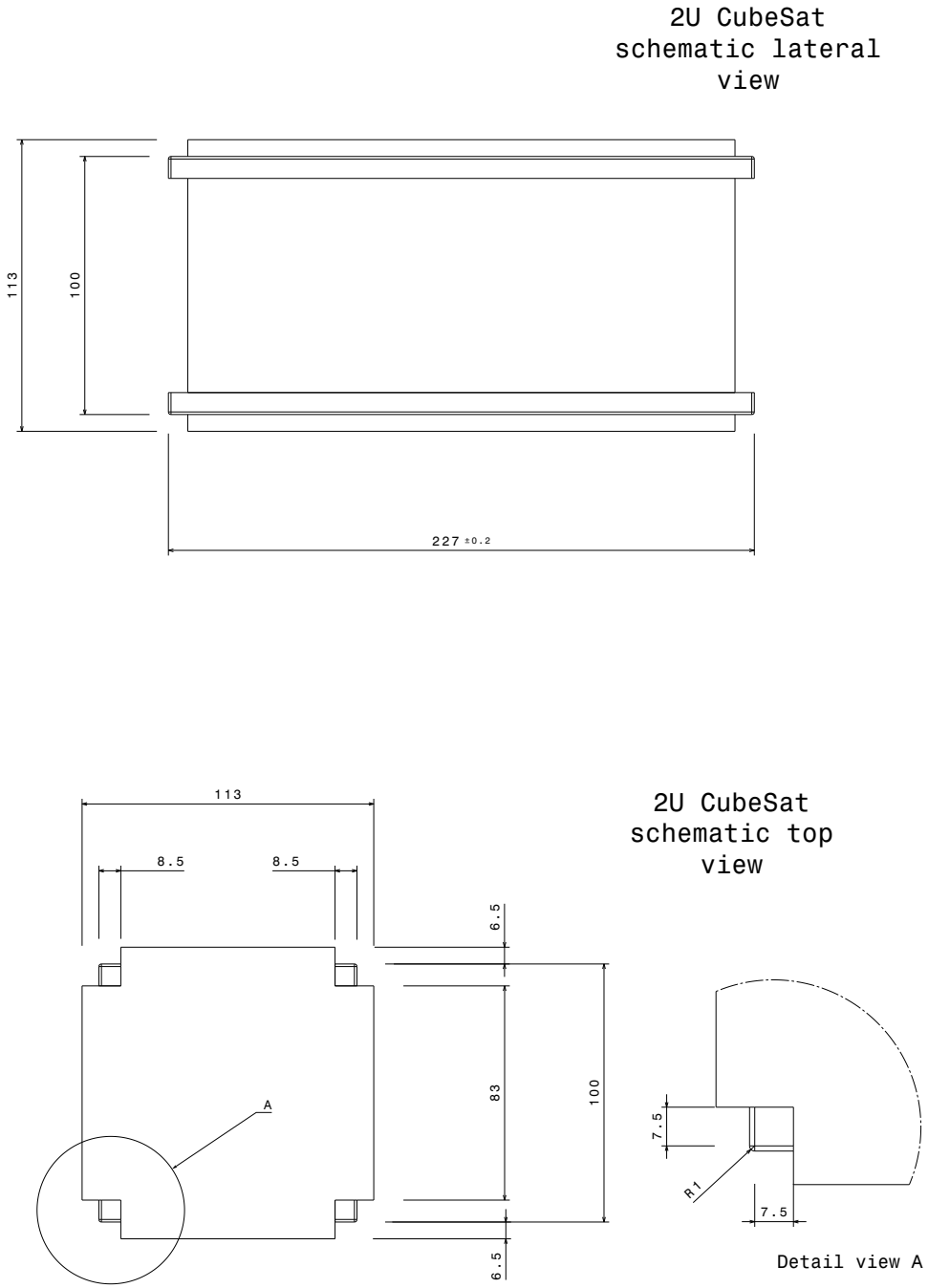

Figure 1.4: A schematic and simplified lateral and top view of a 2U CubeSat, reporting the relevant dimensions specified in the CDS.

2 Shape memory alloys

2.1 Introduction and history

Shape memory alloys (SMA) are a class of metals which exhibit a large strain recovery when undergoing the proper thermomechanical cycle. This phenomenon is often referred to as shape recovery, and it occurs even when high loads are induced inside the material, therefore conferring to these alloys an important role as sensors and actuators characterised by high actuation energy densities [2]. The employment of these materials is now common in many industrial sectors and applications [3, 4]: SMA-based mechanisms or devices are found in the aerospace [5, 6, 7] and the automotive [8] industries, in electronics (often in combination with MEMS technology) [9], in medicine and surgery [10, 11] and in biomedical engineering [12].
New studies are also being conducted in order to integrate these materials in structures and lightweight frames both in the constructions field and in objects designed for everyday use, in order to obtain new ways of sensing deformations in the material [13] and also to actively modify the physical properties of the structure itself, increasing its stiffness or exploiting the damping abilities offered by SMAs [14, 15].
Despite being a phenomenon known since the end of the 19th century, the shape recovery exhibited by particular alloys was not exploited until the second half of the 20th century: in 1963 Buehler found that an alloy formed by nickel (Ni) and titanium (Ti) could display a significant strain recovery when undergoing a specific thermal cycle, and they studied the unique properties of the material in detail, generating interest and causing a gradual diffusion of the technology in the aforementioned technological fields [2]. The nickel-titanium alloy was called NiTinol, and its characteristic behaviour was since then commonly referred to as shape memory effect (SME).

2.2 Physical properties of shape memory alloys

The peculiar shape memory effect of shape memory alloys is possible due to the transformations which take place in the microscopic structure of the material when an external solicitation such as a temperature variation or a mechanical stress (or a combination of the two), is applied: in the case of shape memory alloys the thermal and the mechanical fields are closely connected, and they exhibit a strong mutual influence on each other. More in specific, the simpler and more known variant of shape memory effect occurs when a mechanical stress is applied on the material and

a consequent rearrangement is induced in the atomic structure, and the induced modifications are subsequently canceled by a temperature increase in the material [16]. Before proceeding with the analysis of the various phenomena occurring during the transformations, it is useful to provide definitions for the different phases found during the thermo-mechanical operative cycle. The stable phases of SMAs are defined using a terminology similar to the one used in metallurgy to define the different forms of steel.

Austenite is the phase of an SMA which is stable at higher temperature, and it is characterised by a cubic crystalline structure. It is the phase with the highest symmetry, and it is unique for the specific material, meaning that only one austenitic structure variant is possible, being it formed in the same way during each thermal cycle the material undergoes.

Martensite represents instead the phase of the material which is stable in colder conditions, being it obtained from an austenitic structure after a temperature decrease. With respect to austenite, martensite is characterised by a lower symmetry in the crystalline lattice. When formed in absence of external loading, martensite is not macroscopically distinguishable from the original austenite because only small rearrangements occur at atomic level, slightly modifying the angles and the atomic distances inside the lattice; due to these small rearrangements and the subsequent reduction in the order of the lattice many different variants can be formed during the transformation and are equally possible and stable. Therefore, the martensite which forms from austenite due to a simple temperature decrease in no load conditions is a random mix of variants that coexist inside the material, and it is defined as twinned martensite.

The peculiar shape memory effect cannot not occur unless an additional transformation, called de-twinning process, is induced in the SMA. This transformation, which generates a new variant of martensite called de-twinned martensite, is activated when a sufficient external load is applied to the SMA; under the effect of loading the low-symmetrical, mixed structure of twinned martensite is stretched, resulting in a macroscopic deformation of the SMA. The amount of strain attainable by NiTinol in this phase is up to 8%, and this large deformation occurs at a nearly constant stress in a similar manner to how plastic deformation occurs in traditional metals, and therefore this peculiar phenomenon is defined pseudo-plasticity. Unlike plastically-deformed metals, though, the induced strain is completely recovered by the material when the temperature is increased and austenite is formed again.

Figure 2.1 shows a complete thermo-mechanical cycle of an SMA in a stress (σ)-

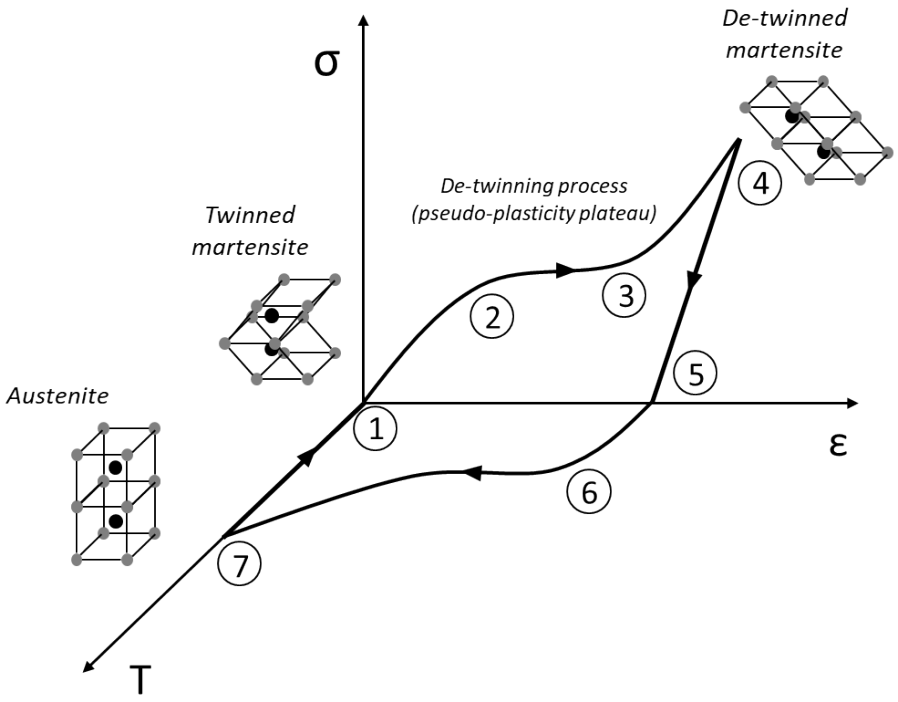

Figure 2.1: A complete thermo-mechanical cycle of an SMA in the stress-strain-temperature space.

strain (ϵ)-temperature (T) space. Point 1 is characterised by zero stress and strain and by a temperature at which twinned martensite is the stable phase. Following the curve and moving at constant temperature on the $\epsilon - \sigma$ plane towards point 2, the first, linear elastic phase of martensite is encountered (interval 1-2), where twinned martensite behaves as a normal metal with a given Young's modulus. At point 2, a sufficient stress to trigger the de-twinning process is reached, and the pseudo-plastic behaviour is dominant in the following interval 2-3, due to the aforementioned stretch and rearrangement in the microscopic lattice.

The process is complete when point 3 is reached, and only de-twinned martensite exists in the material, therefore a second elastic behaviour is displayed in the following interval 3-4. Point 4 represents the yield point of martensite at the given temperature, and a further increase in the imposed stress beyond this threshold would cause irreversible plastic deformation of the SMA. Along the unloading phase (interval 4-5) the material retains the acquired pseudo-plastic deformation, only recovering the second, elastic portion of the total strain, and at point 5 the material is still formed entirely by de-twinned martensite.

Maintaining a zero load, the temperature is then increased in interval 5-6, up to the

point where martensite is no longer stable and the conversion into austenite starts, continuing in interval 6-7. The transformation is complete at point 7, and only austenite exists in the material. If the temperature is gradually decreased and no external load is imposed, austenite is progressively turned into twinned martensite (interval 7-1), reverting back to the initial condition at point 1.
The cycle of figure 2.1 is a generic curve which covers different states of the material, and in which all the parameters are changed while following the path from 1 to 7. Figure 2.2 shows instead a temperature-deformation curve obtained for a constant stress value, and it displays the typical hysteretic nature of the SMA transformation. This plot highlights four important values of temperature which are determinant to characterise the cycle of a specific alloy; these temperatures are defined as follows:

- M_s (martensite start) is the temperature at which the transformation from austenite to martensite starts;
- M_f (martensite finish) is the temperature at which the conversion into martensite is complete; M_f is of course lower than M_s, being on the branch of the curve representing the cooling process;
- A_s (austenite start) is the temperature at which the transformation from martensite to austenite starts;
- A_f (austenite finish) is the temperature at which the material is only composed of austenite; A_f is higher than A_s, being on the opposite branch of the curve, associated with the heating process.

The vertical axis of the plot of figure 2.2 reports the evolution of the macroscopic deformation ΔL during the cooling-heating process: deformation is maximum when the material is in its martensite form and it is fully recovered (i.e. zero value for the deformation) when austenite is formed due to the temperature increase. The knowledge of these temperatures is fundamental for every application based on SMAs, since the SME can only occur in the specific temperature range determined by M_f, M_s, A_s and A_f. The values of the characteristic temperatures of the transformation is not fixed, but it is largely influenced by the amount of stress to which the material is subject. Figure 2.3 shows in a schematic way the effect of different stress levels on the hysteretic curve for a Ni-Ti SMA.
As shown in figure 2.3, different stress levels produce a variation both in the characteristic temperatures and in the maximum strain achievable during the cycle. In

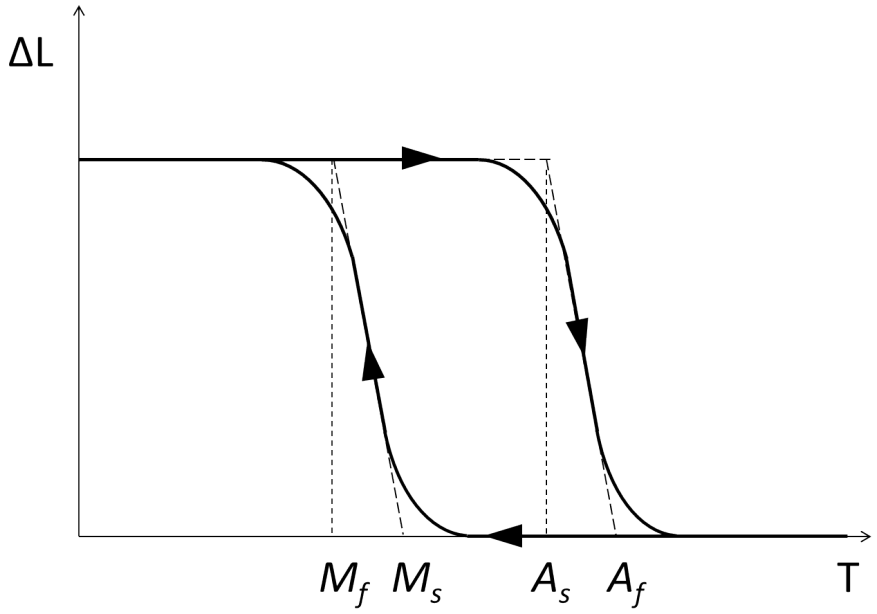

Figure 2.2: The hysteresis curve typical of an SMA thermo-mechanical cycle, in which the most important temperature values are reported; the deformation ΔL occurring in the material corresponds to the elongation attained after a complete conversion into martensite, while a value of zero for the deformation indicates a recovered shape in full austenite structure.

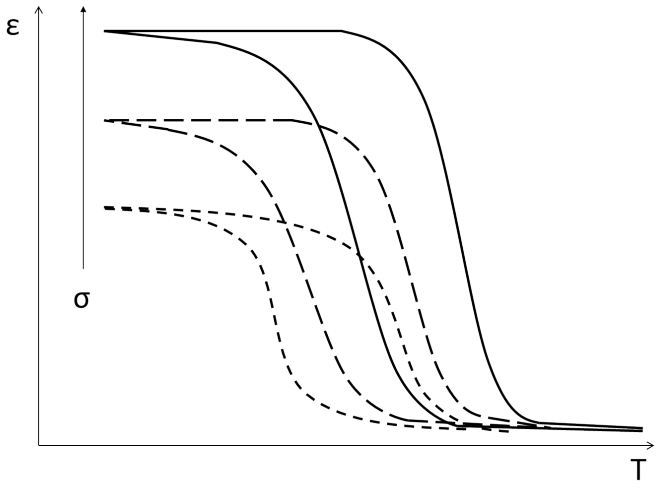

Figure 2.3: The effect of different stress levels on the SMA cycle.

particular, an increase in the applied stress causes an shift of the curve to the right, causing an increase of all the characteristic temperatures: this means that the cycle occurs at higher temperatures when subject to a higher stress. The increasing applied stress also causes a stretch of the curves along the ϵ axis, therefore meaning that the material can attain larger deformations during the de-twinning phase of the martensite transformation.

2.3 One-way and two-way shape memory effect

The shape memory effect explained in the previous section is an intrinsic property of every SMA which undergoes a mechanical and thermal cycle in the proper stress and temperature range, and it is often referred to as one-way shape memory effect: one-way SME refers therefore to the ability of the material to recover the large induced strain transforming from de-twinned martensite to austenite. The second part of the cycle, though, is not possible unless an external solicitation is applied in order to return to the strained, de-twinned martensite condition.

However, it is possible under particular circumstances to achieve an improvement in the one-way SME and have the material remember not only the austenite shape, but also the martensite one: this effect is called two-way shape memory effect, and it allows to switch between the hot and the cold shape merely by changing the temperature, achieving also in this case the large strain associated to the detwinning process. The two-way SME is obtained for a specific SMA by a long thermal training, which consists in a high number of cycles between the two extreme conditions.

Even if a two-way SME is not the final goal, a phase of thermal training shows positive effects for every SMA, even when operating with the simpler one-way SME; a period of thermal training allows for a stabilisation in the transition temperatures and in the composition of the martensite phase cycle after cycle, improving the repeatablitiy of the transformation and providing a more precise output when the SMA is used as a sensor and actuator. Figure 2.4 presents the typical, simpler cycle of the two-way SME, providing also a scheme of the corresponding shape variation of the material at the main points of the curve.

The two-way SME, despite more difficult to achieve, allows for a further simplification in the working principle of an SMA-based mechanism, since mechanical complexity is taken to the minimum. In this case, the control system only needs to regulate the temperature of the material to obtain the required output in terms of displacement or shape modification, and no other components such as springs or

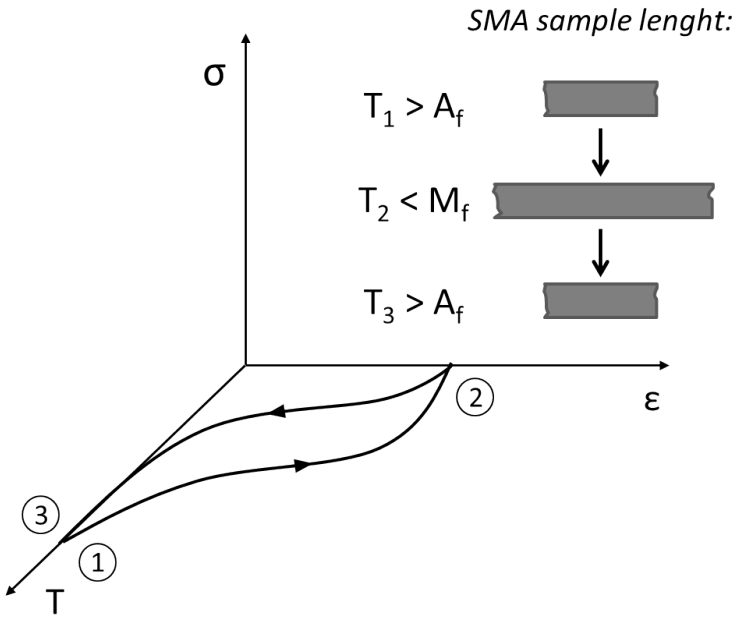

Figure 2.4: The thermal cycle associated to the two-way SME, in which no external stress is involved in the transformation from austenite to de-twinned martensite, and the material switches automatically between the contracted and elongated shapes.

loading sources are needed.

3 IRESA actuator and possible applications

This section contains an overview of IRESA (Intelligent Reduntant Spacecraft Actuator), a small, SMA-based actuator built upon the one-way SME presented in section 2. The general features of the device, such as its mechanics, design and performance are presented in this section, together with the adopted control strategy. The open possibilities for IRESA as a spacecraft mechanism are then introduced, presenting preliminary calculations and design options for every application.

3.1 Mechanical description of IRESA

IRESA is a compact SMA actuator developed in conjunction by the research center Forschungsgemeinschaft Werkzeuge und Werkstoffe e.V. and the Lehrstuhl für Raumfahrttechnik (LRT, Chair of Astronautics) of the Technical University of Munich (TUM).
It is designed to be compatible with the side panel of a 1U CubeSat following the aforementioned CDS regulations, and to operate efficiently while taking up the minimum amount of space; the current version of the actuator is entirely contained in a 80×30×8 mm envelope. The CAD model of the actuator, on which the entire work contained in this thesis is based, is presented in figure 3.1 together with a simplified scheme of its working principle. The actuator operates taking advantage of the one-way shape memory effect provided by NiTinol wires which work in opposition to a bias (or return) spring: the action of the spring guarantees that the necessary de-twinning stress is applied on the material during the transition from austenite to martensite. The NiTinol wires are shorter in their austenite shape, and are elongated when the spring has completed its stretching action. Therefore, the contraction phase of the cycle is triggered by an increase in the temperature of the material, and the subsequent elongation phase is obtained by letting the wires cool in combination with the effect of the spring.
The design requirement imposed to the actuator in terms of available displacement corresponds to a nominal stroke of at least 3.5 mm [18]; this minimum value is guaranteed by considering a larger displacement of 3.85 mm during the design process, in order to counteract possible tolerances and production imperfections. The number of achievable actuation cycles for an SMA is strongly dependent on the amount of strain taken during operations, and in particular the lifespan of the material is lower if the full 8% strain is exploited at every cycle. The operative goal and lifespan for IRESA is set to be of at least 10,000 cycles, and therefore a proper maximum 3%

strain is used at every actuation cycle. The total necessary length of the wires is 131 mm, split into two pairs in order to keep the dimensions of the total assembly contained.

As shown in figure 3.1, the total nominal displacement is obtained by connecting the wires (which are marked with the red colour in the CAD model) to a fixed bearing (light blue) and an intermediate, Z-shaped element (violet). The intermediate element is able to slide and it is connected to the second pair of wires, which are also connected to the floating bearing (blue), to which the output pin is rigidly attached. The total translation of the output pin corresponds to the nominal 3.5 mm stroke. The bias, or return, spring (marked in grey) acts on the floating bearing in opposition to the contraction of the wires.

An output disk (in yellow, on the back side of the PCB) is connected to the board and to the output pin: this mechanical element converts the linear translation of the pin into a nominal 180 degrees rotation through an arc-shaped channel. The rotation of the disk is obtained through the frictional sliding of the pin inside the channel. With this design solution, the capabilities of the actuator cover a wider range of possibilities, as both the linear displacement and rotation can be exploited to drive specific subsystems in a small satellite (a short overview on the possible scopes of IRESA as a spacecraft actuator is given in section 3.2).

As previously introduced, the parallel mounting of the two sets of wires allows to achieve a larger displacement output while keeping the size of the board and the actuator contained: the employment of additional sets of wires working with the same principle would allow for a larger displacement, but with the downside of an increased mechanical complexity of the assembly.

The pairs of wires are responsible for the redundancy of the system, which is one of the most important features of the actuator and one of the fundamental elements in space applications. Only one of the two wires in each set is actuated during the normal functioning of the mechanism, while the other is at rest. Redundancy proves fundamental in order to allow a correct functioning of the system in case of failure of one or more wires, and also to extend the operative life of the actuator when all the wires work correctly, since the main wires can be readily substituted by the redundant elements as soon as a significant deterioration is assessed through fatigue analyses. Moreover, if a pair of wires is completely impaired due to external causes or to a failure in the electronics of the board, half the stroke is still achievable by operating the remaining pair.

The switch between a wire and its substitute in the pair can be performed without

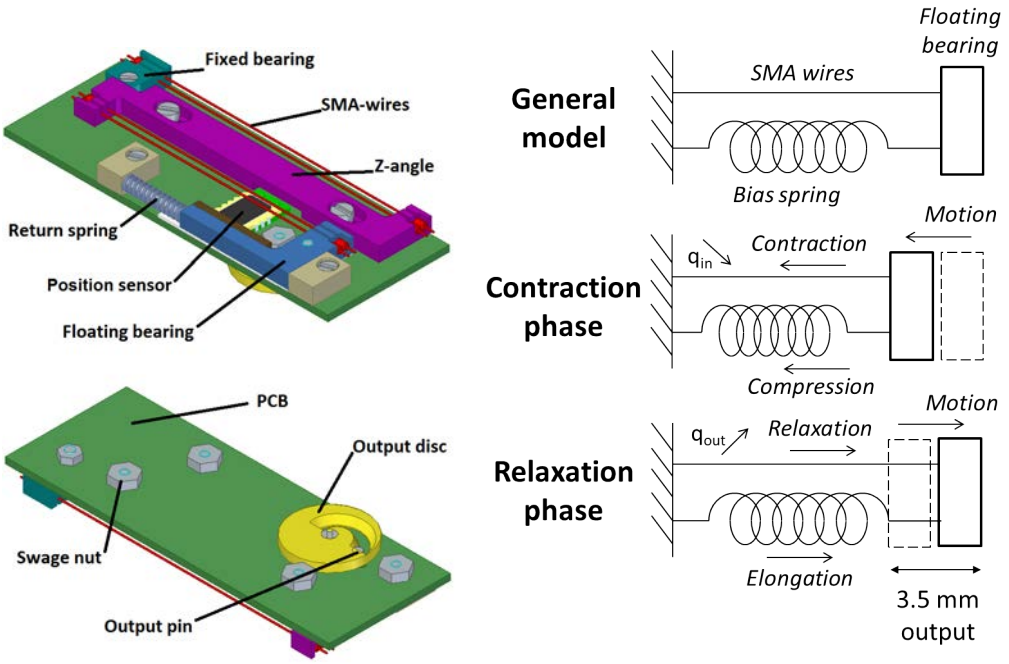

Figure 3.1: The CAD model of the actuator from both sides, with a reference on the main mechanical components (left) and the lumped-parameters model of an SMA-bias spring mechanism (right).

stopping the actuator from its service, therefore allowing for a smooth transition and for a continuous operation of the satellite.

Figure 3.2 shows the current version of the hardware of the actuator, highlighting the main elements presented in the previous, simplified CAD model, while table 3 reports the most relevant performance data.

As reported in [17] and [18], the tensile stress of wires in an SMA actuator can reach values up to 450 N/mm^2; the diameter of every wire in IRESA corresponds to 0.3 mm, for a cross section of approximately 0.07 mm^2, therefore allowing for a maximum output force of 31.5 N. Accounting for some safety margin before reaching the yield point, a maximum 28 N output force is achievable by the wire itself. When coupled to the bias spring, which acts in opposition to the SMA, a decrease in the effective, net force exerted at the output pin is experienced, and a total output force of approximately 19 N is available for servicing.

3.1.1 Actuation process and control strategy

The actuation method adopted for IRESA is one of the most common in SMA-based active applications, as a controlled Joule heating effect is used in order to change

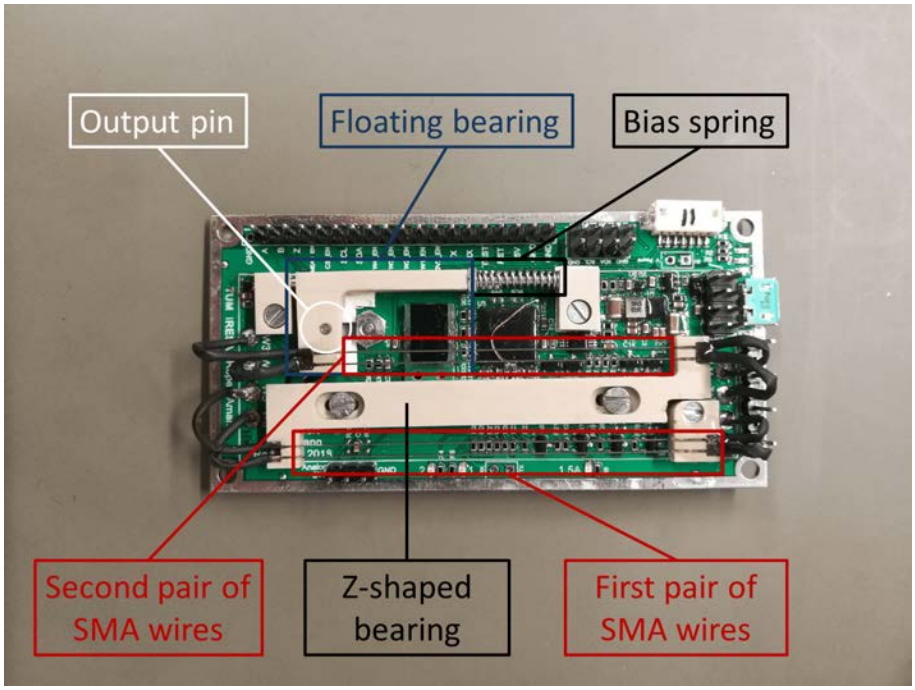

Figure 3.2: The hardware of the IRESA board used as a base for the development of the subsystem.

Property	Quantity	Unit
Total mass	22	g
Idle power consumption	125	mW
Power consumption to maintain a position in vacuum	400	mW
Power consumption to maintain a position in atmosphere	1800	mW
SMA wire diameter	0.3	mm
Available translational displacement	3.5	mm
Total available translational force	28	N
Net available translational force	19.1	N
Available rotation at the output disk	180	deg
Available moving torque	7.5	Nmm
Available holding torque	85	Nmm

Table 3: The most relevant performance data of IRESA.

the temperature of the wires during the normal operation of the actuator, and the amount of current flowing through the wires is regulated via pulse width modulation.

When operating in vacuum conditions, the only possible means of heat exchange are conduction and radiation, due to the lack of residual atmosphere: the wires exhibit conduction with the bearings at their extremities and at the same time they dissipate heat by emitting power from their outer surface; due to the small diameter

of the wires the external surface available for power dissipation is limited, and the temperature decrease of the material is slow.

During the heating phase the predominance of the input power over the scarce dissipation allows to raise the temperature of the SMA very quickly, achieving a complete contraction of the wire in 10 s: moreover, the reduced capability in heat dissipation allows to achieve this actuation speed with a small power consumption, in the order of magnitude of approximately 100 mW. The slower cooling process settles instead on a time interval of 90-100 s for a complete elongation. The asymmetry in the functioning of the system is typical of its employment in an atmosphere-free environment, while the behaviour is substantially opposite when the actuation takes place in laboratory conditions: in this case the prevailing heat exchange method is convection with the air, which efficiently removes heat from the wires and counteracts the provided input power; therefore, only higher actuation times are possible during contraction (in the order of 30-40 s) and with a higher power expense, especially when the conversion into austenite is almost complete and the temperature of the material is maximum. Convection also reduces the asymmetry of the system, because it allows a faster cooling phase when current is turned off, making the actuator complete its elongation in around 30 s.

The behaviour in absence of atmosphere remains the most relevant given the purpose of the actuator and its possible application in a satellite. An experimental curve representing a full actuation cycle obtained during testing procedures in a thermal vacuum chamber is presented in figure 3.3. The total displacement imposed to the actuator is slightly lower than the nominal 3.5 mm, settling on 2.85 mm. This plot clearly shows the functioning asymmetry in vacuum conditions, with a heating phase lasting around 10 s, a subsequent phase at constant temperature and a final cooling phase with a duration of approximately 80 s.

Conduction phenomena at the extremities of the wires are also responsible for a non-homogeneous temperature distribution inside the material, in which a temperature gradient persists during every phase of the actuation; the central portion of the wire is heated properly, while the ends are colder: this causes a decrease in the efficiency of the conversion from martensite to austenite, because the final portions of the wires always retain a non-zero martensite fraction. The main effect of the temperature gradient is the reduction in the total stroke obtainable from the actuator with respect to a condition of perfect insulation, thus proving the usefulness of keeping a safety margin on the 3.5 mm requirement.

The actuation process is driven by a contactless position sensor (marked in black in

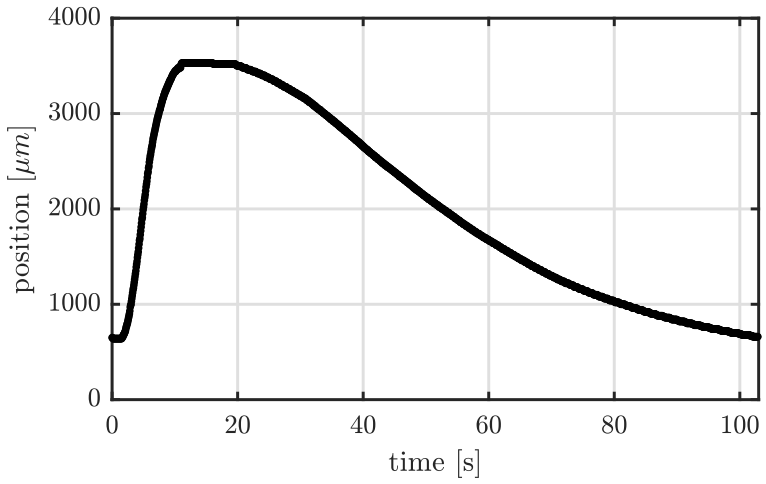

Figure 3.3: The position over time performance curve of a complete actuation cycle obtained in vacuum conditions.

the previous figure 3.1), which allows for a precision on the position of the floating bearing of 50 $\mu\Omega$ without filtering. The precision in the position control is enhanced to 1 $\mu\Omega$ when a proper filter is applied. In addition to the position sensor, other measurements are carried out during the actuation process, in order to target different aspects of the functioning of the board: temperature measurements are collected in different spots on the SMA wires in order to determine the thermal behaviour of the material, and a continuous measurement of the value of electrical resistance in the wires is collected and used in order to assess the health condition of the SMA, as explained in section 3.1.2.

3.1.2 Effect of fatigue on the performance

Electrical resistance is one of the most useful indicators of the condition of the SMA, and it gives precious information on the wear and the residual lifespan left for the material. In particular, the curves presented in figure 3.4 show how the electrical resistance follows a nearly-linear dependence on the martensite/austenite fraction inside the SMA, and therefore on the stroke produced as output by the actuator.
Observing the evolution of the curves in the interval 0-3.5 mm, it is possible to see that except for an initial and final inversion in the resistance variation the curves take the form of a line with negative slope, therefore the resistance decreases in the martensite-austenite transformation (i.e. the contraction of the wires). It is also interesting to observe how different parameters, such as the number of cycles underwent by the wire and the different operative stress levels affect the variation

of electric resistance over the total stroke. The curves also exhibit a hysteretic behaviour over a full actuation cycle, a phenomenon that is more visible where inversions in the slope occur.

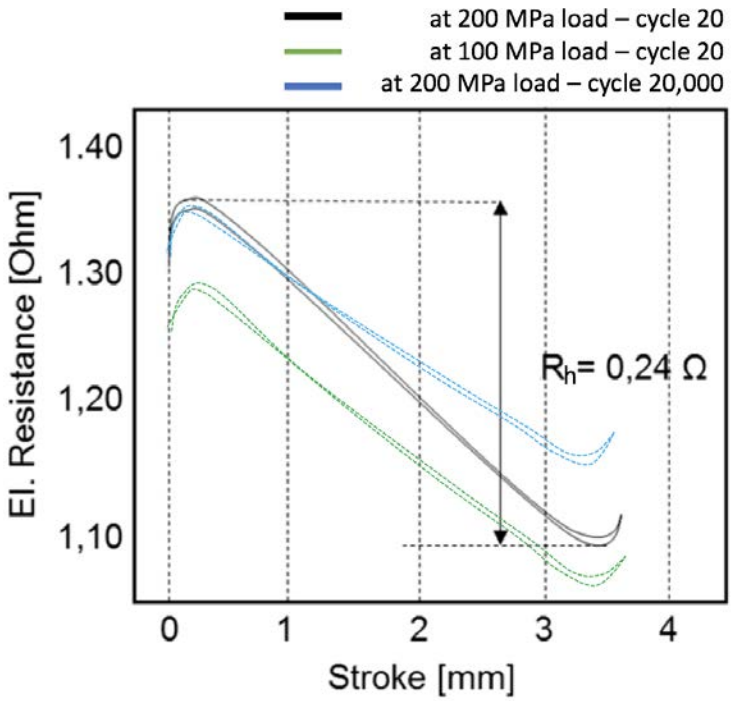

Figure 3.4: The curves of electrical resistance inside the SMA wires for different stress levels and different life periods.

Regarding the stress levels, the plot shows that a full actuation at the same cycle number and for different applied loads (in this case respectively 100 MPa and 200 MPa) exhibits a larger resistance variation as the stress increases; the initial and final values of resistance are also higher if the stress increases. This behaviour is linked to the elastic deformation that occurs in the wires in parallel to the SME, since a higher applied load also produces a larger restriction of the cross-section of the wire, enhancing the increase in electrical resistance.
At a fixed stress level, in this case 200 MPa, the number of actuation cycles plays a role in changing the slope of the curve, decreasing the total variation of electrical resistance between martensite and austenite, and also slightly decreasing the output stroke. This phenomenon occurs due to the deterioration of the material and the reduction in the efficiency of the shape recovery process due to the typical effects of fatigue: larger portions of the wire are no longer able to complete the conversion when the number of cycles increases, as microscopic fractures and cracks form in the structure of the alloy. A detection of this decrease over time allows for a good

estimate of the health condition of the specific wire, and it can be also used as a criterion to determine the best moment to switch to a new wire and terminate the operative life of the worn out one.

3.2 Possible applications for IRESA

This section provides a short overview on some of the most relevant applications in which IRESA could make the difference, reducing the complexity of the specific system and providing the necessary output in terms of motion or force, depending on the specific requirement.

3.2.1 Hold Down and Release Mechanism (HDRM)

Hold down and release mechanisms are used in space as a reliable mean of servicing for various deployable or detachable elements, such as solar arrays, antennas and booms. SMA-based mechanisms are suitable for this task, as they can either have an active role during the whole deployment, driving the process and being actively controlled through the entire operation [19, 20], or they can simply complete a switch between two different states providing a necessary degree of freedom to the structure to be deployed. SMARD and its evolution 2SMARD [23] are an example of SMA-based hold down and release mechanisms for CubeSats: these devices were developed at the Technical University of Munich and tested during the 19th iteration of the Rexus/Bexus programme, as an all-in-one actuator responsible for the deployment of both the four solar arrays of the satellite and the S-band antenna. After becoming the main mean of deployment in the MOVE-II (Munich Orbital Verification Experiment 2) 1U CubeSat, launched in December, 2018, the mechanism proved to work correctly performing the required orbital detachment of the deployable elements as expected.
IRESA could also be employed for a similar task, due to its features of compactness and integrability in the lateral panel of a satellite. In particular, the actuator could be used in its purely linear variant, as the only function needed would be to switch between the two configurations in order to disengage a fastening element; the deployable structure could then be opened properly by using a torsional spring mounted on the hinges. The actuator would therefore be required to operate correctly only one time, and the redundancy present in the design of IRESA could easily guarantee reliability to the subsystem.
Figure 3.5 contains a schematic concept of the HDRM system, showing the simple

functioning process. The sequence represents a side view of the lateral wall of the satellite (marked with the green color), which may be connected to or even incorporate IRESA; an external hook-like element (in black) is attached to the output pin instead of the previously presented output disk, and a matching element (in grey) is mounted on the inner face of the solar array.

The left part of the image shows the holding phase of the mechanism, which lasts from the final integration of the satellite to the moment of deployment into orbit; it is fundamental that the solar array remain in this position without any risk of premature disengagement, in order to avoid a premature end for the mission: the strong preload provided by the bias spring of IRESA guarantees that the floating bearing hold this position even under the effect of the typical loads and vibrations encountered during the ascent. When actuated, IRESA decouples the locking element from the hook by completing the contraction of the SMA wires, and in the later phase the array is free to rotate around its hinge. The preload of the torsional spring counteracts potential inertia and friction effects, thus opening the panel.

In this preliminary design the resetting ability of IRESA is not exploited, since the proposed design is based on a single release mechanism; however, if for any application other than solar arrays the spring-based and passive deployment system is replaced with an active element, and the panel is able to close again into the original configuration, new actuations of IRESA would allow for the HDRM to lock and unlock the deployable a large number of times.

3.2.2 Antenna Pointing Mechanism (APM)

CubeSats are usually equipped with both VHF/UHF and S-Band antennas in order to provide an uplink and a downlink (figure 3.6).

VHF/UHF antennas are thin, elongated, slender elements which are rolled up inside a proper housing during the launch and introduction into orbit, and are later released in the open condition when the satellite needs to start communicating; they remain open and protrude from the satellite, with no need of active control.

On the other hand, S-Band antennas are flat panels that are usually attached rigidly to the lateral surface of the satellite (they are referred to as patch antennas); these antennas are therefore able to communicate only if they are pointing in the correct direction for the whole duration or a portion of the overpass on the ground station; even when optimal attitude is maintained by the satellite, the link time is still a small fraction of the total the satellite spends above the local horizon of the ground

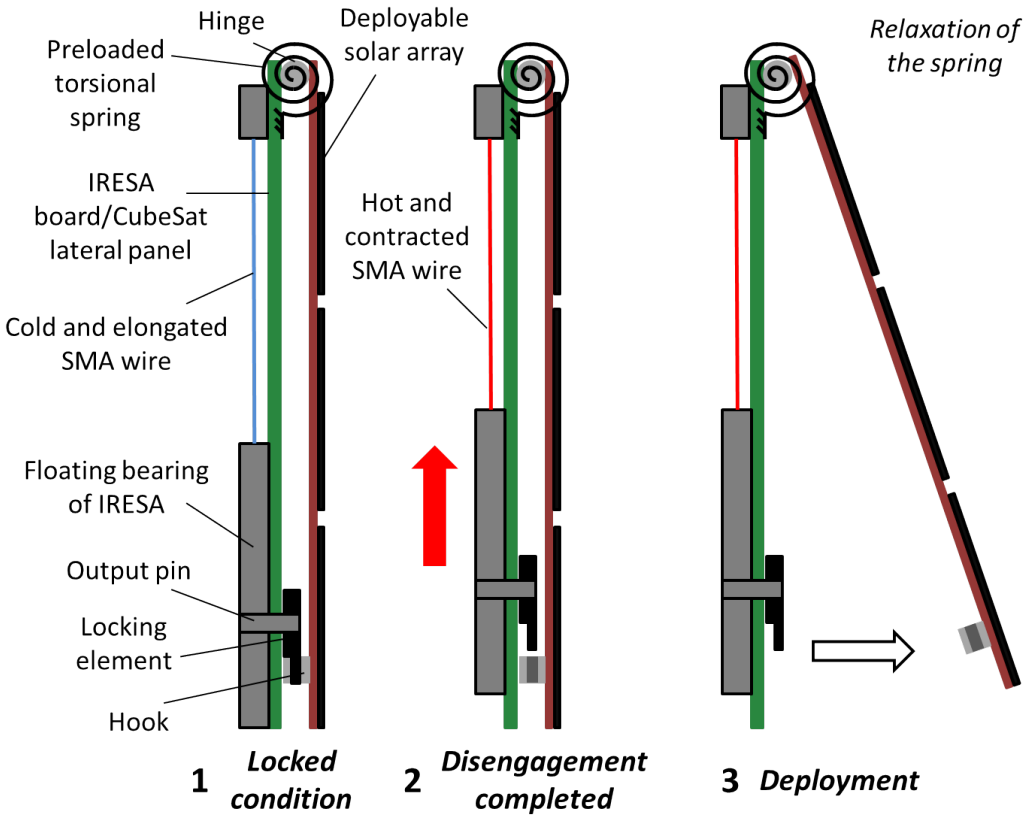

Figure 3.5: The different phases of the hold down and release procedure (side view of a lateral wall of a satellite): 1) the solar array is secured to the satellite wall during launch and immission into orbit; 2) IRESA is actuated and the locking system is disengaged; 3) the panel is deployed by the torsional spring at the hinge.

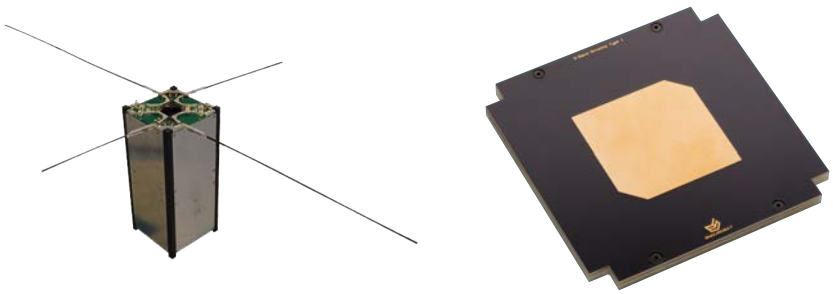

Figure 3.6: A 2U CubeSat with a deployed VHF antenna mounted on top (left). Digital image. ISIS. 2010; an S-Band antenna, with a flat geometry (right). Digital image. EnduroSat.

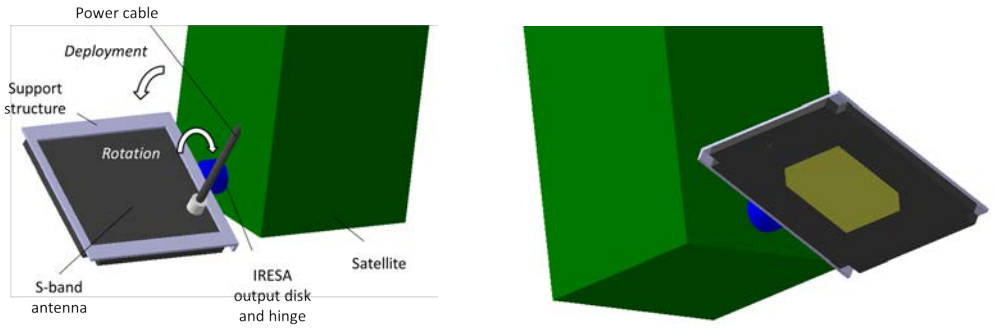

Figure 3.7: The preliminary concept of the deployment and pointing mechanism for an S-band antenna and its main elements (left) and the side to be pointed towards the ground station (right).

Parameter	Value	Unit
Earth radius	6378	km
Orbital altitude h_o	500	km
Orbital angular speed ω_{orb}	0.063	deg/s
True anomaly γ	17.51	deg
Angle above local horizon ξ	5	deg
Link availability time Δt_{link}	11	min
Total range of motion δ	135	deg
Required actuation angular speed $\omega_{pointing}$	0.39	deg/s

Table 4: The main parameters used for the preliminary calculations.

station.

Redundancy is helpful in this case, since mounting small antennas on each or many faces of the satellite guarantees communication even when a non nominal attitude happens, and prolongs the link availability window. The solution presented in this section is based on a different approach, which consists in mounting the S-band antenna on the external pin of the IRESA board, which is integrated in the lateral panel of the CubeSat, creating an antenna pointing mechanism (APM) able to provide a larger link time if compared to a rigid mounting. The parameters considered for this simple preliminary calculation are presented in table 4.

The orbit considered in this preliminary analysis is a LEO with an altitude of 500 km; from simple calculations derived from the equations for a circular orbit it is immediate to determine the visibility window of the satellite from a given point on the surface of the planet. Figure 3.8 contains a scheme of the orbit and show the geometrical quantities involved in calculations and contained in the table.

The satellite could theoretically start its communication process in the moment when

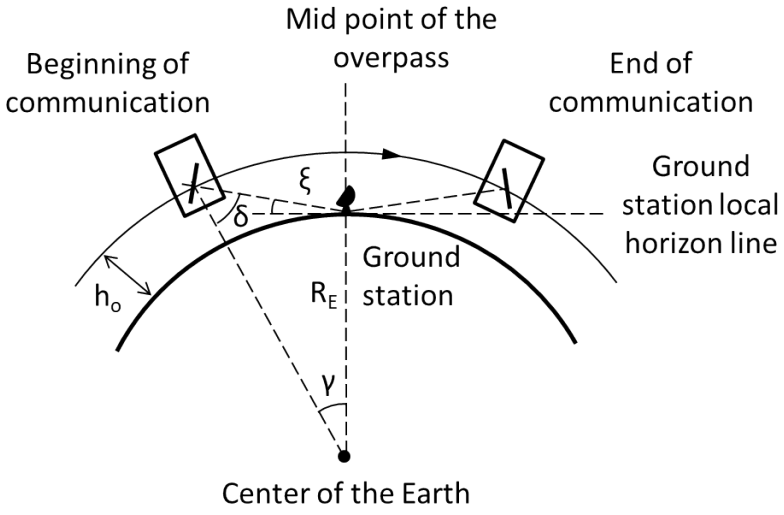

Figure 3.8: The portion of the orbit for which the mechanism should operate; the different values of the depicted parameters are listed in table 4.

the local horizon line is crossed along the orbit; due to atmospheric losses, though, an angle ξ of 5 degrees above the horizon must be reached before effective transmission. With reference to figure 3.8, simple geometry calculations yield the true anomaly value for the effective portion of the orbit, measured from the perpendicular line conducted through the ground station. The specific equations and the calculations carried out to obtain the results contained in the table are reported in appendix A. The expected range of motion (ROM) of 135 degrees and the pointing rotational speed of approximately 0.4 deg/s are compatible with the specifications of IRESA, which could therefore be considered as a mean of motion for such a system. Moreover, the high torque produced by the actuator can easily counteract the resistant torque generated by the cables of the antenna, which are usually thick and moderately flexible. The expected ROM for this type of application is compatible with the limited twist and deflection acceptable for the cables, since only a small deformation is imposed to the cable while the antenna rotates.

3.2.3 Solar Arrays Drive Mechanism (SADM)

A solar array drive mechanism (SADM) is a device used to optimise the functioning of solar arrays by moving and rotating them in order to be as perpendicular to the sun vector as possible: this allows for a maximum solar power impingement and therefore for a maximum power conversion by the solar cells.
A satellite can achieve this result by maintaining its attitude in such a way that the

rigidly deployed panels are oriented in the correct direction (sun-pointing satellite), or it necessarily needs a SADM to move the arrays independently on the manoeuvers of the spacecraft along the orbit: this configuration occurs, for example, when nadir-pointing or astronomical observation satellites are considered. Traditional SADMs can have one or two rotational degrees of freedom, depending on the necessity of the specific mission [21, 22].

IRESA could be suitable to operate as a single-axis mechanism, taking advantage of the rotation provided by the output disk and with a mounting similar to the one presented in section 3.2.2; the deployment of the solar arrays could be achieved even in this case as shown in section 3.2.1. Figure 3.9 shows the requirement in terms of rotation of the solar arrays for a nadir pointing CubeSat operating in a Low Earth Orbit similar to the one used in section 3.2.2, and in this case a sun-synchronous, midday-midnight orbit is chosen as an example.

The maximum rotation achievable from IRESA corresponds to 180 degrees, which is not enough to cover the whole sun-illuminated portion of the orbit, as seen in the picture; moreover, a maximum angle of 170 degrees should be considered in order to maintain a proper safety margin, especially if the disk operates with an uncertainty of $\pm$ 4 degrees (as reported in table 3) due to tribological effects. A good result could still be achieved though, increasing the efficiency of the solar arrays for the most part of the orbit exposed to sunlight. IRESA would be activated when the satellite is the position 1, and would continue to rotate the solar arrays until position 2 is reached. The portion of orbit crossing the shadow cone would guarantee a more than sufficient time to reset the actuator and bring back the arrays to configuration 1. In this case, the drawback of the limited ROM of IRESA is balanced by the possibility not to use a device such as a slip ring to transfer power between the satellite and the solar cells, and to employ a normal cable connection due to the limited twist it has to withstand.

3.2.4 Active Thermal Control System

A different application with respect to the previous mechanisms is introduced in this section, but it is later developed in the following sections in every aspect, being the central core of the thesis and the subsystem chosen to be designed and prototyped.

As an enhancement to the classical systems suitable for power dissipation in space, such as radiators, more advanced solutions can be adopted in order to increase the performance in terms of heat exchange and thermal stability of the satellite

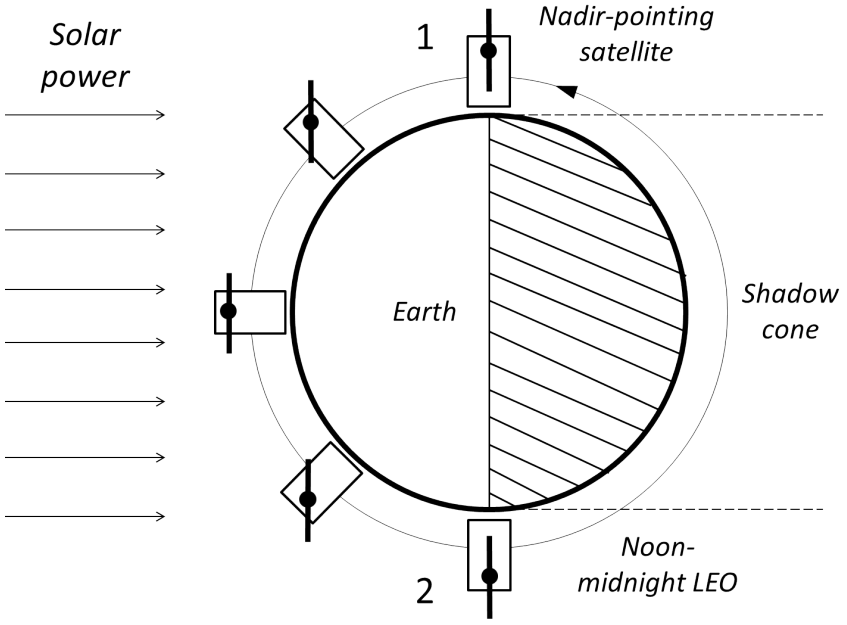

Figure 3.9: An example of employment of IRESA as a SADM: a sun-synchronous noon-midnight LEO requires the solar arrays to rotate by an angle of at least 180 degrees in order to properly track the sun during the illuminated region of the orbit.

or of a specific payload. Therefore, solutions as variable geometry radiators and louvers can be implemented in addition to the typical radiating surfaces in order to obtain a more versatile and adjustable behaviour from the system. Radiators with variable geometry are composed of one or more main emitting surfaces to which secondary, foldable panels or diaphragms are attached. These additional surfaces can be deployed or opened and they increase the total emitting surface, due to their good thermal connection with the radiator.

Thermal louvers work following a different principle, as they operate in a way similar to window venetian-blinds [24]: a series of thin, metallic blades is mounted in front of the radiating surface and hinged to a support structure; the mobility of the blades allows for a modification of the radiating properties of the system, leaving a different portion of the surface exposed to the external environment.

Shape memory alloy-based systems already exist and are employed in missions involving these means of control system [25], given the strong dependency of these materials on temperature variations, making them suitable to implementations in passive control loops; shape memory alloys can be programmed to operate in a determined temperature range, thus a good connection with the thermal control surfaces guarantees an efficient response from SMA-based actuators. The scope of

this thesis is instead to prove the effectiveness of IRESA in one of these contexts, by designing a thermal subsystem for a CubeSat based on louvers and operated by the SMA actuator. This design process is continued as the main topic of this thesis: a general overview on thermal control systems is given first, to contextualise the later design choices, and the complete design process is later addressed. The main focus is pointed towards the mechanical part of the project, showing the results of the design process and the behaviour of the first prototype.

4 Thermal control systems based on louvers

This section contains the considerations connected to the thermal behaviour of the subsystem, as well as the definition of the main requirements deriving both from thermal and mechanical aspects of the system. Due to the characteristics of the actuator, and the necessary adaptations that are required in order to make the classical design of louvers suitable for a CubeSat application, the thermal and mechanical fields are often addressed together in this section and in the following ones, as the design process cannot be completed overlooking one or the other aspect, and a design choice taken to fulfill a requirement in one of the fields has important consequences on the other.

4.1 Description and state of the art for louvered surfaces

The general structure of a thermal louver consists in a classical, high emissivity radiating surface covered by thin foils or blades, separated from the radiating area by a small offset and hinged to an external support structure; the blades are therefore able to rotate around one axis and expose a different portion of the underneath surface to the open space. This process is often referred to as control of the effective emissivity of the surface [26], mainly due to the change in the view factor between the radiator plate and the facing blades. The effective emissivity ϵ_{eff} of a louver is defined as the ratio between the amount of heat dissipated by the system and the ideal power emitted by an equivalent black surface at an equal temperature:

$$\epsilon_{eff} = \frac{q_{diss}}{A\sigma_n T^4} \tag{1}$$

where q_{diss} is the dissipated power (in W), σ_n is Boltzmann constant (in $\mathrm{W/m^2k^4}$), A is the radiating area (in $\mathrm{m^2}$) and T is the temperature of the surface (in K). The effective emissivity depends of course on the angle at which the blades are open, as the main function of the system is to modify the power emission depending on the boundary conditions, but it is also an indicator of the effect of the structure of the louver itself on the underlying surface: even when in completely open mode, the louver and its supports create an obtrusion for the radiator, and part of the dissipated heat is trapped in the structure, thus reducing the performance of the system. More information on this problem is given in later sections, dealing with radiaton heat exchange.

Louvered thermal control systems possess a very long history of effective functioning

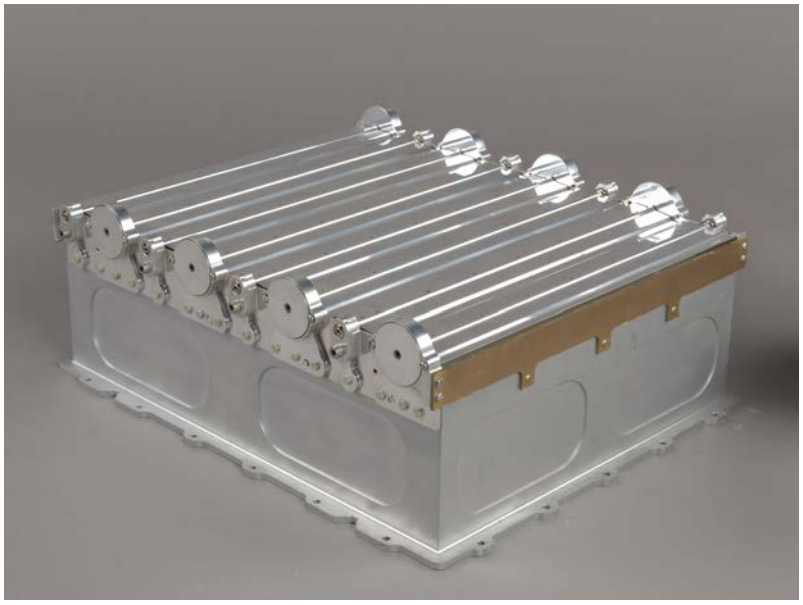

Figure 4.1: The classical structure of a louver designed for a large spacecraft, composed of several independently moved blades. Louvers, Temperature Control System, Mariner 2. Digital image. Smithsonian - National Air and Space Museum.

in space technology, having been employed in several missions in the last fifty years, such as Mariner, Pegasus, Voyager, Seasat and also the Global Positioning System (GPS). Figure 4.1 shows the louver system which was mounted on board the Mariner 2 spacecraft in 1962: this louver presents the typical structure of a vane-type system, composed of a series of independent blades hinged to the lateral metallic walls.

During the years several architectures and variants were introduced, making this type of subsystem both passively and actively controlled. Passive louvered surfaces base their functioning on small torsional springs connected to the hinges of the blades, placed in very good thermal connection with the radiator and reacting to temperature variations on the radiator itself. These springs work differently depending on the material they are made of: bimetallic springs are built combining together two metals with different thermal expansion coefficients, which undergo differential deformations modifying the shape of the spring and producing rotational motion; the same principle is exploited with SMA springs, taking advantage of the previously introduced (section 2) high sensitivity to temperature and of the large deformation of these alloys. Therefore, with such system the blades are opened or closed automatically to counteract the temperature variation, creating a passive feedback loop.

The downsizing of radiator-based thermal systems to the size of a typical CubeSat

Figure 4.2: The passive louver for CubeSats developed and patented by NASA. Digital image. NASA CubeSat Form Factor Thermal Control Louvers. NASA Technology Transfer Program.

panel has been attempted and achieved only in the last few years. An example of space-qualified and patented system developed by NASA [27] is presented in figure 4.2. This solution represents a perfect downsizing for a CubeSat of the classical system, being it composed of an external housing for the hinges of the small blades; the system is passive, as it relies on miniaturised bimetallic springs, and it is designed in order to be modular and adaptable to different configurations.

4.2 Definition of the requirements

As introduced in the previous section, the implementation of this type of subsystem in a size compatible for a picosatellite offers interesting challenges both from a design and a reliability point of view. The definition of the tasks of the subsystem and consequently of various steps in the design process comes from an analysis of the exclusive features it has to incorporate (in this case the IRESA is of primary importance in the design process) and the interest for possible future developments at the Chair of Astronautics, as this thesis project could constitute a basis for future improvements on the same subject.

Therefore, the definition of the requirements of the system is crucial in order to combine every aspect for a homogeneous outcome. A fundamental aspect regards the nature of the subsystem itself: despite being closely connected to a thermal control system, the manifacturing and testing of a real radiating surface is not presented on this work, and it is not included in the final design. A complete TCS should be tailored on the specific payload it has to serve, nonetheless it remains a fundamental ground element for the design process; preliminary calculations and simulations based on thermal equilibrium equations for a radiating surface in space, which are introduced in section 5, are fundamental to define how the system could operate in a future implementation.

With this choice the implementation of the specific elements belonging to the louver assembly gains generality, and becomes more based on mechanical aspects, dealing entirely with the challenges of using IRESA for this specific task. The following sections contain the functional, performance, constraints and verification requirements of the system, derived accordingly with the previous statements.

4.2.1 Functional requirements

Functional requirements define the specific tasks that the system needs to fulfill. The subsystem shall:

F1	Provide a mean to actively control the effective emissivity of a small radiator for CubeSats through a moving external louver system, in order to adapt the behaviour to the different needs of the payload and to the changing boundary conditions.
F2	Generate a continuous rotational motion for the blades of the louver, with the possibility to maintain each intermediate position depending on the needs of the TCS.
F3	Actively integrate the IRESA actuator as the only mean of motion, through a mechanical design tailored on the specific features of this new generation drive.

4.2.2 Performance requirements

Performance requirements express the performance ranges of the subsystem; in this case a simple performance is required from the system, which shall:

P1	Provide a 90 degrees range of motion for the external structures, replicating the working principle of the classical louver systems.

4.2.3 Constraint requirements

Constraint requirements usually include operational, environmental, safety or regulatory constraints. In this specific case, the subsystem is designed to comply with the most demanding standards in terms of size and functioning. Getting to the specific, the system shall:

C1	Comply with the CDS standard on maximum size protruding from the envelope surface of a CubeSat measured from the corner rails, which corresponds to 6.5 mm.
C2	Be contained in the surface of a 2U CubeSat side panel; part of the panel surface shall be dedicated to the housing of the IRESA board, while the remaining surface is entirely available for the radiator and louver assembly.
C3	Comply with the ECSS standard in terms of safety margins for spacecraft mechanisms.

4.2.4 Verification requirements

Verification requirements define under which environmental conditions the subsystem shall maintain its performances; in this specific case, the subsystem shall:

V1	Perform the basic operations of opening and closing in laboratory conditions, in order to assess the correct design, production and integration; special attention is given to the verification of the tolerances, due to the small size of the components
V2	Perform the same opening and closing procedures in vacuum conditions, recreating an operative environment more similar to the one encountered on a spacecraft in terms of SMA behaviour and tribological effects
V3	Maintain its structural integrity during the testing phase, conducted following the specifications of NASA GEVS-SE REV A and NASA-HDBK-7008, in order to qualify the subsystem

4.3 Preliminary design of the TCS

As mentioned in section 4.2, a preliminary thermal design of the system constitutes the basis from which the mechanical assembly design is derived. In general, the purpose of this type of system is to provide a dedicated thermal control unit linked to a sensitive payload, which must be maintained in a proper temperature range; the maximum or mimimum allowed temperatures shall never be reached or exceeded, both in normal operation and in the two nominal worst cases (worst hot case and worst cold case, respectively). The sizing of the system is subject, in this work of thesis, to limitations coming from the features of the hardware equipment already existing; in this case the most relevant design driver is the size and the hardware configuration of the current version of IRESA, as presented in the previous dedicated section. The geometry of the actuator is a fixed parameter and it is not alterable in any step of the design. Future adaptations or a combined design of the two subsystems could yield an improvement in this sense.
Therefore, the current size of the actuator contributes in defining the available portion of the lateral panel of a 2U CubeSat left for thermal control purposes. The following sections contain a brief introduction to the influence of view factors in radiative heat transfer, contextualising the adopted design strategy for the mechanics of the system.

4.3.1 Definition of view factor

View factors are important parameters in the analysis of radiative heat transfer, as they allow to determine the portion of thermal power mutually exchanged by generic surfaces placed in different configurations with respect to each other. Given the two generic infinitesimal surfaces dS_1 and dS_2 of figure 4.3, the view factor of surface dS_1 with respect to surface dS_2 is defined in equation 2:

$$F_{12} = \frac{1}{S_1} \iint_{S_1 S_2} \frac{\cos\alpha_1 \cos\alpha_2}{r_{12}^2} \mathrm{dS_1 dS_2} \tag{2}$$

A view factor value of zero indicates that none of the power emitted by dS_1 invests dS_2; on the contrary, a value of 1 means that all the power radiating from dS_1 hits the surface dS_2.
Analytical solutions to the integral in equation 2 are only found for simple configurations of the surfaces, for which explicit formulas exist and allow to calculate view factors; for these simple configurations, it is easy to analyse the dependence of the

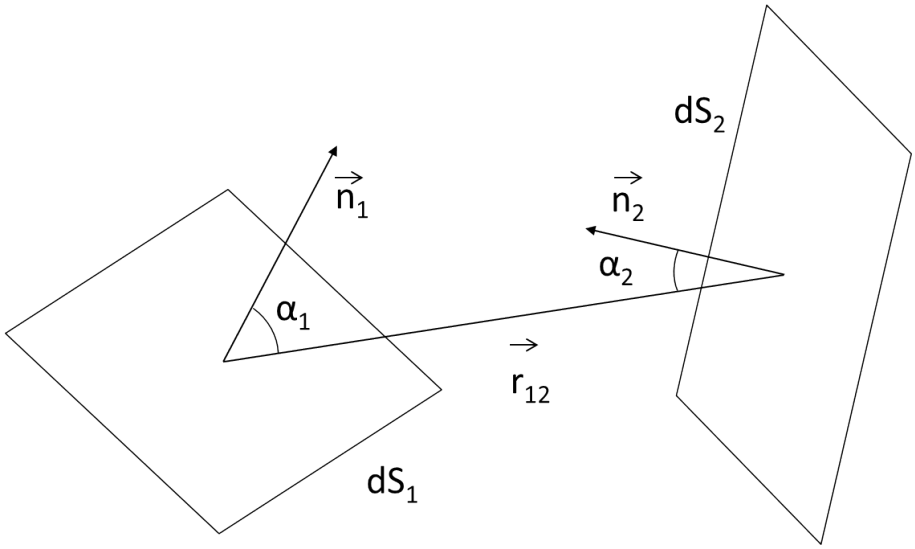

Figure 4.3: The relevant parameters used in equation 2.

view factor on the features of the surfaces, such as the dimensions, the aspect ratios, the mutual distance, the orientation, etc. More complex surfaces and geometries are usually discretised and reduced to basic planar surfaces, and the view factors between all the elementary surfaces are determined by specific softwares via numerical tools.

In the case of louvered surfaces the calculation of the view factor between the radiator and the blades is extremely important to correctly predict the functioning of the system. The radiator can be modeled as a plate emitting power only from one of its main faces, the internal one being coated and prevented from dissipating power inside the spacecraft; when the louvers are completely closed the view factor is easily found to be approximately unitary, with the whole radiating surface enclosed. When louvers are in the completely open configuration (i.e. they form an angle of 90 degrees with the surface) the view factor is at its minimum value, but the presence of the louver structure still interferes with the emitting capabilities of the radiator. This means that a certain amount of power is still retained even in maximum radiation configuration, leading to a necessary oversizing of the radiator in order to obtain the required emitting area or dissipate the generated power. This solution is easily achievable in normal satellites, considering the reduced size of typical radiators with respect to the whole spacecraft, but it is definitely not the best solution when size is a main concern, as happens in CubeSats. A different approach is followed in this case, aimed at reducing the complexity of the system and based on simple considerations on view factors between rectangular, planar surfaces, as reported in

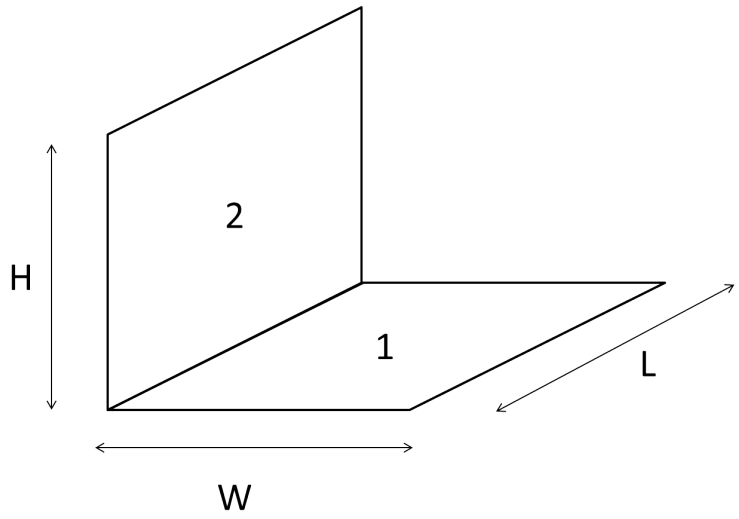

Figure 4.4: Geometric configuration of two perpendicular rectangular surfaces; in this case surface 1 is considered as the emitting surface and surface 2 is the absorbent surface. The two surface share the same depth L, but can have different H and W dimensions.

the following analysis.

Two important algebraic properties of view factors are reported, and later used in view factors calculations:

1. Reciprocity. For the two generic surfaces i and j it is easily found that:

$$S_i F_{ij} = S_j F_{ji} \tag{3}$$

2. Distribution. In the case of a source surface S_i with two different target surfaces S_j and S_k the total view factor is the sum of the two separate view factors:

$$F_{i,j+k} = F_{ij} + F_{ik} \tag{4}$$

The calculations for completely open louvers contained in this section refer to the configurations reported in figures 4.4 and 4.5, which approximate at different levels a real louvered surface. In this analysis, the complete surface surface of the radiator covered with louvers is split into several smaller surfaces separated by the open blades; with the hypothesis of equal temperature distribution on the radiator, these surfaces can be treated as independent on each other, as each one is enclosed by two blade surfaces and all of them are defined by the same view factors.

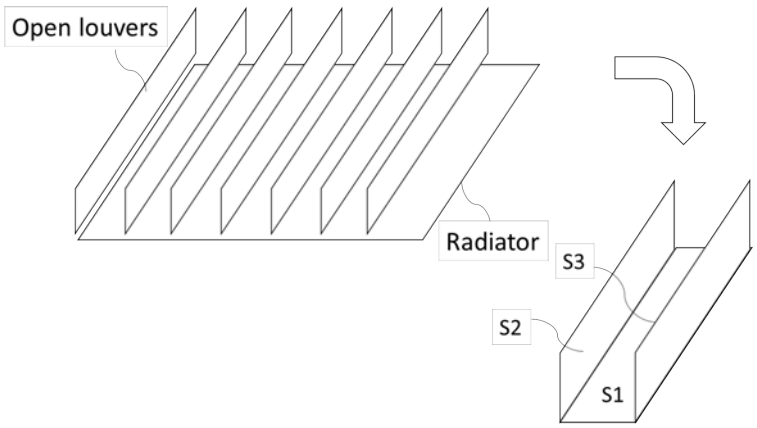

Figure 4.5: A simplified model of a louver (top left), composed of planar surfaces only, is even more simplified into an emitting surface S_1 and two absorbent surfaces S_2 and S_3 (bottom right) in order to easily calculate the total view factor.

With reference to figure 4.4, the following equation 5 (taken from the source [28]) allows to obtain the view factor F_{12}:

$$F_{12} = \frac{1}{\pi w}\left[h\ \tan^{-1}\left(\frac{1}{h}\right) + w\ \tan^{-1}\left(\frac{1}{w}\right) - \sqrt{h^2+w^2}\ \tan^{-1}\left(\frac{1}{\sqrt{h^2+w^2}}\right) + \frac{1}{4}\ln(ab^{w^2}c^{h^2})\right] \tag{5}$$

$$a = \frac{(1+h^2)(1+w^2)}{1+h^2+w^2}$$

$$b = \frac{w^2(1+h^2+w^2)}{(1+w^2)(h^2+w^2)}$$

$$c = \frac{h^2(1+h^2+w^2)}{(1+h^2)(h^2+w^2)}$$

where $h = H/L$ and $w = W/L$.
Referring to the surfaces of figure 4.5, the calculation of the view factor $F_{1,2+3}$ is possible by using equation 4 in combination with equation 5; for a generic louver, H and W share the same value, and L is at least one order of magnitude larger with respect to the other two dimensions. Calculations for $H = W = 1$ cm and $L = 8$ cm, dimensions compatible with the lateral panel of a CubeSat, yield a total view factor of:

$$F_{1,2+3} = 2F_{12} = 0.55$$

h	F_{12}
0.125	0.2792
1	0.2
1.5	0.1708
2	0.1493

Table 5: Values of the view factor for different aspect ratios between the two surfaces shown in figure 4.6.

This result shows that for a generic radiator, more than half of the surface emits power toward the louver; part of this power is reflected or absorbed by the blades (depending on their values of emissivity) and emitted again into open space or towards the radiating surface, thus reducing the heat rejection capabilities of the system.
A solution to the loss of performance may come from the removal of the support structure and the frame typical of classical louvered systems, and from a decrease in the number of blades, therefore modifying the aspect ratio between the radiator and the louver: this procedure is adopted in the present work, as it proves helpful also in reducing the mechanical complexity of the system. Taking the simplification to the extreme, a single panel for which $H = L > W$ is proven to be the best solution in terms of minimization of the view factor in the completely open position. The curve of figure 4.6 shows the dependence of the view factors on the aspect ratio h (as previously mentioned, in this case $h = w$); the value of the view factor F_{12} decreases as h increases. A set of results for a few combinations of values of h, highlighted on the curve with blue circles, is presented in table 5.
Figure 4.7 presents a schematic of the preliminary geometry of the system, based on the assumptions and calculations made in the present section. The dimensions of the system are derived from the maximum surface available for a 2U CubeSat and they are reported in the scheme of the satellite, together with a simplified louver.
The view factor between the two finite rectangular surfaces is also easily calculated when they are not perpendicular to each other; no analytical solution exists in this case, and the view factor must be found via a numerical procedure. The exact formula, as found in [29], is included in the appendix B of this document. Figure 4.8 shows the value of the view factor F_{12} versus the angle ϕ between the radiator and the blade and for the aspect ratio deriving from the now fixed dimensions of the system, and corresponding to $h = 1.2683$; regarding the tilt angle between the two surfaces, ϕ equals 0 degrees when the louver is closed and 90 degrees when the

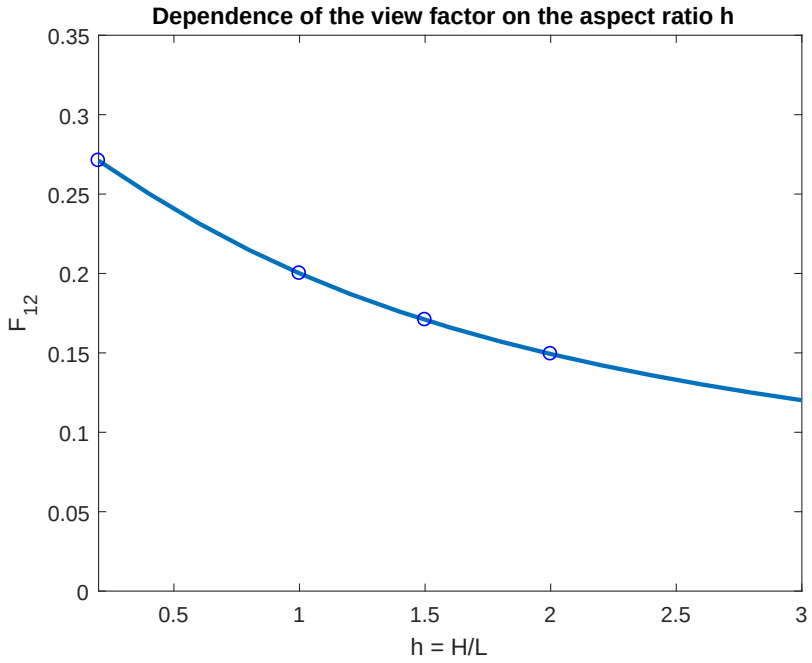

Figure 4.6: The view factor decreases as h increases, thus a smaller portion of emitted power impinges the open louver surface; the blue circles correspond to the values of h reported in table 5.

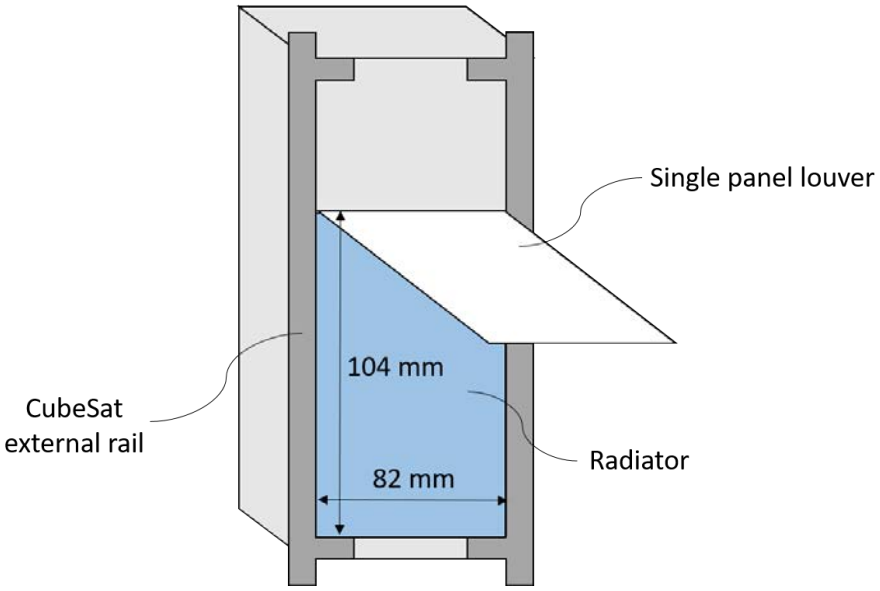

Figure 4.7: A simplified scheme of a 2U CubeSat, showing the proportions of the system compared to the size of the satellite.

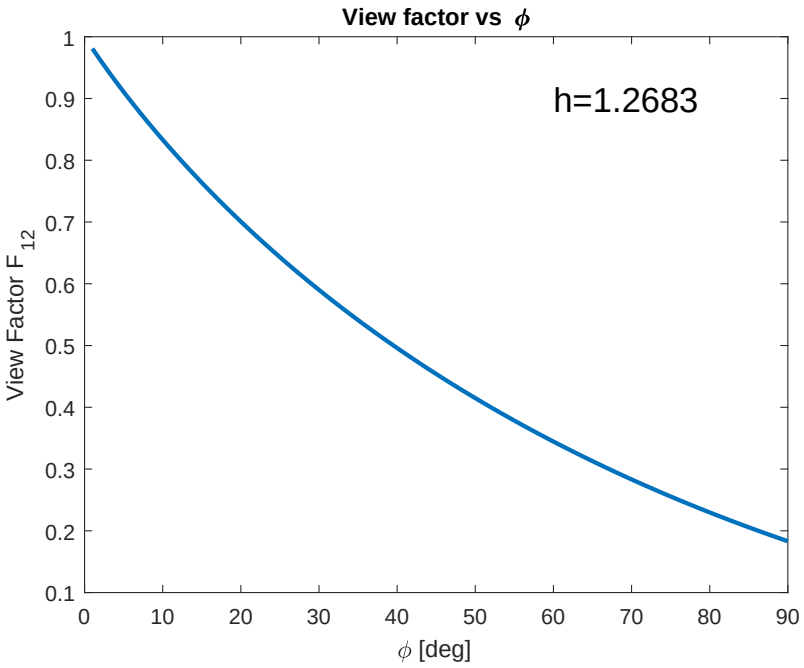

Figure 4.8: Value of view factor F_{12} for the operative angular range of motion of the louver, and for the effective aspect ration available for the system.

panel is completely open). In addition to the previous geometrical considerations, the chosen design represents a net simplification in terms of complexity. Implementing a series of interconnected blades actuated together by IRESA would be a notable complication in terms of design, manufacturing and assembling, without showing remarkable advantages in terms of prototyping and testing if compared to the proposed solution. Moreover, a larger number of hinges would require a larger number of properly designed extremely small components, and an increase in the total friction for the whole system. However, such a design is still possible with the given hardware, and a concept deriving from the design process carried out in this thesis is presented in the final part of this document, in the section 8.2 dedicated to possible future developments.

5 Thermal analysis

This section provides a general overview on the thermal performance of the louver analysing the effect of different thermo-optical parameters on the behaviour of the system. In particular, the analysis focuses on the amount of power q_{pl} which can be effectively dissipated by the system for different values of the emissivity and the absorption coefficient, and for different angular configurations and boundary conditions: in this case of preliminary calculations the effect of the solar radiation is the sole boundary condition considered, due to its generality and simplicity in terms of mathematical implementation in the model. Further investigations could be carried out in future analyses in order to include the effect of the planetary IR emission and the effect of the albedo. These sources of thermal exchange require the knowledge of the orbital parameters and the nominal attitude of the satellite in order to be properly predicted and calculated, mostly due to the view factors between the planet and the radiating surfaces.
On the other hand, the effect of solar impingement provides useful information on the behaviour of the system, and it allows to understand the situations in which the use of the proposed thermal control unit could be beneficial for a payload or for the thermal stability of the satellite.
In specific, the following parameters are taken into consideration during the calculations:

- the emissivity of the radiator in the infrared spectrum ϵ_r;
- the coefficient of absorption of the radiator in the visible spectrum α_r;
- the emissivity of the louver in the infrared spectrum ϵ_l;
- the coefficient of absorption of the louver in the visible spectrum α_l;

For the sake of simplicity and in order to reduce the number of parameters the louver is considered to have the same coefficients both for the internal and the external surfaces, while a more accurate analysis could be made if different optical properties are imposed on the two sides, for example if different surface finishes or thin layers of other materials are applied on one or the other surface.
The effects of different values of each parameter are evaluated for every angular position of the louver (determined by the value of ϕ) and also for different angles of incidence θ of the solar radiation. Figure 5.1 presents the main parameters under

analysis as well as a simplified geometry of the system, which is composed of a radiator of surface A_r and the louver, with a surface equal to the radiator on each side. The purpose of the system is to provide a dedicated thermal control to a specific payload, which can only operate within a precise temperature range. The radiator is thermally insulated on its internal face, in order to decouple the internal environment from the external emitting surface; this design solution allows to neglect the power emitted from the internal surface.
The temperature range of the specific piece of equipment shall not be exceeded in every possible operating condition, and for this reason a system based on an active control of the emitted power could prove to be beneficial for the thermal stability of the inner region of the satellite. In particular, this section addresses two possible advantages of placing an active louver with the previously shown geometry in front of a radiating surface, which are:

- the possibility to control the temperature T_r and/or the amount of emitted power q_{pl} by regulating the angle ϕ of the louver, in case of absence of external thermal sources (such as plaetary emissions and solar radiation);
- the ability to counteract and reject a large part of the solar power illuminating radiator, in case this event occurs due to a specific manoeuvre or to an unexpected change in the nominal attitude of the satellite.

In all the following cases the simple assumption of isothermy between the radiator and the payload is made, neglecting the small difference in temperature and therefore considering a perfect thermal connection between the two elements; this assumption means that a change in the temperature of the radiator due different boundary or operative conditions is linked to an equivalent change in the temperature of the payload, and therefore the knowledge of the temperature of the radiator completely defines the system. All the following results are obtained imposing a value of 15°C to the temperature of the radiator (suitable for most of the payloads) and calculating the associated q_{pl} which can be dissipated.

5.1 Thermal model

The simplified thermal model adopted for this analysis is implemented in MATLAB and it is based on two thermal nodes: the radiator and the blade of the louver (marked respectively with the numbers 1 and 2 in figure 5.1). The two elements are physically decoupled and cannot exchange heat via conduction, but only via

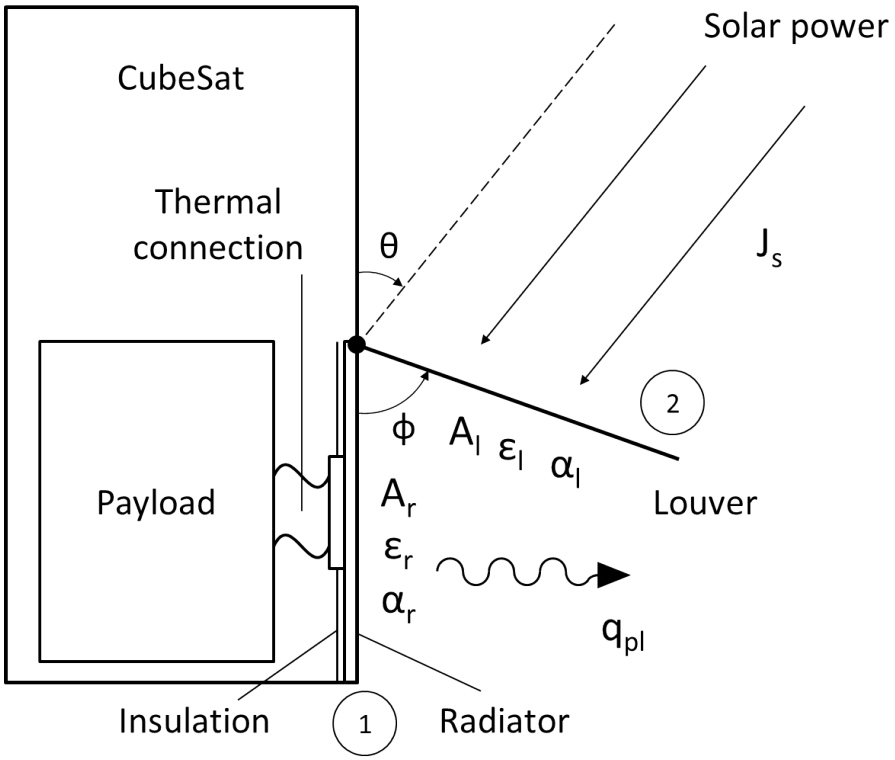

Figure 5.1: A schematic model of the use of the TCS: the radiator (first thermal node) is thermally connected to the payload but insulated from the rest of the satellite, therefore operating at its own temperature; the louver (second thermal node) interacts with the radiator via radiative heat transfer only; the incidence angle θ drives the effect of solar radiation, while ϕ determines the behaviour of the louver; q_{pl} is the parameter to be determined in every simulation and the goal of the thermal control system.

radiation. Ideally, the louver and the radiator are also perfectly insulated from the surrounding structure of the spacecraft, even if in a realistic environment a small amount of power is transferred through the supports and the hinges: this effect could be modeled as a net heat flow or a conductive heat flow when thermal tests are made on the subsystem and experimental data is used to enhance the model, but it is neglected in these prelinary calculations. As a preliminary assessment, this analysis can be used to determine what critical conditions are found during operation, and for which combination of parameters the system performs better in terms of heat dissipation capability, rather than providing precise information on the exact amount of power q_{pl} or on the temperatures of the nodes.

The radiator and the louver exchange heat as ideal, lambertian surfaces, therefore the view factors between the surfaces are used to determine the equilibrium tem-

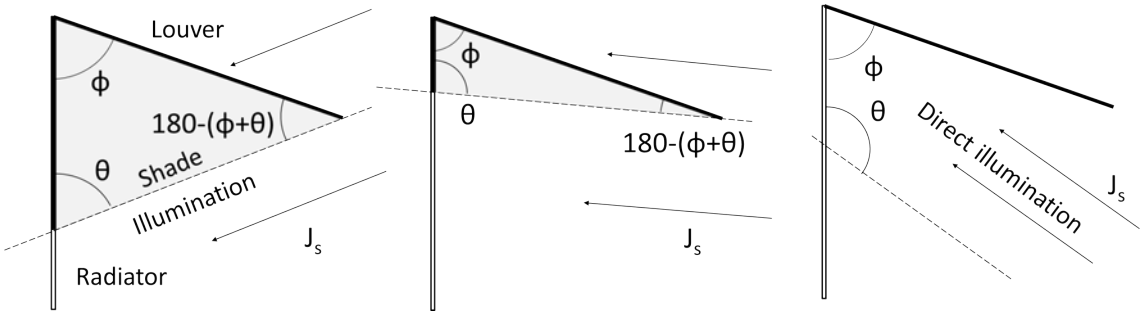

Figure 5.2: Different illumination conditions are generated depending on the angle of incidence of the solar radiation θ.

peratures and the reciprocal influence of the two bodies.

Moreover, a dedicated function is responsible for the calculation of the different illumination produced by the sun rays on the louver and the radiator for different opening angles and angles of incidence (an example of which is reported in figure 5.2), calculating the effect of direct impingement and also of mutual reflections. The louver is expected to shield the system from external solar power, and therefore to reflect into space a large portion of the incoming rays: the reflection of the louver is modeled as diffused, neglecting the effect of specular reflection. In order to adopt this simplification, a previous analysis on the impact of specular reflection was carried out, verifying that this choice is in favor of safety and that the amount of disposable power is slightly higher if a partial specularity of the surface is accounted for.

The first simulations, presented in section 5.2.1, are addressed to defining the amount of power dissipated for each angular position of the louver, while the following section 5.2.2 extends the analysis including the effect of solar radiation and provides information on the behaviour of the system as a protector from unfavourable external conditions.

5.2 Simulations and results

The simulations presented in this section are performed using the set of parameters of table 6, equal for all the different cases unless specified in a different way: each plot in the following sections is obtained imposing a range of values to the parameter under analysis, but the other constant parameters always maintain the value reported in the table. The details of the thermal model and its fundamental equations are reported in appendix C.

Parameter	Value	Unit
T_r	15	°C
A_r	0.0085	m^2
ϵ_r	0.8	-
α_r	0.2	-
ϵ_l	0.15	-
α_l	0.1	-
ϕ	0-90	deg
θ	0-180	deg
J_s	1366	[W/m^2]

Table 6: The parameters used for the simulations.

5.2.1 Thermal characterisation with no external conditions

The first, simpler simulations performed with the model have the task to define the characteristic behaviour of the system considered as isolated from external thermal conditions. The amount of disposable power q_{pl} in this case is only dependent on the opening angle ϕ, due to the influence of the view factors on the emission capability of the system. The solar constant is set to zero, so no effects of illumination are taken into account, and the parameters α_r and α_l do not play any role in this analysis.
The important parameters to be studied are therefore ϵ_r and ϵ_l, as they strongly modify the behaviour of the system in the infrared spectrum.
Figures 5.3 and 5.4 present the characteristic curves of the system obtained varying the two aforementioned parameters. The plots show the influence of different values of the two emissivities on the power q_{pl} over the whole range of motion of the louver. The curves corresponding to different values of emissivity are traced with a different tone of grey and thickness, and the values of the analysed parameter are impressed on the plot in order to simplify the visualisation. The values of ϵ_r cover a broader range, since different design strategies and coatings can be chosen for the radiating surface and a wider variety of solutions can be adopted. The values of ϵ_l are lower and taken from a more narrow interval, so that the louver interferes less with the radiator and it absorbs a lower portion of the emitted power, settling to lower operative temperatures; this effect is positive for every angular configuration, since it allows for a lower influence of the louver on the emission when the system operates at maximum dissipation (which means that the louver is fully open), and it allows for a better decoupling of the interior and the exterior of the satellite when it is fully closed, therefore insulating the payload and the radiator from space and maintaining a more stable environment.

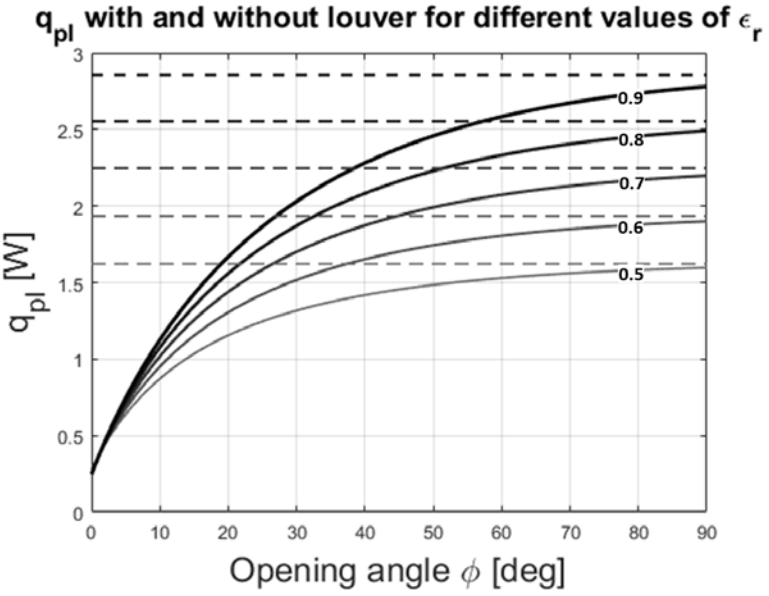

Figure 5.3: Dissipated power q_{pl} over the whole opening angle range and for different values of ϵ_r: higher values of emissivity are preferable in order to dissipate a larger power at full regime ($\phi = 90$ deg) and to operate with lower power emission when the louver is closed.

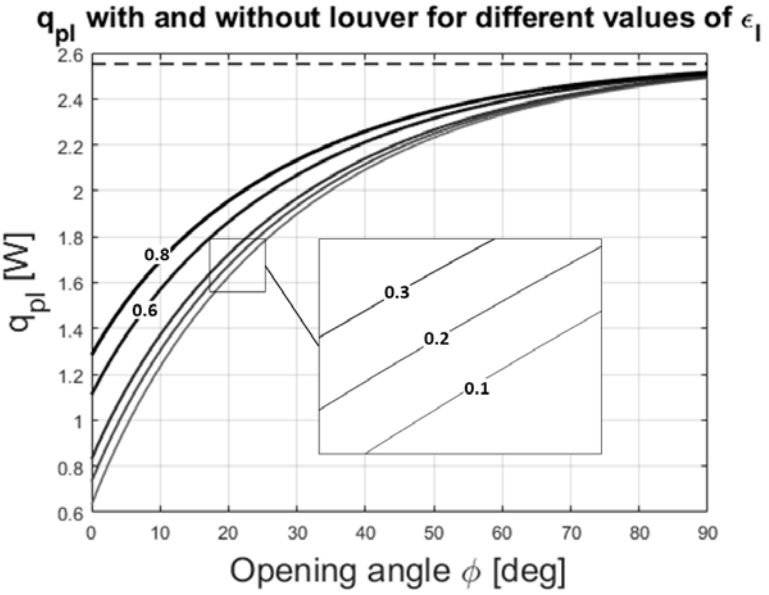

Figure 5.4: Dissipated power q_{pl} over the whole opening angle range and for different values of ϵ_l: lower values of emissivity allow for a better thermal insulation when the system is closed while causing no effect on the dissipation at full regime ($\phi = 90$ deg).

Figure 5.3 confirms a large impact of ϵ_r on the performance of the system, as evidenced by the wide shift present between the curves of the louvered radiator (continuous lines) and the constant curves of an ideal, equivalent unlouvered radiating surface (dashed lines). A higher value of emissivity allows to dissipate more power when ϕ is close to 90 degrees, while at the same time it provides a better insulation for ϕ close to 0 degrees, thus proving that a lower amount of power is lost when the louver is closed and a better insulation is reached.

Figure 5.4 confirms the hypothesis of a better performance of the system for low values of the emissivity of the louver: when ϵ_l is low (0.1 - 0.3) a better insulation is attained at nearly no expense in terms of maximum disposable power in the fully open condition.

5.2.2 Thermal characterisation with the effect of solar radiation

The previous analysis carried out in absence of external thermal inputs is now enhanced and extended in order to include the solar radiation into the operation of the system. As shown in the introduction of this section, the angle of incidence of the sun covers a full 180 degrees range, and the incoming power interacts differently with the system depending on direct illumination and reflections.

As a first assessment, the disposable power q_{pl} for various angular configurations and over the whole incidence range is calculated, in order to verify the correct functioning of the model. These first results are shown in figure 5.5. The different curves in greyscale colour shown in the plot correspond to different opening angles ϕ and they cover a range of different responses of the system. For larger opening angles a strong change in the slope of the curve occurs when the sun starts to illuminate the radiator: a dramatic decrease in the emission capability is found and it proceeds with an approximately constant slope until a minimum is reached, after which the lower inclination of the sun rays allows to progressively improve the performance and dissipate an increasing amount of power.

Passing to lower values of ϕ the breaking point in the curves is correctly found at higher values of θ, and the decrease in the value of q_{pl} after the change in the slope is less pronounced proceeding towards smaller angles. The curves relative to different opening angles overlap in this region when ϕ exceeds 30 degrees, showing that the maximum power level is found at lower opening angles as the incidence increases, and proving the beneficial shielding effect of the blade in front of the radiator; as mentioned, this trend is only found until an optimal condition occurs between the

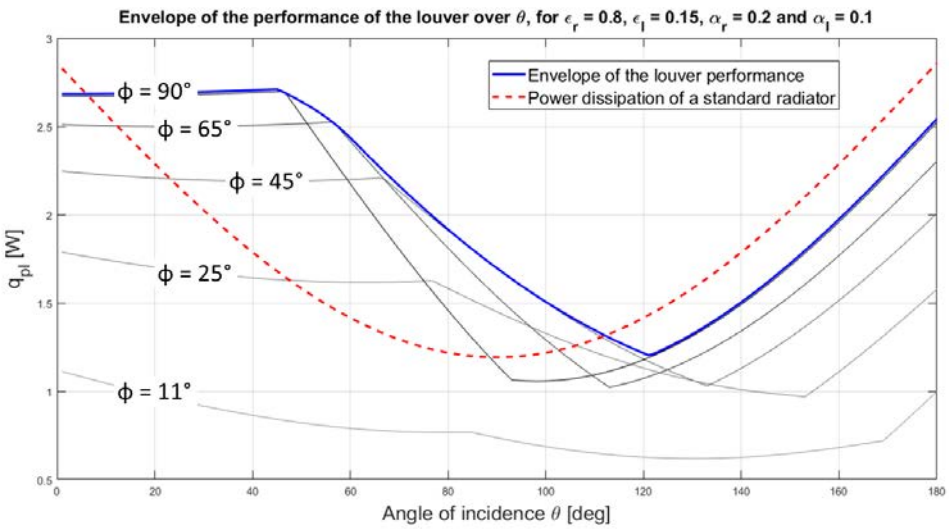

Figure 5.5: The characteristic curves of the system for various values of ϕ (greyscale) show the different response over the incidence range; an envelope (blue curve) marks the best condition of the system in terms of power dissipation, defining the maximum value of q_{pl} for each value of θ and spanning over different opening angles; the performance of an equivalent unlouvered radiator is also reported as a term of comparison (red dashed curve).

value of θ and ϕ, after which a decrease in the opening angle (below 30 degrees) only causes a worsening of the performance: this means that it is more convenient to keep the louver open if the goal is to dissipate as much power as possible, due to the low value of the angle of incidence and the smaller impact of the impinging radiation.

In order to compare the performance of the louvered radiator with the behaviour of a simple, equivalent radiator with no shielding, a proper envelope of the previously introduced curves shall be taken. Figure 5.5 also reports the envelope (blue colour) of the family of curves described up to this point: the envelope shows the maximum amount of disposable power at each value of θ, incorporating the information of the angle ϕ necessary to obtain the specific performance. The envelope can be compared with the curve of a standard radiator (red colour and dashed line in the plot), the functioning of which is strongly affected by the incoming solar radiation. As visible in the plot, the power curve of a simple radiator follows a parabolic trend, and the maximum dissipation is only possible when the angle of incidence approaches 0 or 180 degrees. The envelope of an equivalent louvered radiator lies above the parabolic curve for a large portion of the considered angular range, meaning that for each angle the disposable power attainable by this system is higher. In the

regions where the parabolic curve stands above the envelope, the difference between the two curves is small, meaning that the louver only lowers the performance of the radiator in specific regions and by a small amount.
The plots of figure 5.6 present the effects of the different optical parameters on these curves, showing for which combination of values the two performances differ the most, and in which cases the use of a louver of this type improves the overall performance of the thermal control system.

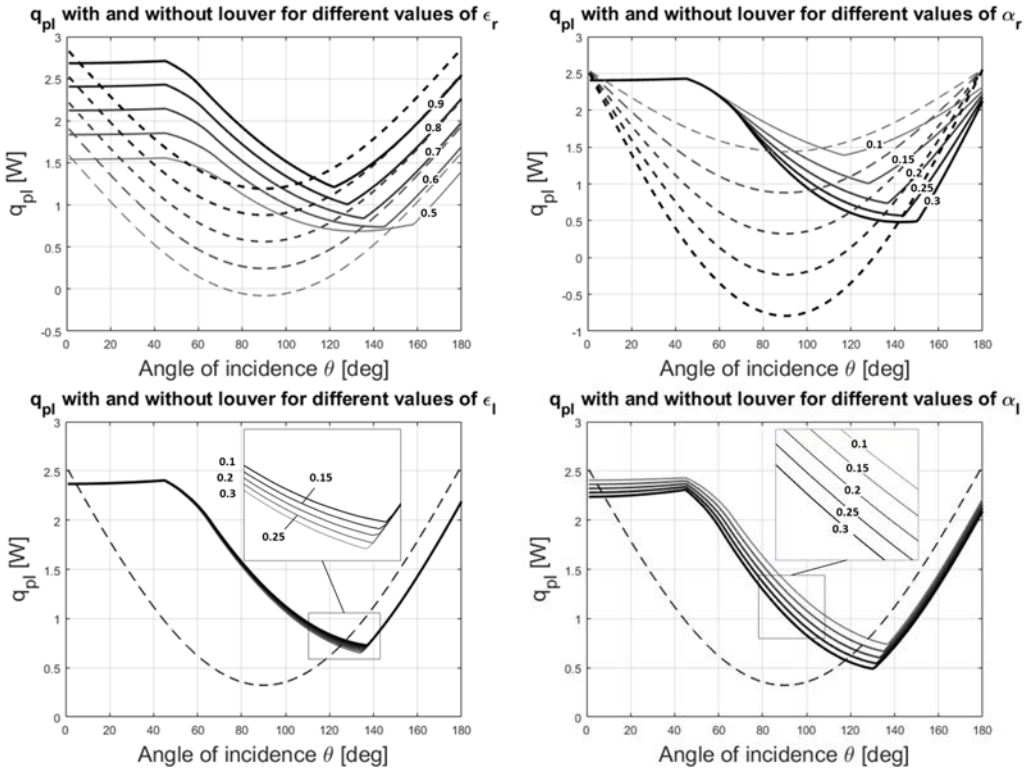

Figure 5.6: Plots obtained for different values of ϵ_r, α_r, ϵ_l and α_l, and showing the improvement in the performance of the system when the louver acts as a shield for the incoming solar radiation.

The plots show the envelope curve associated with every set of optical properties and the respective parabolic curve of the equivalent unlouvered radiator. Each envelope is marked with a continuous line and is associated to a specific tone of grey, which is also used on the corresponding dashed line of the simple radiator. The first two plots are obtained by assigning different values to ϵ_r and α_r, and both the families of curves are largely affected by the change in these parameters. The last two plots are obtained for different values of ϵ_l and α_l, so only a single curve for the unlouvered surface exists and is compared to the envelopes.
Observing the plots more in detail and starting from the one relative to different

values of ϵ_r, it is possible to see that this parameter has a large impact on the power dissipation capabilities of the system, as happened also in the previous simulation not accounting for the solar radiation. The parabolic curves are shifted vertically by a considerable amount as the emissivity changes, and for the lowest values of ϵ_r the vertex of the curves approaches and crosses the zero line: this means that a simple radiator cannot counteract the effect of solar radiation if its emissivity stands below 0.5, and the value of q_{pl} decreases until it becomes negative, meaning that the system starts transferring heat towards the payload instead of removing it, and that it would require an active cooling system in order to compensate for this phase. The envelopes of the louvered surface show instead that an always positive value of q_{pl} is attainable over the whole range of incidence of the solar radiation, and that the system becomes more stable in terms of emission and less dependent on the value of emissivity: this result means that for every value of θ it is possible to extract a certain amount of power from the payload, without recurring to other means of thermal control; as expected, a stronger dependence is still maintained in the first part of the plot, for lower values of θ.

The second plot presents the dependence of the curves on α_r, showing the strong influence of this parameter on an unlouvered radiator, for which the inability to dissipate heat becomes more evident even for low values of α_r, close to 0.25 or 0.3; the behaviour of the louvered radiator differs the most for these values of the parameters, as the envelopes are more separated from the corresponding parabolic curves and settle to considerably higher values, confirming that the louver acts efficiently as a shield, improving the performance of the radiator. In the first part of the range the envelopes are approximately coincident, as the value of the parameter under analysis only starts to have any effect when the direct illumination of the solar power on the radiator occurs. The beneficial effect of the louver on the system is of course less pronounced for lower values of α_r, as the radiator is able to effciently reject the incoming radiation by itself: however, even in this condition an improvement of the performance is found for angles of incidence in the range between 0 and approximately 110 degrees, at the expense of a small reduction in the performance in the remaining part of the range.

The last two plots refer to the effect of ϵ_l and α_l on the performance of the system. What is evident from the curves is that the impact of these parameters is less pronounced with respect to the parameters of the radiator, thus allowing for a larger flexibility in the design of the surfaces of the louver. In particular, the envelopes obtained changing ϵ_l are almost coincident, with only a minimum difference in the

disposable power: however, the difference in the value of emissivity determines a different equilibrium temperature for the louver, which may be an important design parameter due to the thermal response of the adopted materials.
In the last plot, a difference in the value of α_l produces instead a larger effect on the value of q_{pl}, especially in the range of $1theta$ between 45 and 120 degrees, thus showing that a reduction in the coefficient of absorption of the louver is largely beneficial for the performance of the thermal control system.
As a conclusion of this preliminary analysis of the system, it is proved that the presence of the louver does improve the flexibility of the thermal control system, allowing for a wider range of operative conditions and different power dissipation levels, which can be adapted to the needs of a specific payload or can deal with a discontinuous operation of the on-board equipment and counteract any potential overheating; the analysis also proved the positive effect of the louver on the system when external conditions interfere with the nominal heat transfer procedures, showing that a functioning close to a certain degree to the nominal operation is possible over a large portion of the range of the external input, and simply by keeping the louver open at the correct angle through an active control system.

6 Mechanism design

This section contains the main mechanical aspects of the subsystem, and it presents the working principle of the system, the subsequent detail design of the various components and the simulations performed in order to assess the functioning of the mechanism. This section is closely connected to the following section 7, in which a more practical description of the prototype is provided.

6.1 Preliminary design and working principle

As presented in previous section 4.3.1, in which a synthesis of the system was obtained from geometrical and thermal points of view, the thermal louver presented in this work is simplified into a single panel hinged directly to the external rails of the CubeSat and not connected to the underneath radiator, in order to decouple the two elements during the nominal functioning; IRESA has therefore the task to control the angular position of the panel depending on the requirements set by the TCS. Unfortunately, the output rotation generated by the disk mounted on the back of the board is not suitable to produce the required rotation around an axis parallel to the board itself, as the axis of rotation of the disk is perpendicular to it. Therefore, a different approach is adopted to cope with the requirements of this specific application and to produce the necessary motion.
As explained in section 3, the actuator produces a linear displacement for a total stroke up to 3.5 mm; considering a proper safety margin, the mechanism is designed to operate with a maximum displacement of 3 mm, in order to account for small misalignments arising from the manufacturing process and non-perfect tolerances between the moving parts. The status of prototype of the system justifies this choice to operate in favor of safety, since the production of components with extremely strict tolerances would represent an increase in manifacturing time and costs. Further improvements could be carried out in the future in order to exploit the maximum possibilities of the actuator.
In this case a maximum rotation of 90 degrees is to be reached, and as a design choice a normally-open configuration is to be preferred for the system. Therefore the actuator needs to be in the extended position when the panel is open, and in the maximum contracted configuration when the panel is closed; the solution chosen to achieve this effect is a simple lever configuration, due to the high force output available from IRESA and the small mass and moment of inertia of the protruding panel.

A schematic of the functioning principle of the lever is presented in picture 6.1, showing the two extreme configurations of the panel and an intermediate configuration, corresponding to an angle ϕ equal to 45 degrees. The position of the two rotation axes of the system was chosen in order to maintain for the most angular configurations between the extremes 1 and 2 a nearly zero horizontal displacement of the moving hinge. With such a simple assumption the maximum displacement occurs when the louver blade is half open. Deriving the dimensions of the lever from this design choice, L corresponds to the value of 1.5 mm, while it is also immediate to determine the value of D and the value of l, maximum displacement along the x-axis, from basic trigonometry:

$$D = \sqrt{2L^2} = 2.121 \text{ mm}$$

$$l = D - L = 0.621 \text{ mm}$$

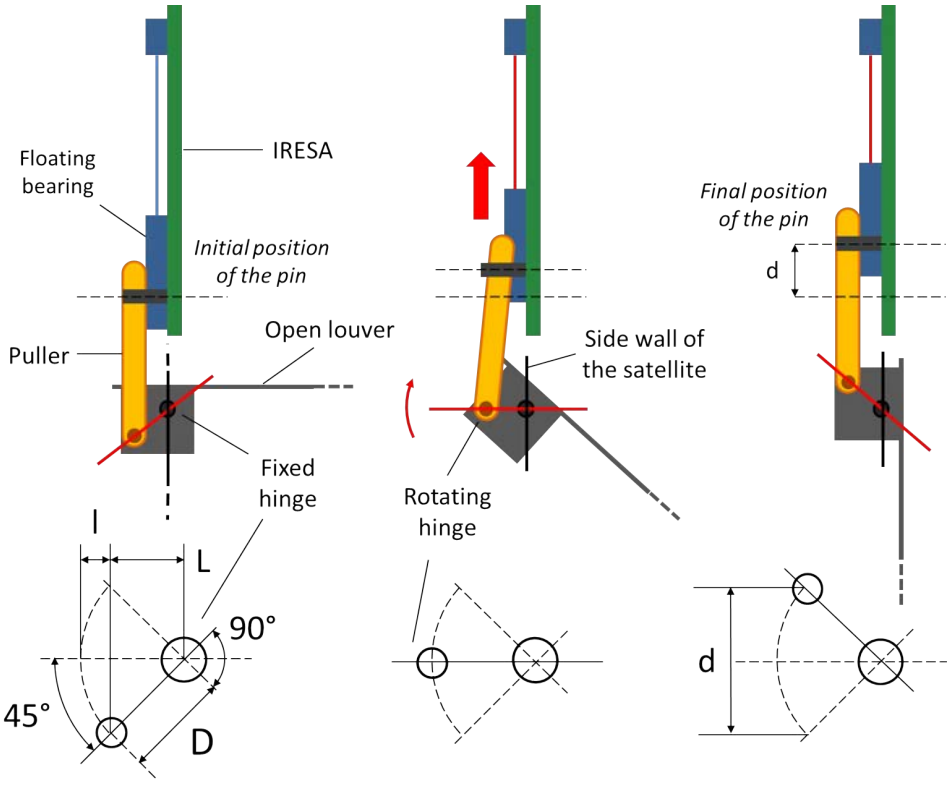

Figure 6.1: A schematic representation of the lever implemented to move the blade of the louver (top) and an enlargement of the hinges (bottom) show the characteristic dimensions of the lever, including lengths and angles.

6.2 Prototype mechanical design

This section contains the final design used to manifacture the prototype, showing the evolution from the initial concept to a coherent assembly that is a) resistant to possible mechanical loads b) kinematically coherent with the lever principle introduced in the previous section and c) a good trade-off between similarity to a hypothetical version flying in space and a low cost and easily manufacturable mechanical system. The basic concept behind the design is to exploit the existing hardware in its current version and to minimize the number of components in order to reduce the complexity of the assembly. A complete description of the system is contained in tables 7 and 8, in which all the relevant components are listed and briefly described; the same elements are also reported in figures 6.2 and 6.3, to provide a complete overview on the mechanics of the system.
The components marked with an S in addition to a number belong to the support structure, which is similar to the one of a real CubeSat but is not designed to be effectively mounted on a satellite, while the elements marked with H consist in existing hardware. The structural elements were designed using some of the MOVE-II satellite components as a base and reference.

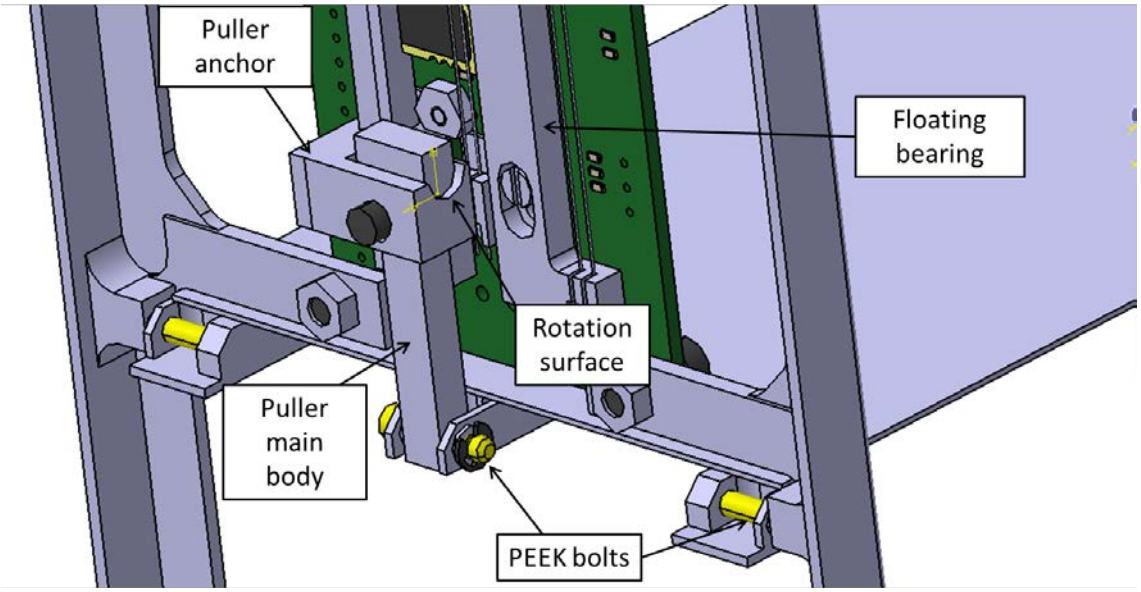

Figure 6.2: A detail of the most important elements in the design: the hinges with non-coinciding axes and the pulling element which connects the actuator to the louver.

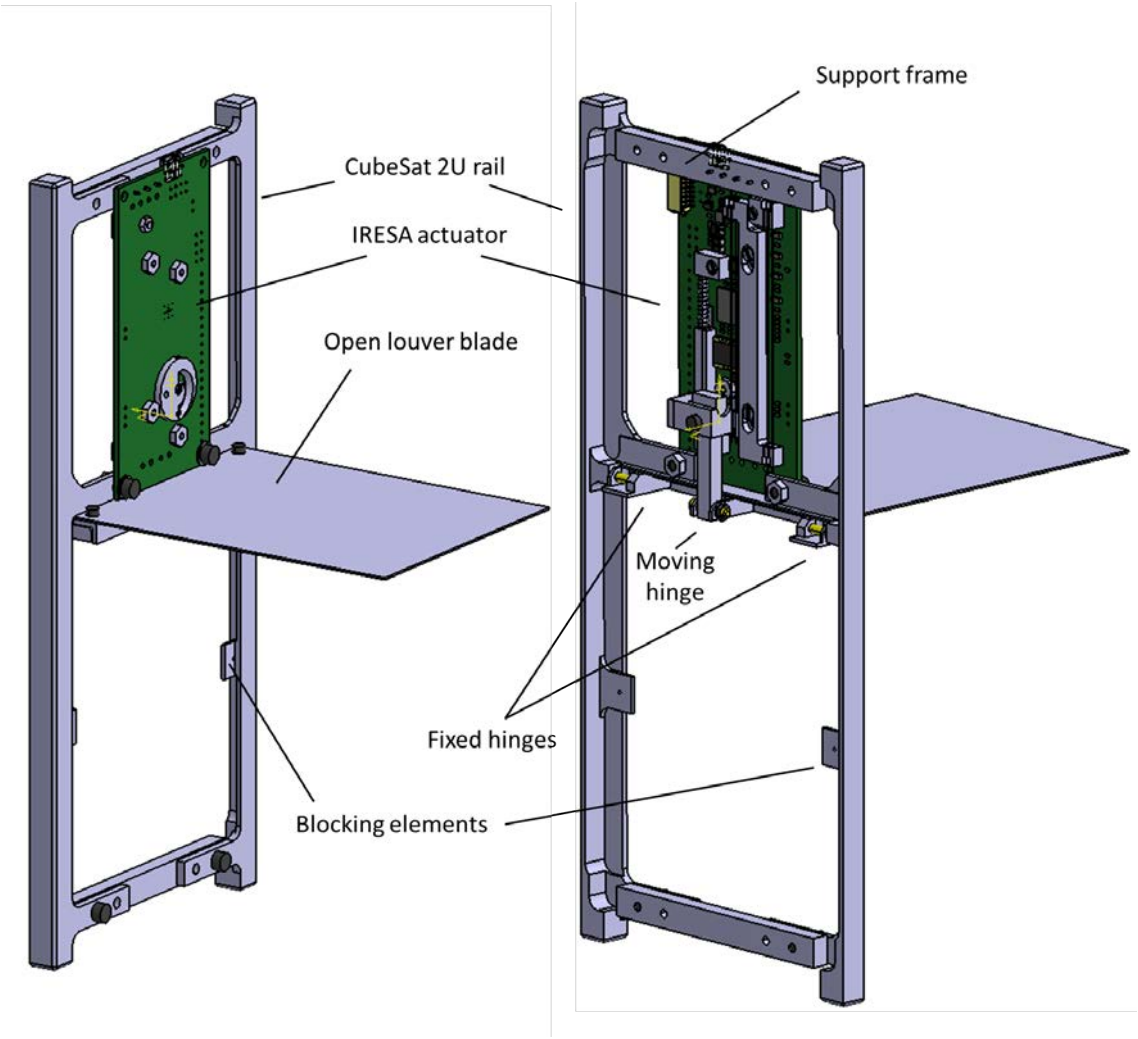

Figure 6.3: The complete prototype of the subsystem in the open configuration, with the panel at 90 degrees perpendicular to the lateral face of the satellite; the external side of the experiment is visible on the left, while the internal side is shown on the right.

Table 7: A list of the elements which compose the subsystem, and which are the object of the design and later verification.

Number	Name	Material	Description
1.1, 1.2	Hinges	Aluminum 6061-T6	These two elements connect the louver assembly directly to the rails; they are equal but mirrored; the holes which house the bolts have a diameter of 2.5 mm.

2	Lever	Aluminum 6061-T6	This element connects the louver assembly to the puller, which is in turn connected to the sliding structure of the actuator; the lever houses a hole placed in the correct position in order to satisfy the dimensions reported in section 6.1.
3	Louver stiffner	Aluminum 6061-T6	This L-shaped element is necessary to ensure that the relative position between the hinges and the lever is not changed during operation due to the potential deformation of the thin louver panel.
4	Louver blade	Aluminum 6061-T6	The blade of the louver, which is connected through screws to the stiffner; this solution allows an easier mounting and replacement of this element, allowing also to create a modular system, in which blades of different thickness and size can be tested or mounted.
5	Puller anchor	Aluminum 6061-T6	This element provides a hard mounting with the sliding element of IRESA through a screw which creates preload; this element moves rigidly with the actuator, and it is separated from it just for prototyping purposes, since a future iteration of the design could easily incorporate the two bodies in one single element.

6	Puller main body	Polyether ether ketone (PEEK)	This component is connected to the lever through a bolt which has rotational freedom with respect to the puller, creating a revolute joint; this element is also free to rotate with respect to the anchor, by means of two matching, curved surfaces: this solution is necessary in order to overcome the slight displacement encountered during the closing process, because of which a rigid element would generate unnecessary stress on the louver assembly.
7.1, 7.2	Bolts	Polyether ether ketone (PEEK)	The three bolts have the same diameter, corresponding to 2.5 mm; they are designed to form a clearance fit with the matching holes, creating three revolute joints.
H1	IRESA board	PCB, SMA	The actuator in the current version.

Table 8: A list of the elements of support, which are designed to be realistic and comparable to real hardware.

Number	Name	Material	Description
S1, S2	CubeSat rails	Aluminum 6061-T6	The two structural elements are similar to real CubeSat components, only differing in the level of tolerance and surface finish, reduced to obtain an easier manufacturing.
S3	Support frame	Aluminum 6061-T6	Simple structural elements which hold the two external rail in the correct position.

As visible from the figures, the adopted solution is only effective in pulling (hence the name puller for the connection element) the louver from an open configuration

to a closed one, forcing the blade to rotate and to follow the contraction of the wires: as the wires are progressively elongated and the actuator is reset, a torsional spring mounted on one of the hinges provides the torque necessary to open the louver following the given elongation profile and creating preload between the head of the puller and the puller anchor, in the rotation surface highlighted in figure 6.2. Figure 6.4 shows the spring in its position, with one end acting on the CubeSat structure and the other on the hinge of the louver. The spring is relaxed when the panel is completely open, and it is compressed to the maximum level when the louver is closed. A precise value for the rate of the spring is not set and could be adapted after the first functional tests. A plausible value is given in section 6.3, dealing with mechanical simulations.

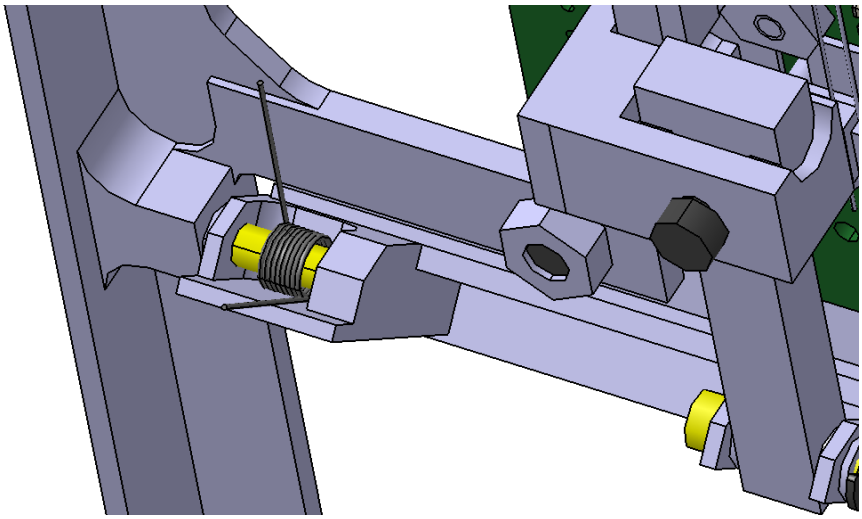

Figure 6.4: The torsional spring which provides the preload necessary to guarantee a correct opening phase for the louver, in order to keep the head of the puller connected to the anchor.

6.3 Kinematic and dynamic simulations

A kinematic and dynamic simulation is performed on the assembly, in order to assess a series of features of the system, and in particular:

1. the correct design of every component and of the assembled structure, by importing the most relevant 3D parts from the CAD software;
2. the kinematics of the mechanism, and the correct functioning of the lever system and every component involved in the motion;
3. a dynamic assessment of the reaction forces and friction forces that arise during normal operation.

In the first step of the analysis a simplified model of the louver mechanism is imported into the Adams workspace, as shown in figure 6.5; the only components included in the model are the blade and the support structure, which includes the hinges and the lever, and the pulling structure, which includes the puller main body and the anchor.

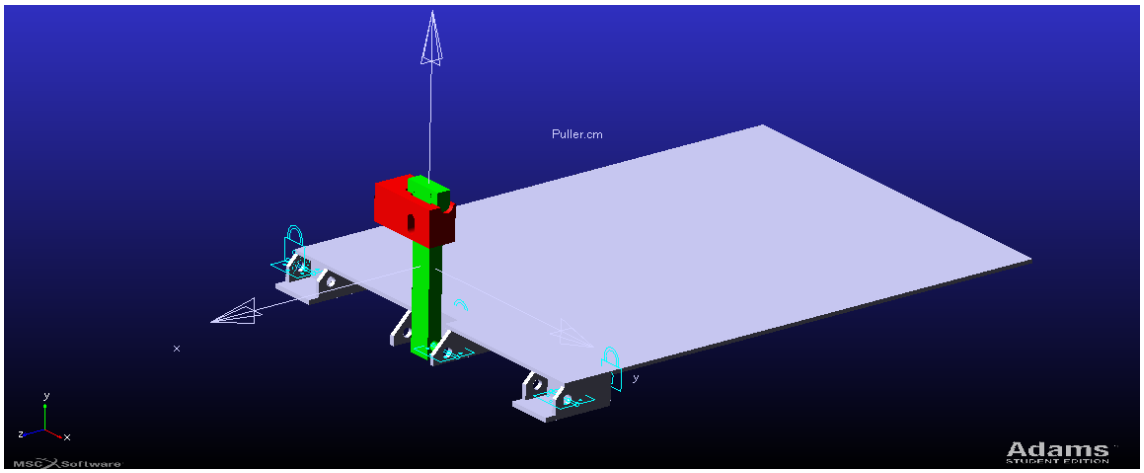

Figure 6.5: The simplified model of the louver in the Adams workspace, composed of the blade and its support structures (grey elements) and the pulling structure (green color for the puller main body, red color for the puller anchor); the louver is here displayed in its nominal open configuration.

The hinges between the louver and the external rails (not included in the model and identified with the ground of the workspace) are modeled as revolute joints throughout the analysis, with an initial zero value for friction; the effect of friction is later added as the model is refined for more complete analyses.

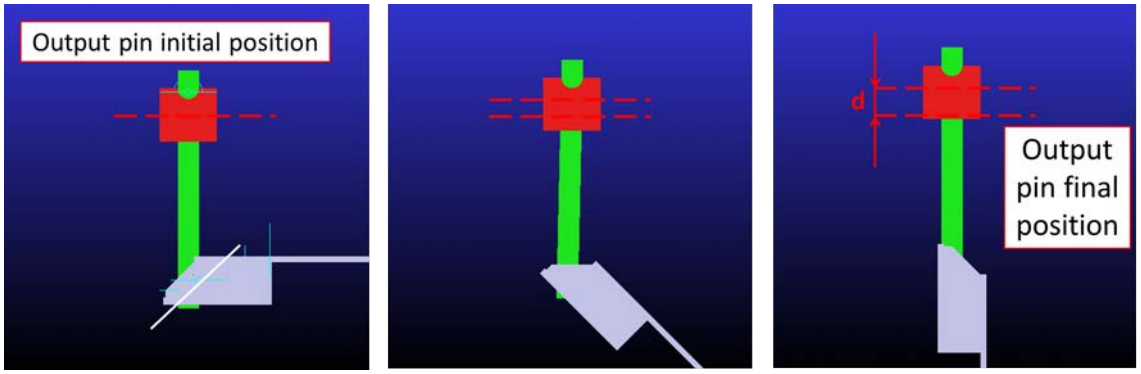

Figure 6.6: The closing sequence of the louver from a lateral point of view, showing that the lever system works as expected.

Fixed joints connect the various elements of the moving blade structure: they act between the hinges and the lever bodies and the blade. Given the rigid-body nature of the analysis, the stiffner included in the detailed description of section 6.2 is not a part of the model, in order to reduce the complexity and keep the number of bodies as low as possible. As a first step in the analysis, the contact surface between the puller and the anchor is also modeled as a revolute joint, simplifying the behaviour of the assembly, just to verify the correct relative position of the axes of the hinges and verify that the system is able to complete a 90 degrees rotation around the x-axis (with reference to the frame included in figure 6.5) with a maximum displacement of 3 mm along the y-axis of the anchor element (marked in red in the figure). Figure 6.6 shows a lateral view of the louver in three different angular positions during the closing operation; respectively, they represent the starting point (normally open condition) with an angle of 90 degrees between the blade and the non-displayed external CubeSat panel, the intermediate point, with an angle of 45 degrees and the maximum angular displacement of the puller from the initial vertical position, and the final point, with the blade parallel to the direction of the puller.

Figure 6.7 shows the time history of the displacement along y-axis for the anchor and the according rotation of the louver. The time duration of the closing operation is chosen to be 10 s, representing the functioning of IRESA in vacuum conditions. The displacement of the anchor is modeled as a Haversine step function. As visible from the plot, this first, simple simulation confirms that the design is correct and that the simplified model performs as expected.

The analysis is continued by refining the model in terms of connections, as the revolute joint between the puller body and the anchor is replaced with a more realistic contact force between the two bodies, letting the geometry alone account

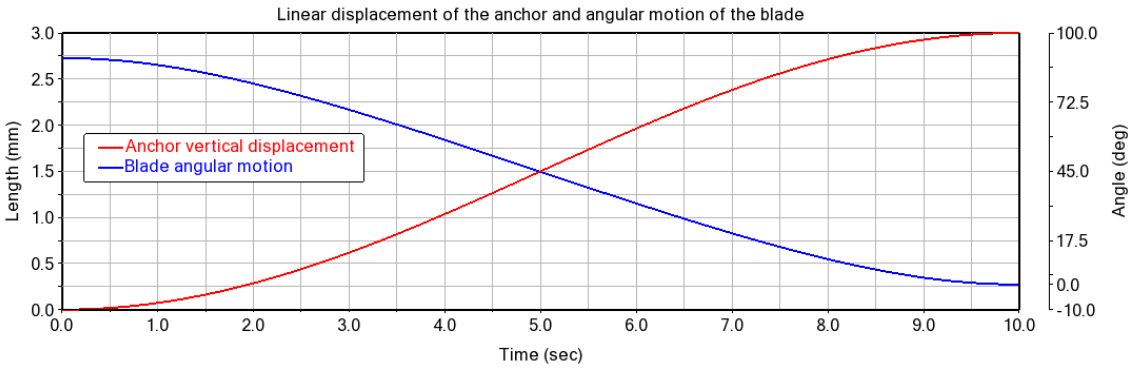

Figure 6.7: Time histories from the first simulation, showing the correct functioning of the mechanism under the hypothesis of ideal joints.

for the relative motion instead of creating ideal constraints.

By setting the contact parameters properly, the mechanism proves it functionality even in this case; the insertion of a torsional spring (for which K = 2.0×10^4 Nmm/deg) and of a friction force between the two materials (Coulomb friction, with $\mu_s = 0.2$ and $\mu_d = 0.1$) acting against the pulling motion is necessary in this case, due to the removal of a vertical constraint previously applied through the revolute joint.

The results obtained with this modification are shown in figure 6.8, where the angles followed by the puller are reported: the small difference between the two curves is due to a non-perfect behaviour at the beginning of the motion, where the model containing the contact surface exhibits small transverse translations which are damped by the preload in the continuation of the closing. The difference between the two angles is in any point lower than 0.05 degrees, therefore proving that the adopted contact region successfully resembles and ideal hinge and allows for a small rotation of the puller along its translation.

The final analysis performed on the mechanism addresses the dynamic behaviour of the system, when the friction of the hinges and a realistic value for the rate of the torsional spring are introduced in the system, with a new value of K = 0.02 Nmm/deg. The choice for the proper rate is based on the functioning of the system: since the puller is only able to transmit force and motion in the positive y-axis direction, a countermeasure must be adopted for the opening phase of the louver; following the realistic behaviour of the IRESA board, the opening phase is at least one order of magnitude longer than the closing operation, and during this phase the anchor is taken back to its initial position. The puller shall in any moment be kept adherent to the anchor, in case the louver needs to be operated again, and the

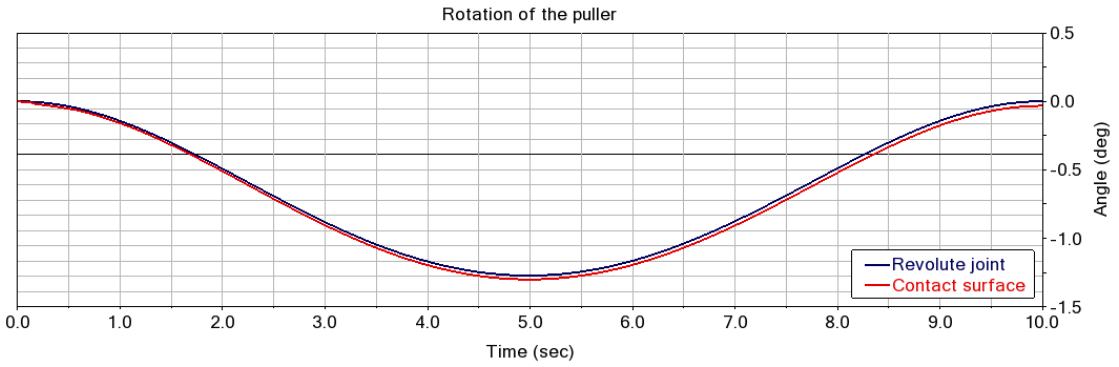

Figure 6.8: The rotation of the puller obtained with the two different models for the connection between the two elements.

minimum value of the rate is the one that guarantees this result.

6.4 ECSS standards for spacecraft mechanisms

In order to be qualified to operate on a spacecraft, mechanical assemblies shall comply to specific regulations in terms of ratio between worst case performance and expected nominal performance, material selection, interactions between different materials, friction and lubrication and vibrations. The design of the thermal louver mechanism presented in this thesis was carried out taking as a reference the ECSS-E-ST-33-01C Rev.1 standard [30], which summarises the most important aspects to be taken into account.

The crucial element to be assessed in this case is the available torque margin between the maximum expected required performance of the system and the maximum available output from the actuator itself; in this case IRESA produces a linear displacement and data are available for the maximum force output, but the output torque available at louver level is easily computed knowing the configuration of the simple lever at the base of the mechanism design, as presented in section 6.1. It is to be noted that by removing the output disk and the tribological issues associated with it, the available maximum torque for a generic application increases as the whole force output of the actuator can be exploited. The available torque is found by considering the average 19 N force previously introduced in table 3, and a lever L between the application point and the hinges on the rails of 1.5 mm, as a worst case; with these values, the obtained torque is:

$$T_{av} = F_{av} \times L = 19 \text{ N} \times 1.5 \text{ mm} = 28.5 \text{ Nmm}$$

Symbol	Complete name	Further specifications
I	Inertia	Inertia resistive torque applied when acceleration occurs (e.g. spinning spacecraft)
S	Spring	Spring torque at maximum value
H_M	Magnetic effects	
F_R	Friction	
H_Y	Hysteresis	
H_A	Others	Other torque sources (e.g. harness)
H_D	Adhesion	
T_D	Torque due to acceleration function	Torque employed to follow a specific acceleration profile for the moving element
T_L	Deliverable output torque	

Table 9: List of torques included in equation 6, with the same nomenclature presented in the E-ST-33-01C Rev.1 standard [30] regarding spacecraft mechanisms.

The values of the expected torques used in the calculations of the margins were taken from the previous analysis process. ECSS standard provides the following formula to calculate the minimum torque required in normal operation:

$$T_{min} = 2 \times (1.1I + 1.2S + 1.5H_M + 3F_R + 3H_Y + 3H_A + 3H_D) + 1.25T_D + T_L \quad (6)$$

where each torque source expressed in capital letters is accompanied by the relative safety factor; a reduction of the factors could be achievable when using measured instead of theoretical data, which is not the case in this preliminary evaluation process.

A list of the torques included in the equation is reported in table 9. In this case, the only non-zero elements that are considered are the spring torque S, the friction torque F_R and an hypothetical torque due to inertia I, by applying a random value of rotational speed to the satellite and accounting for the effect of the centrifugal force on the panel: given the operative configuration of the louver, a spin of the satellite would tend to drag the panel to its fully open condition, perpendicular to the side wall. An estimate of this force is used, and the worst case of 2 rpm for

the spin of the satellite is considered to determine the numerical value. No holding torques are needed in addition to the counteracting effect of the bias torsional spring since no other force is acting on the louver, so the term is neglected in the equation. Simplifying the neglected terms, equation 6 takes the form:

$$T_{min} = 2 \times (1.1I + 1.2S + 3F_R) \tag{7}$$

and finally substituting numerical values derived from calculations and analyses it yields:

$$T_{min} = 2 \times (1.1 \times 0.0031 + 1.75 \times 2.1 + 3 \times 0.969) \text{ Nmm} = 10 \text{ Nmm}$$

With traditional actuators, an high output (and therefore margin) usually corresponds to higher power consumption and larger mass to be introduced into the system; in the case of IRESA, and in general of SMA mechanisms, this problem is not encountered, as a high margin is still obtainable while maintaining low power requirements and low mass, due to the high force-per-unit-mass output provided by this technology.

7 Manufacturing, integration and testing

This section concludes the discussion relative to the mechanical characterisation of the system, completing the overview with the results obtained during the final integration of the prototype and the first functional tests of the mechanism.

7.1 Prototype integration

After the phase of detailed design of the prototype, the single components were manifactured at the workshops of the Technical University of Munich. The final finishing of the various components was not refined as in a potential flight model of the experiment, and the louver blade in particular was left unpolished at this stage of prototyping, given the purely mechanical verification purposes of the experiment. In specific all the parts of the assembly presented in section 6 were machined and produced correctly, except for the anchor of the puller, for which a slight production defect occurred.
The first assembly of the components was aimed at targeting potential problems arising from incorrect tolerances, especially in the smaller components; in particular, the following elements were checked and assessed during the first assembly and disassembly procedures:

- the geometry of the components, verifying the shape of the elements in order to detect possible production defects;
- the position, diameter and depth of the threaded holes, in particular the ones on the components of the blade;
- the fit of the bolts of the hinges, of particular concern in order to guarantee the smallest possible amount of friction;
- the effect of misalignments in the external frame on the hinges of the louver, with the potential risk of an increase in friction and a prevented rotation for the blade;
- the correct positioning of IRESA on the external frame, assessing the matching between the moving parts of the actuator and the puller element of the louver.

Once assessed the correct fit of the bolts, the assembly of the louver was carried out, securing the aluminum blade, the support structure and the hinges together.

Finally, the external frame was assembled making sure that the louver was properly hinged and held in position by the joints.

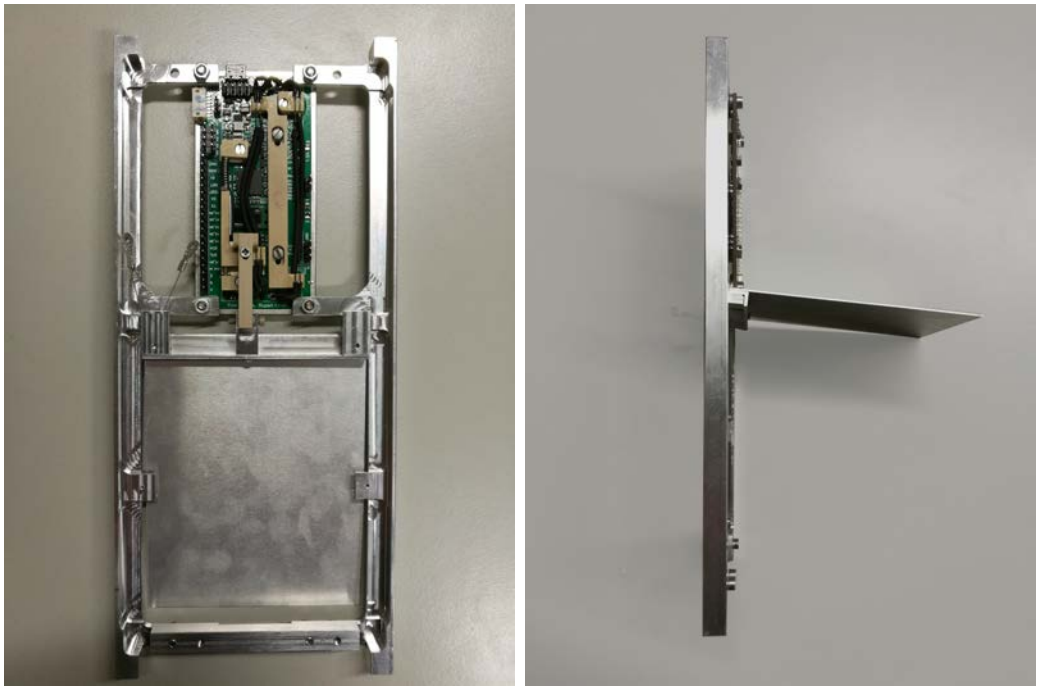

Figure 7.1: A front (left) and a side (right) view of the complete assembled prototype; the front view displays the louver in its completely closed configuration, while the side view allows to see the open blade, although the opening angle does not correspond to the nominal 90 degrees due to mechanical interference.

A proper clearance between the louver and the frame was assessed, in order to allow rotation without frictional sliding on the CubeSat rails.
The following procedure consisted in adding the actuator to the system, finalising the assembly. Before being mounted on the frame, IRESA underwent a minor intervention which consisted in the removal of the unnecessary output pin, which is replaced in this design by a screw having the same function, and of external pins used for debugging procedures, due to the non compatibility with the aluminum frame.
After the insertion of the actuator, the problem with the defected component was targeted, and a solution to the issue was found by directly attaching the connection element (puller) between the louver and the actuator directly to the floating bearing of IRESA: the PEEK component was screwed to the bearing and held in position by sufficient preload, in order to avoid any translation during operations. This adaptation of the design was necessary in order to perform the functional tests in time, due to the impossibility to manifacture new components.

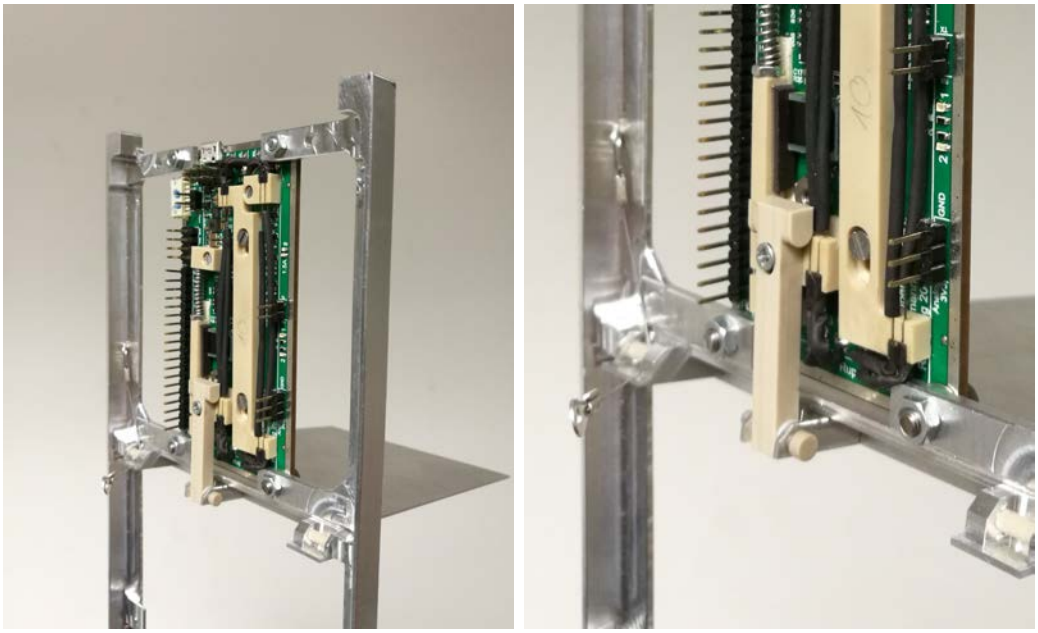

Figure 7.2: A side view of the prototype, which allows to see the mechanics of the louver and the lever system (left) and a closer view on the mechanical connection between IRESA and the louver (right): in this picture the alternative mechanical connection through a simple screw is visible, in replacement of the defected connector.

It is to be pointed out, moreover, that even it the fully open condition the blade is not able to reach a 90 degrees angle with respect to the frame, due to the larger edge fillets adopted for the CubeSat rails for the sake of faster manifacturing: this issue is totally absent in the design and it is expected to be eliminated in future prototypes matching more properly the specified tolerances. A result close to the nominal condition is reached anyway, and the panel is able to open enough to allow a proper testing phase.

In addition, at a first attempt IRESA and the louver did not match perfectly, and due to the slight misalignment of the hinges caused by the actuator attached to the external frame the louver was no longer able to open and close, and a strong friction occurred during the rotation; in this case the design proved to be adaptable and able to counteract the issue, simply allowing to operate a small adjustment from the screws of the two hinges. After this adjustment the louver was able to perform as expected and the friction reduced to the initial level.

This finding further confirms that the chosen design strategy not only allows for easier and faster manufacturing but also improves the performance of the system, making it versatile and able to tolerate misalignments coming from the integration

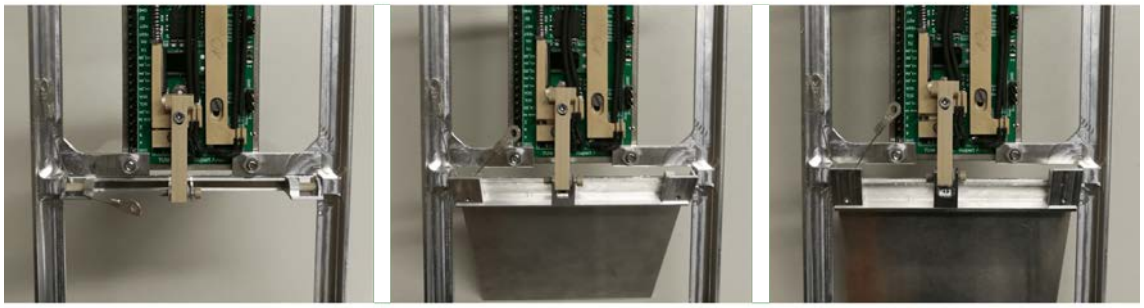

Figure 7.3: A detail of the mechanical interface for three different angular positions of the louver, showing the displacement of the puller for every angle.

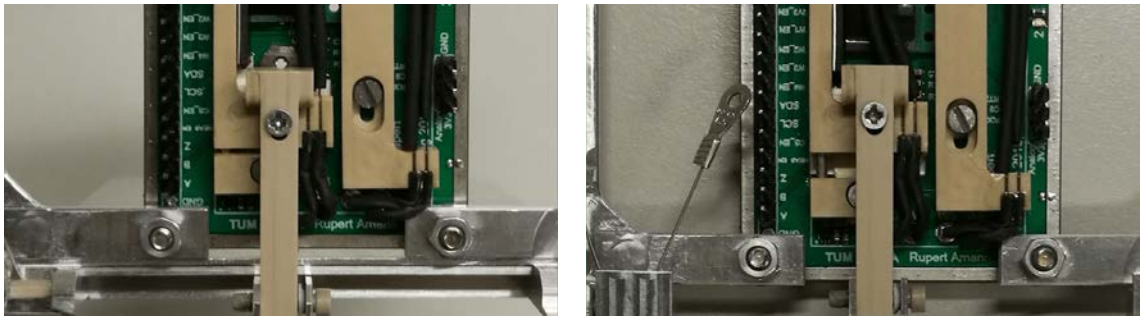

Figure 7.4: A closer detail of the puller which connects IRESA and the louver: in this case the displacement of the floating bearing is forced by a manual closing of the blade and the actuator is not operated; the two reported configurations correspond to a completely open (left) and a completely closed panel (right).

process of a potential satellite. Figures 7.1, 7.2, 7.3 and 7.4 show different details of the assembled prototype, illustrating its main components.

7.2 Functional testing

The second part of the integration and verification process was focused on the functioning of the louver, and in particular to the performance of the lever system, assessing the impact of manifacturing and non-perfect assembling on the small distances involved in the lever. The performance of the louver was evaluated by running a complete actuation cycle on IRESA, and observing the subsequent rotation induced on the blade. The experimental set-up with the louver completely open is presented in figure 7.5 with a brief description of the main elements: the picture also shows the loss of range of motion due to the mechanical interference between the blade and the edge fillets of the structure, which accounts for approximately 10 degrees.

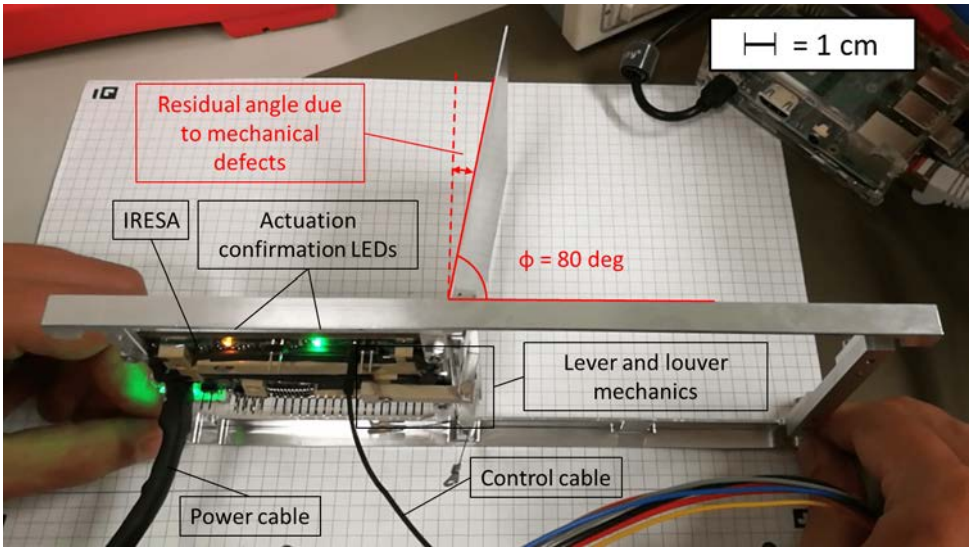

Figure 7.5: The experimental set-up used for the functional test of the louver.

The sequence of images 7.6 and the plot of figure 7.7 both show the behaviour of the system: the louver is completely open in its initial state, which corresponds to an angle ϕ of 80 degrees, and the actuator is in its reset mode (SMA wires fully elongated); as soon as the contraction begins the blade starts to follow its nominal rotation profile as expected. The closing operation proceeds fast until an angle of approximately 30 degrees is reached, and then the speed of actuation dramatically decreases: this phenomenon is due to the already presented features of the actuation in presence of atmosphere, and the last part of the contraction is slower because of the efficient convective cooling counteracting the Joule effect.

After a slow final part, the louver stops at an angle approximately equal to 5 degrees, therefore not completing a full closing. The second part of the cycle starts from this position and proceeds smoothly until an almost complete opening is reached: the non-perfect opening is mainly due to the aforementioned contact between the blade and the frame, and also to the residual contraction present in the SMA wires, which is expected to be counteracted by the torsional spring at the hinge of the louver, absent at this stage of testing. The total opening and closing procedure lasted approximately 93 seconds, and the maximum closed condition was reached after 55 seconds from the beginning of the procedure.

The plot of figure 7.7 summarises the previous description of the sequence, and in particular it emphasizes the characteristic behaviour of actuation in atmosphere: both in the closing and opening the first part of the curve has a relatively high slope, which decreases toward the end of the operation. Observing the total ob-

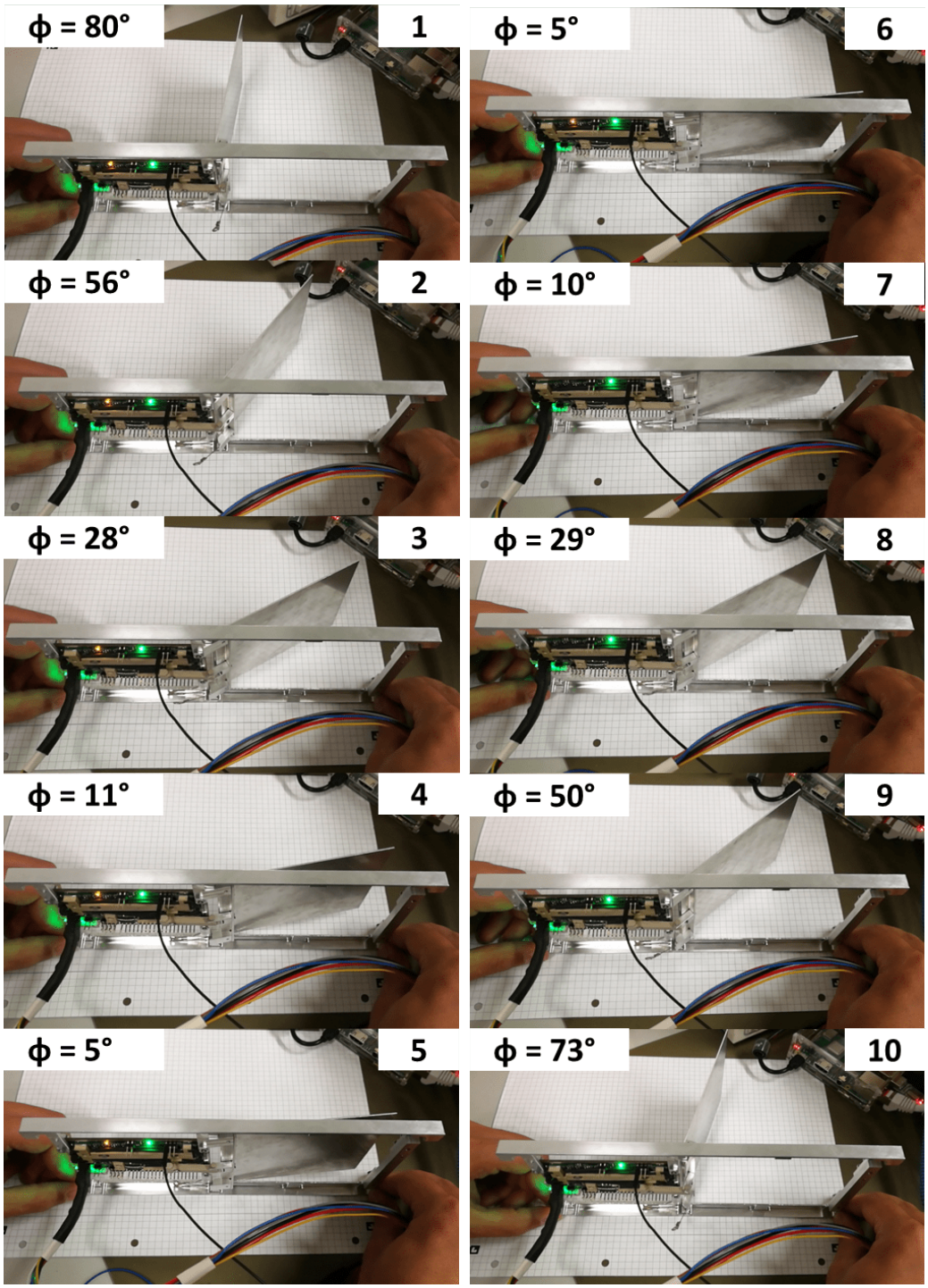

Figure 7.6: The complete sequence of the first functional test of the louver: the first series of frames (left column) depicts the closing phase spanning an angle of approximately 75 degrees; the second series of frames (right column) shows the opening of the louver, spanning a slightly smaller angle of approximately of approximately 68 degrees.

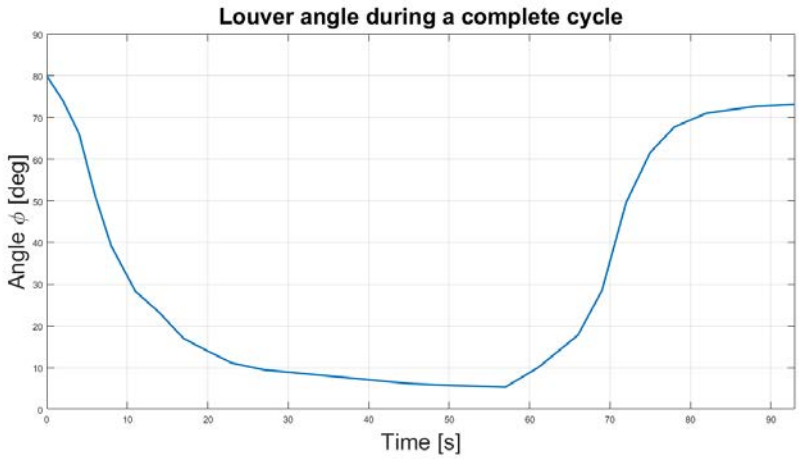

Figure 7.7: The closing and opening of the louver over time, showing the faster first part of the two phases and the decrease in slope as the two extreme positions are approached.

tained rotation, a range of motion of approximately 75 degrees was achieved, but as previously addressed in this section part of the responsibility resides in mechanical interference between the blade and the frame rather than a non-perfect functioning of IRESA: this effect accounts for the subtraction of about 8-10 degrees from the nominal open configuration at 90 degrees; the residual angle (approximately 5 degrees) in the closed position is instead the result of a combination of a non-complete contraction of the actuator and of the effect of mechanical tolerances on the small components, lowering the efficiency of the mechanics of the lever for ϕ approaching to zero.

In conclusion, this functional test proved that the adopted safety margin of 0.5 mm was necessary in order to reject mechanical imperfections arising from manifacturing and assembling, allowing the system to achieve an almost complete functioning from the first actuation; a better result in terms of range of motion is easily obtainable with a more refined manufacturing of the external support structure, allowing a complete opening of the panel. Moreover, the mechanism seems to tolerate quite well the absence of the anchor element providing rotation capability to the puller, without the occurrence of excessive stress on the bolt of the lever due to the stiffer structure and with no noticeable effect on the rotation of the louver. Therefore, it could be possible to implement a variant of the system in which the anchor is not present and a torsional spring at the hinge of the louver is no longer necessary, further reducing the complexity of the mechanism.

8 Conclusions

As a conclusion of this work of thesis, some of the most important aspects of the development process are remarked and summarised, giving a final overview on the accomplished results. As a last contribution to the work, some possible enhancements to the current design and possible peculiar implementations are provided as a cue for future works.

8.1 Final considerations

After a first necessary study on the physical properties of the particular materials involved in the project and their use inside IRESA, the main efforts were shifted towards the development of new technology in order to prove the versatility and the possibilities offered by the innovative actuator.
The choice to work on a thermal subsystem came mainly from the extreme compatibility of the thermal field with the working principle of the actuator, its range of motion and its operation speeds. In particular, the interest fell into the adaptation of a system able to provide a large range of power emissions to a spacecraft radiator of small size, as not many examples are found for this type of technology in the sector of small satellites and CubeSats. The possible breakthrough of the newly developed technology, or part of it, could help the development of more elaborate systems based on the same principle. The choice to design an active thermal subsystem is also unusual, and it is only possible because of the unique properties of the SMA in general and the actuator in specific, as most of the other morphing external surfaces dedicated to thermal control rely on passive and simpler means of actuation.
The various steps in the first part of the development, dealing with preliminary thermal considerations and with a simplified thermal characterisation of the subsystem, led to a coherent final mechanical design, which constitutes a trade-off between the thermal performance, the reduced mechanical complexity and the fulfillment of the requirements.
Particular attention was given during the design process to the mechanical tolerances to be specified in the technical drawings, especially considering the small size of the components of the assembly. Special considerations were required while designing the hinges and the bolts of the louver, crucial elements in the final functioning of the system.
After the manifacturing and integration steps, good results were obtained in terms

of functionality of the mechanism, even if some production defects were encountered and are expected to be removed in future versions of the same assembly, as they derive mainly from issues linked to production and they are not flaws in the final design. However, the system proved to be versatile and flexible, tolerating the presence of the defects and making the test procedures possible even if with some limitations. The first functional test run on the mechanism provided positive results, showing a good functioning of the system in laboratory conditions. Further test procedures are scheduled for the system in order to assess its capabilities in a vacuum environment and also its structural strength during the proper vibration analyses, necessary for the qualification of the technology for space.

8.2 Future developments

This final section introduces a short selection of possibilities for a future evolution in the design of the subsystem, as well as examples of how the current design could be integrated differently than the version presented in the previous section, showing the suitability of the current design for more complex applications or configurations. The current design of the subsystem is the result of the considerations made in sections 4, 5 and 6, and it can be summarised as a synthesis of both thermal and mechanical aspects, keeping as a main requirement the reduction of complexity while maintaining a reliable performance. The choice to simplify the louver to a single, large blade brings advantages, as already seen, in terms of efficiency of radiation to open space, reducing the obtrusion caused in other louvered surfaces by the presence of multiple blades; a larger number of blades reduces the maximum dissipation capability of the radiator, and causes other problems such as solar rays entrapment and multiple reflections, which lead to a further decrease in the amount of heat to be rejected.

However, if a classical, multi-blade configuration is chosen for a specific TCS, the efficiency in terms of motion provided by the lever system leaves room for further developments, allowing for the implementation of an array of blades moved by IRESA more similar to the common louvers. A concept of this adaptation is shown in figure 8.1, and its working principle is very similar to the one presented so far: as seen from the schematic design, the blade of the system closer to the actuator corresponds exactly to the single blade developed in this thesis, but with a lower size and mass. The following blades are rigidly connected to the first one, and they are actuated simultaneously via the connecting element without possibilities of reciprocal motion.

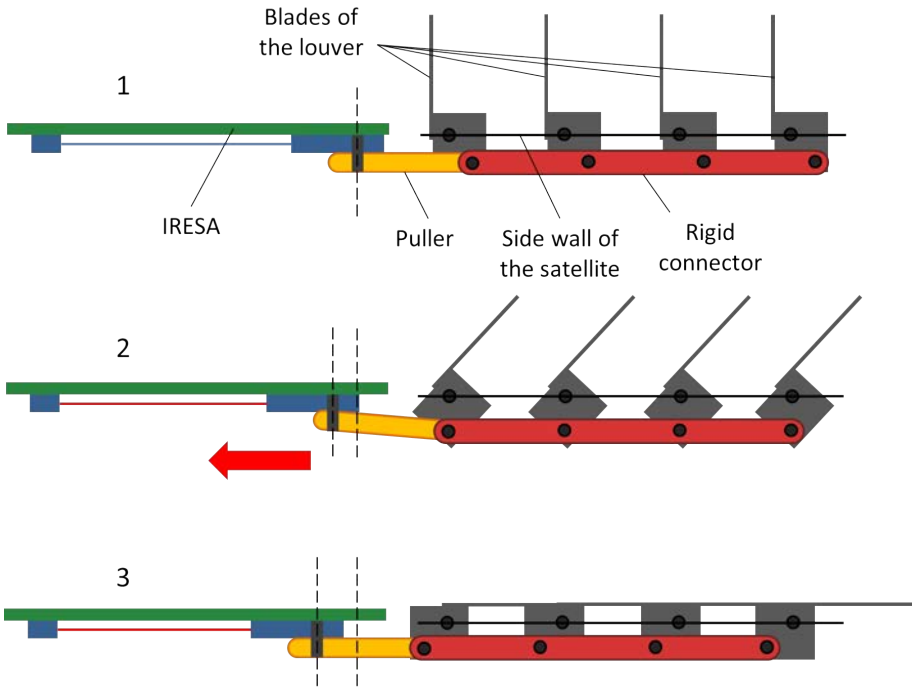

Figure 8.1: A louver system operating with the same principle presented in the previous sections but consisting of multiple blades, actuated at the same time by IRESA.

In this case, one hinge of each louver is rigidly connected to the structure of the satellite (represented by the black thick line in the figure) while the hinges linked to the red connector perform replicating the rotation of 90 degrees shown in the previous mechanical design sections.

Such a solution is as versatile as the single blade variant, given the simple addition of a connector and of extra blades, and it is adaptable to different sizes and configurations. The major drawback of a single actuator providing motion to all the blades is the lack of redundancy which characterises the typical, passive spring-actuated louvers, in which potential malfunctions of one or more units are only responsible for a decrease in the efficiency of the system rather than for a complete fail. On the other hand,The advantage of combining an active control system and the classical configuration is an increase in precision for the whole system, as the required angle for the blades can easily be reached given the features of IRESA.

The same result of a better shielding to the solar radiation can be achieved without modifying the current design and keeping the complexity as low as possible, if the surface at disposal is large enough to allow a smart arrangement of multiple actuator-louver assemblies. Also, an inversion in the reciprocal position of the puller element

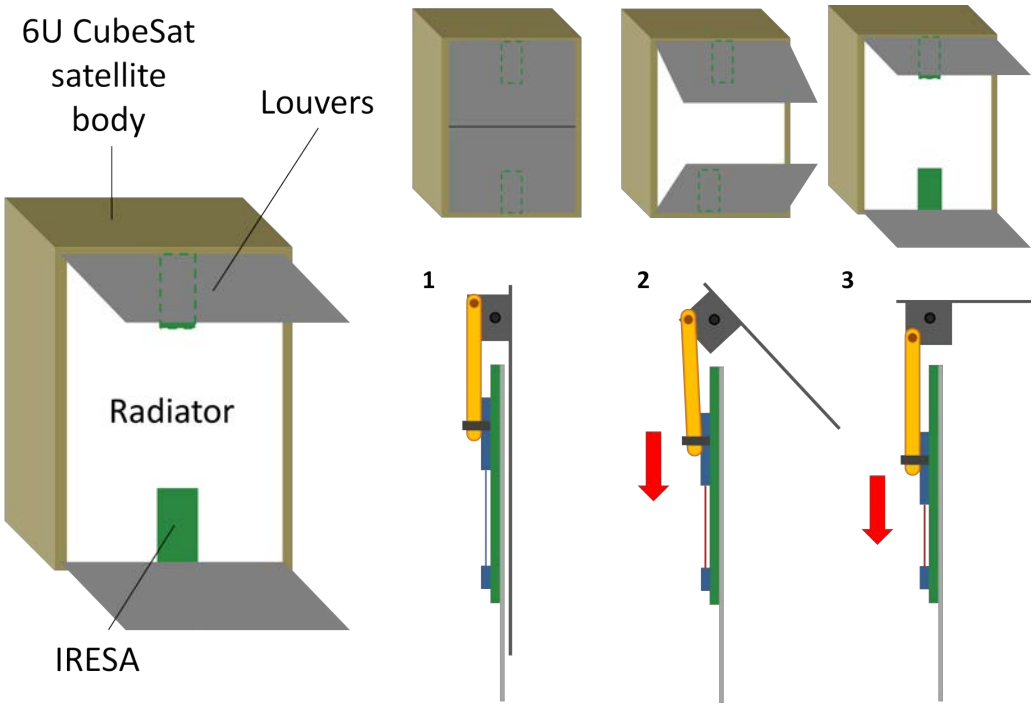

Figure 8.2: The adapted design of the mechanism in order to be suitable for a more elaborate arrangement of the louvers on the panel of a larger satellite; the working principle remains unchanged even if the position of the elements is inverted in this variant.

and the hinge of the louver is perfectly possible with the current design, without any modification to the components. These features are presented in figure 8.2, where the preliminary design of different arrangements on the surface of a 6U CubeSat are shown. This particular configuration resembles in its geometry a deployable radiator, given the large panels opening to expose the underlying radiating surface. This solution is particularly indicated to counteract the effect of solar radiation hitting the radiator with an intermediate incidence (approximately $\theta = 45$ deg or $\theta = 135$ deg, with reference to the angles used in section 5), providing a better shielding for the emitting surface but causing an increase in the view factor between the radiator and the protruding surfaces.

The last proposed implementation introduces a concept of hybridisation between the presented thermal control system and the solar arrays of the power system: in particular, if the system is expected to operate with conditions of illumination for part of the orbit, it could prove beneficial to install some of the solar cells on the external surface of the louver, which provides enough flat space and no obtrusion. This solution is particularly useful if the louver is employed as a sun shield, as this

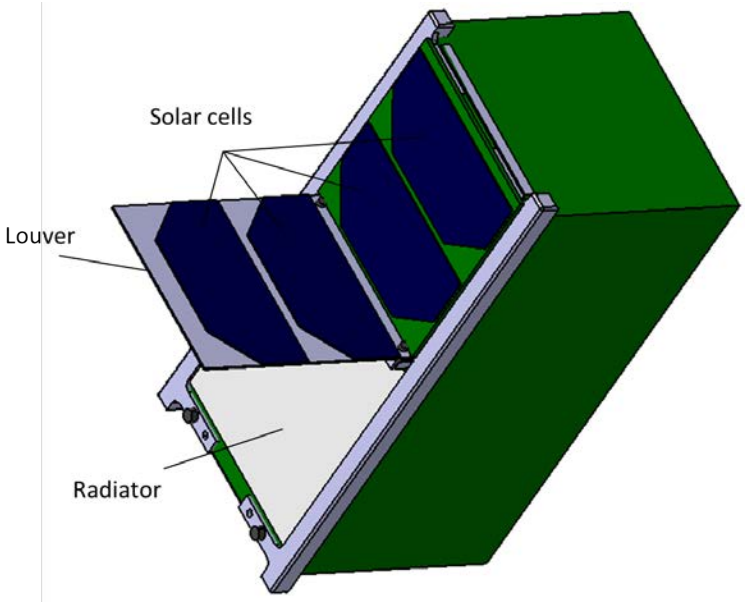

Figure 8.3: The concept of the hybrid system obtained by installing solar cells on the external part of the louver, also showing the underneath white painted radiator.

would automatically place the outer surface in a privileged position and orientation to receive the solar impingement. Figures 8.3 and 8.4 show a concept of the hybrid system, displaying the solar cells mounted on top of the external blade. Solar cells would also be mounted on the rest of the satellite, but they are omitted in the figure for the sake of simplicity.

Of course the implementation of this solution would require proper calculations and to find a trade-off between the maximum thermal power to be dissipated and the efficiency of solar illumination for the solar cells, nonetheless further developments could show a positive impact of the combined technology on the performance of the

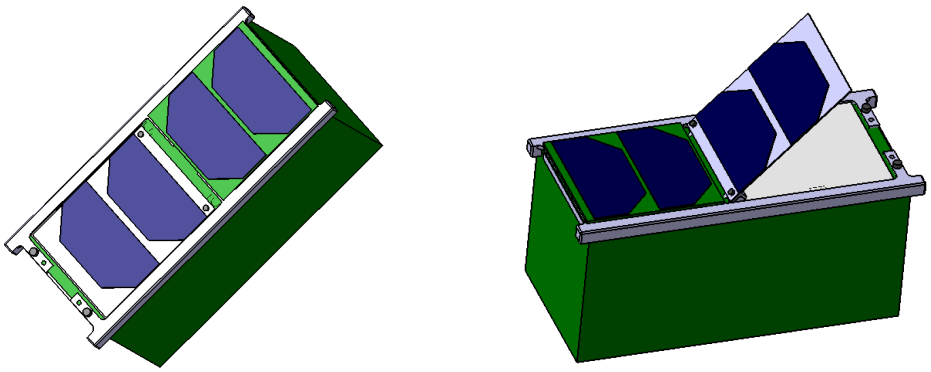

Figure 8.4: Two additional different configurations for the hybrid system, showing a completely closed (left) and a half open panel (right).

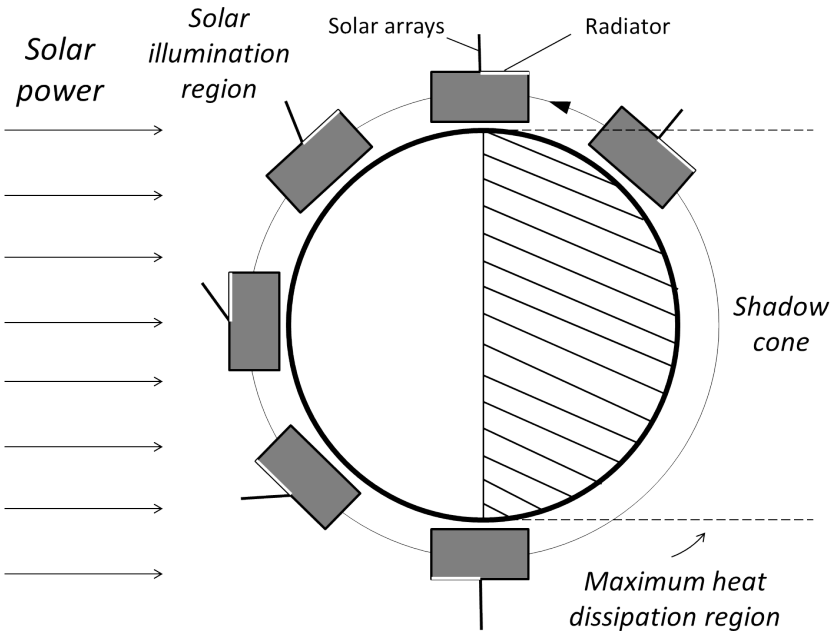

Figure 8.5: A possible orbit (noon-midnight) in which the system could operate, given its particular characteristics.

satellite. Figure 8.5 shows a simple case of application for this solution, considering a Low-Earth, noon-midnight orbit and a non-spinning satellite: during a large part of the illuminated portion of the orbit the louver-solar array could be controlled in order to fulfill both its task in the most efficient way.

Appendices

A Antenna preliminary calculations

This section contains the simple equations used for the preliminary calculations of the quantities included in table 4. Most of the equations derive from the well known, simplified formulas for circular orbits. The first parameter to be calculated from the given altitude h of 500 km is the true anomaly of the first point of the orbit useful for communication purposes:

$$\gamma = \cos^{-1}\left(\frac{R_E\ \cos\xi}{R_E + h_o}\right) - \xi = \cos^{-1}\left(\frac{6378\ \cos 5}{6378 + 500}\right) - 5 = 17.51 \text{ deg} \tag{8}$$

The linear angular velocities along the circular orbit is determined through astrodynamics:

$$v_{orb} = \sqrt{\frac{\mu}{R_E + h_o}} = \sqrt{\frac{398600}{6378 + 500}} = 7.61 \text{ km/s} \tag{9}$$

$$\omega_{orb} = \frac{v_{orb}}{R_E + h_o} = 1.1 \times 10^{-3} \text{ rad} \approx 0.063 \text{ deg/s} \tag{10}$$

The total link time is finally computed as follows:

$$\Delta t_{link} = \frac{2\gamma}{\omega_{orb}} \approx 346 \text{ s} \approx 11 \text{ min} \tag{11}$$

When dealing with link availability for a generic spacecraft in orbit both the orbital angular velocity ω_{orb} and the angular velocity of the ground station due to the rotation of the earth should be considered; however, in the case of a LEO the rotation of the planet can be neglected since it is much lower than the orbital one. Therefore the calculation in equation 11 still holds true with good approximation. From this preliminary calculation the angular range of motion of the antenna is also derived, being found as:

$$ROM = 2\delta = 2 \times [90 - (\gamma + \xi)] \text{ deg} \approx 135 \text{ deg} \tag{12}$$

Finally, the angular speed of the antenna during pointing operations is found through the simple formula:

$$\omega_{pointing} = \frac{2\gamma}{\Delta t_{link}} \approx 0.39 \text{ deg/s} \tag{13}$$

B View factors equations

This appendix contains the equations used in section 4 to calculate the view factors between the two rectangular surfaces representing the radiator and the louver. The equations and formula contained in these appendices are taken from the catalog indicated in reference [29], and reported with the same terminology adopted in the original source.

B.1 Rectangular, tilted surfaces of generic dimensions sharing one edge

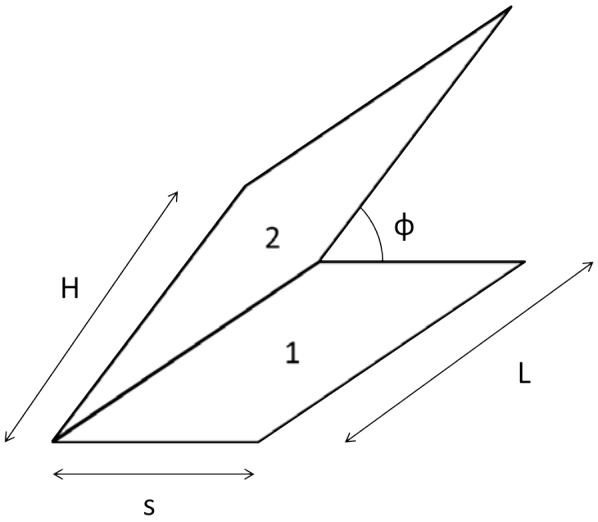

Figure B.1: The two rectangular surfaces 1 and 2 share one edge, are tilted by an angle ϕ and have generic lengths s and H.

Figure B.1 shows a more complex configuration, in which two rectangular surfaces are facing at each other with a tilt angle ϕ and different dimensions, while sharing a common edge of length L. The generic formula for the view factor F_{12} (with particular importance on the respective numbering of the surfaces) is given in equation 14; the first part of the equation is obtained by analytical solution of the general integral applied to the case under examination, while the integral in the final part of the equation can not be solved exactly, and a numerical tool in MATLAB is used for calculations.

$$
\begin{aligned}
F_{12} = -\frac{\sin 2\phi}{4\pi B}\Bigg[& AB\sin\phi + (A^2+B^2)\left(\frac{\pi}{2}-\phi\right) + B^2\tan^{-1}\left(\frac{A-B\cos\phi}{B\sin\phi}\right) \\
& + A^2\tan^{-1}\left(\frac{B-A\cos\phi}{A\sin\phi}\right)\Bigg] + \frac{\sin^2\phi}{4\pi B}\Bigg\{\left(\frac{2}{\sin^2\phi}-1\right)\ln\left[\frac{(1+A^2)(1+B^2)}{1+C}\right] \\
& + B^2\ln\left[\frac{B^2(1+C)}{(1+B^2)C}\right] + A^2\ln\left[\frac{A^2(1+A^2)^{\cos 2\phi}}{C(1+C)^{\cos 2\phi}}\right]\Bigg\} \\
& + \frac{1}{\pi}\tan^{-1}\left(\frac{1}{B}\right) + \frac{A}{\pi B}\tan^{-1}\left(\frac{1}{A}\right) - \frac{\sqrt{C}}{\pi B}\tan^{-1}\left(\frac{1}{\sqrt{C}}\right) \\
& + \frac{\sin\phi\sin 2\phi}{2\pi B}AD\left[\tan^{-1}\left(\frac{A\cos\phi}{D}\right) + \tan^{-1}\left(\frac{B-A\cos\phi}{D}\right)\right] \\
& + \frac{\cos\phi}{\pi B}\int_0^B \sqrt{1+\xi^2\sin^2\phi}\left[\tan^{-1}\left(\frac{\xi\cos\phi}{\sqrt{1+\xi^2\sin^2\phi}}\right)\right. \\
& \left. + \tan^{-1}\left(\frac{A-\xi\cos\phi}{\sqrt{1+\xi^2\sin^2\phi}}\right)\right] d\xi
\end{aligned}
\tag{14}
$$

$$A = \frac{H}{L}$$

$$B = \frac{s}{L}$$

$$C = A^2 + B^2 - 2AB\cos\phi$$

$$D = \sqrt{1+A^2\sin^2\phi}$$

B.2 Rectangular, tilted surfaces of equal dimensions sharing one edge

The equations contained in this section represent a particular case of the equations for the two generic, tilted rectangular surfaces. Figure B.2 shows the configuration for which the two surfaces are inclined by the angle ϕ with respect to each other, but the two lateral edges are equal to each other and to a value H. The corresponding equation 15 is:

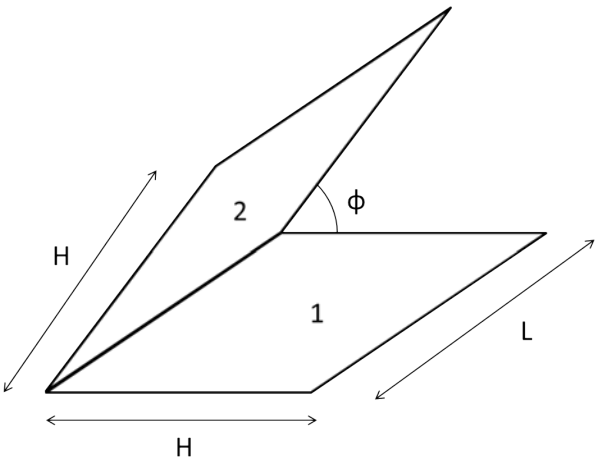

Figure B.2: The two rectangular surfaces 1 and 2 share one edge, are tilted by an angle ϕ and have the same length H.

$$
\begin{aligned}
F_{12} = &-\frac{\sin 2\phi}{4\pi A}\left[A^2\sin\phi + 2A^2\left(\frac{\pi}{2}-\phi\right) + 2A^2\tan^{-1}\left(\frac{1-\cos\phi}{\sin\phi}\right)\right] \\
&+ \frac{\sin^2\phi}{4\pi A}\left\{\left(\frac{2}{\sin^2\phi}-1\right)\ln\left[\frac{2(1+A^2)^2}{1+C}\right] + A^2\ln\left[\frac{A^2(1+C)}{(1+A^2)C}\right]\right. \\
&\left. + A^2\ln\left[\frac{A^2(1+A^2)^{\cos 2\phi}}{C(1+C)^{\cos 2\phi}}\right]\right\} + \frac{2}{\pi}\tan^{-1}\left(\frac{1}{A}\right) - \frac{\sqrt{C}}{\pi A}\tan^{-1}\left(\frac{1}{\sqrt{C}}\right) \\
&+ \frac{\sin\phi\sin 2\phi}{2\pi A}AD\left[\tan^{-1}\left(\frac{A\cos\phi}{D}\right) + \tan^{-1}\left(\frac{A-A\cos\phi}{D}\right)\right] \\
&+ \frac{\cos\phi}{\pi A}\int_0^A \sqrt{1+\xi^2\sin^2\phi}\left[\tan^{-1}\left(\frac{\xi\cos\phi}{\sqrt{1+\xi^2\sin^2\phi}}\right)\right. \\
&\qquad\left. + \tan^{-1}\left(\frac{A-\xi\cos\phi}{\sqrt{1+\xi^2\sin^2\phi}}\right)\right]\mathrm{d}\xi
\end{aligned}
\tag{15}
$$

But in this case the various parameters are simplified as follows:

$$A = \frac{H}{L}$$

$$C = 2A^2(1-\cos\phi)$$

$$D = \sqrt{1+A^2\sin^2\phi}$$

C Thermal model equations

This appendix section provides the fundamental equations used in section 5 to characterise the system and study its behaviour when different values are used for the thermo-optical properties of the surfaces. Figure C.1 reports a thermal model similar to the one of section 5, but more useful to clarify the hypotheses followed in the definition of the mathematical model. As a first thing to point out, the two surfaces of the louver are treated as two separate areas of power emission, as the internal portion interacts with the radiator while the external surface is only facing space when no external conditions occurs.

Therefore, the two surfaces can be treated independently while still accounting for the same thermal node associated with the louver: this choice generates a symmetry between the radiator and the interior of the blade, which possess the same emitting surface area and an identical reciprocal view factor F_{rl} in every angular condition; the exterior of the louver emits power as a simple object isothermal to the interior of the blade and with a surface equal to A_r, and it could be assigned a different value of emissivity or absorption coefficient with respect to the internal surface, in order to account for possible different coatings. These assumptions are at the basis of the simple thermal model adopted for the calculations and reported in equations 16 and 17:

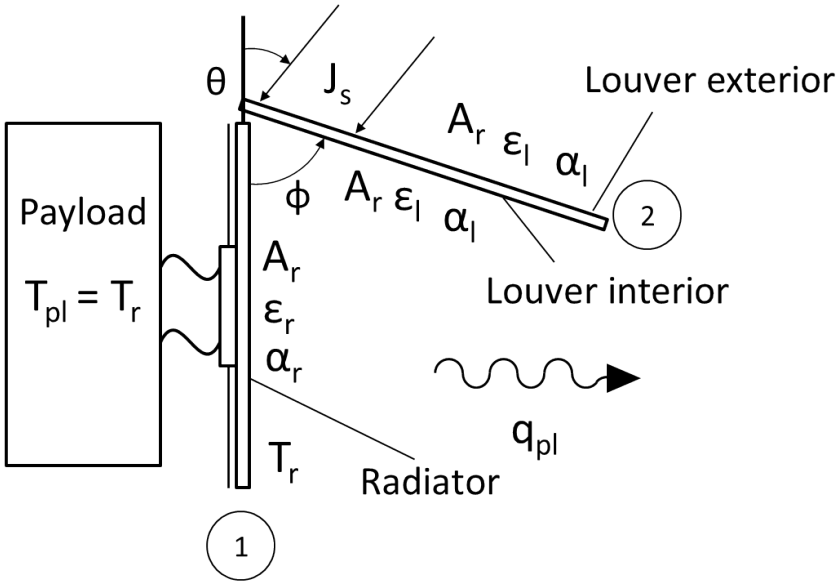

Figure C.1: The complete thermal model adopted for the calculations.

$$\begin{aligned} q_{pl} = \sigma_n \epsilon_r A_r T_r^4 \left[1 - \epsilon_r \sum_{n=1}^{N} (1-\epsilon_l)^n (1-\epsilon_r)^{n-1} F_{rl}^{2n} \right] \\ + \sigma_n \epsilon_l A_r T_l^4 F_{rl} \epsilon_r \left[1 + \sum_{n=1}^{N} (1-\epsilon_l)^n (1-\epsilon_r)^n F_{rl}^{2n} \right] \end{aligned} \tag{16}$$

$$\begin{aligned} 0 = -\sigma_n \epsilon_l A_r T_l^4 + \sigma_n \epsilon_r A_r T_r^4 F_{rl} \epsilon_l \left[1 + \sum_{n=1}^{N} (1-\epsilon_r)^n (1-\epsilon_l)^n F_{rl}^{2n} \right] \\ - \sigma_n \epsilon_l A_r T_l^4 \left[1 - \epsilon_l \sum_{n=1}^{N} (1-\epsilon_l)^{n-1} (1-\epsilon_l)^n F_{rl}^2 n \right] \end{aligned} \tag{17}$$

The two unknowns in these equations are q_{pl} and T_l, as T_r is set to 15°C as specified in the dedicated section; the sums contain in the equations express the multiple reflections and absorptions occurring between the radiator and the louver. For the simulations presented in this work a number of iterations N equal to 6 was adopted, providing a good convergence of the values. Keeping the number of reflections sufficiently large guarantees more accurate results especially for low values of ϕ, due to the large effect of the louver on the emission of the radiator.

The effect of solar impingement is added to the previous model as a series of extra terms introducing power into the system. First of all, a simple trigonometric formula (equation 18) allows to determine the portion of radiator experiencing direct illumination for every value of θ and ϕ, with reference to figure 5.2 and C.2: s is the length of the shade along the lateral side of the radiator, while l is the length of the illuminated region, obtained by subtraction from the total length of the radiator L_{rad}.

With these hypotheses, s is found:

$$s = \frac{\sin(180 - \phi - \theta)}{\sin(\theta) L_{rad}} \tag{18}$$

and of course l is immediately determined:

$$l = L_{rad} - s \tag{19}$$

The script performing the calculations automatically corrects the solutions with negative values of s or with a value of the shade larger than L_{rad}, ensuring the physical meaning of the terms.

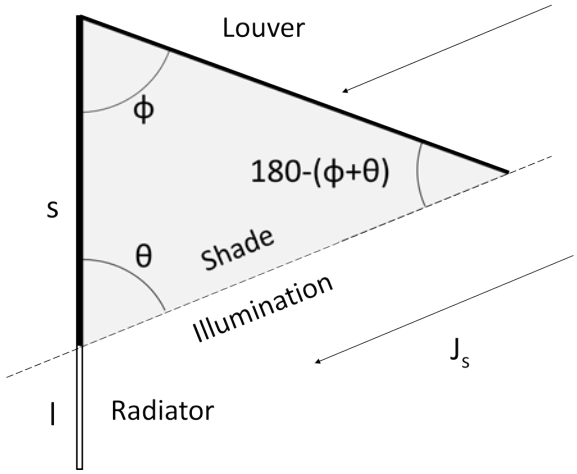

Figure C.2: The illumination and shade on the radiator and the various angles of the model.

Once the illumination is determined, the view factor between the shaded region of the radiator $F_{s\to l}$ is calculated with the equations of appendix B, and the view factor $F_{ill\to l}$ between the illuminated area and the interior of the louver is derived with equation 20:

$$F_{ill\to l} = \frac{A_r F_{rl} - A_s F_{s\to l}}{A_{ill}} \tag{20}$$

where A_s and A_ill are the areas found by multiplying s and l by the transverse dimension of the radiator.

The complete equations (equation 21 and 22, which expand the ones previously introduced and which include the effect of solar radiation are therefore obtained:

$$\begin{aligned} q_{pl} = {} & \sigma_n \epsilon_r A_r T_r^4 \left[1 - \epsilon_r \sum_{n=1}^{N} (1-\epsilon_l)^n (1-\epsilon_r)^{n-1} F_{rl}^{2n} \right] \\ & + \sigma_n \epsilon_l A_r T_l^4 F_{rl} \epsilon_r \left[1 + \sum_{n=1}^{N} (1-\epsilon_l)^n (1-\epsilon_r)^n F_{rl}^{2n} \right] \\ & + J_s A_r \sin\theta \ \alpha_r \left\{ 1 + F_{ill\to l} \left[\sum_{n=1}^{N} (1-\alpha_l)^n (1-\alpha_r)^n F_{rl}^{2n-1} \right] \right\} \\ & + RT \ J_s A_r \sin(180-\theta-\phi)(1-\alpha_l) F_{rl} \alpha_r \left[1 + \sum_{n=1}^{N} (1-\alpha_l)^n (1-\alpha_r)^n F_{rl}^{2n} \right] \end{aligned} \tag{21}$$

$$
\begin{aligned}
0 = & -\sigma_n \epsilon_l A_r T_l^4 + \sigma_n \epsilon_r A_r T_r^4 F_{rl} \epsilon_l \left[1 + \sum_{n=1}^{N} (1-\epsilon_r)^n (1-\epsilon_l)^n F_{rl}^{2n} \right] \\
& - \sigma_n \epsilon_l A_r T_l^4 \left[1 - \epsilon_l \sum_{n=1}^{N} (1-\epsilon_l)^{n-1} (1-\epsilon_l)^n F_{rl}^2 n \right] \\
& + J_s A_{ill} \sin\theta (1-\alpha_r) F_{ill \to l} \alpha_l \left[1 + \sum_{n=1}^{N} (1-\alpha_l)^n (1-\alpha_r)^n F_{rl}^{2n} \right] \\
& + J_s A_r \sin(180 - \theta - \phi) \alpha_l \left[1 + RT \sum_{n=1}^{N} (1-\alpha_l)^n (1-\alpha_r)^n F_{rl}^{2n} \right]
\end{aligned}
\tag{22}
$$

Equations 21 and 22 complete the description of the thermal model, giving the complete overview on how the software producing the plots of section 5 was implemented. The parameter indicated with RT (reflection trigger) is a binary element which can be assigned a value of either 0 or 1 during the calculation cycles, and it activates the reflection of light from the interior of the louver towards the radiator when the incidence θ is sufficiently low to allow the rays to hit the target surface.

References

[1] California Polytechnic State University. *CubeSat Design Specification (CDS) Rev. 13*. Available from http://www.cubesat.org/

[2] Kumar, P., K., & Lagoudas, D., C. (2008). Introduction to Shape Memory Alloys. In Lagoudas, D., C. (Ed.) *Shape Memory Alloys - Modeling and Engineering Applications* (pp. 3-7). Boston, MA: Springer

[3] Mohd Jani, J., Leary, M., Subic, A., & Gibson, M. A. (2014). *A review of shape memory alloy research, applications and opportunities*. Materials & Design (1980-2015), 56, pp. 1078–1113.

[4] Wu, M. H., Schetky, L. McD. (2000).*Industrial Applications for Shape Memory Alloys*. Proceedings of the International Conference on Shape Memory and Superelastic Technolgies, Pacific Grove, California, pp. 171-182

[5] Hartl, D. J., Lagoudas, D. C. (2007). *Aerospace applications of shape memory alloys*. Proceedings of the Institution of Mechanical Engineers, Part G: Journal of Aerospace Engineering. Volume 221, Issue 4 (April 2007), pp. 535-552. Retrieved from https://journals.sagepub.com/doi/pdf/10.1243/09544100JAERO211

[6] Peffer, A. C., Fosness, E. R., Carpenter, B. F., & Denoyer, K. K. (2000). *On-orbit experiments and applications of shape memory alloy mechanisms*. Proc. SPIE 3991, Smart Structures and Materials 2000: Industrial and Commercial Applications of Smart Structures Technologies

[7] Lake, M., Munshi, N., Meink, T., & Tupper, M. (2001). *Application of elastic memory composite materials to deployable space structures*. AIAA Space 2001 Conference and Exposition

[8] Stoeckel, D. (1990). *Shape memory actuators for automotive applications*. Materials & Design, 11(6), pp. 302–307.

[9] Benard, W. L., Kahn, H., Heuer, A. H., & Huff, M. A. (1997). *A titanium-nickel shape-memory alloy actuated micropump*. Proceedings of International Solid State Sensors and Actuators Conference (Transducers '97), Chicago, IL, USA, 1997, pp. 361-364 vol.1.

[10] Machado, L.G., & Savi, M.A.. (2003). Medical applications of shape memory alloys. Brazilian Journal of Medical and Biological Research, 36(6), 683-691. https://dx.doi.org/10.1590/S0100-879X2003000600001

[11] Haga, Y., Tanahashi, Y., & Esashi, M. (1998). *Small diameter active catheter using shape memory alloy*. Proceedings MEMS 98. IEEE. Eleventh Annual International Workshop on Micro Electro Mechanical Systems. An Investigation of Micro Structures, Sensors, Actuators, Machines and Systems (Cat. No.98CH36176, Heidelberg, Germany, 1998), pp. 419-424

[12] Pfeiffer, C., DeLaurentis, K., & Mavroidis, D. (1999). *Shape Memory Alloy Actuated Robot Prostheses: Initial Experiments*. Proceedings 1999 IEEE International Conference on Robotics and Automation (Cat. No.99CH36288C), Detroit, MI, USA, 1999, pp. 2385-2391 vol.3.

[13] Senf, B., Mäder, T., Navarro y de Sosa, I., Bucht, A., Knobloch, M., Löpitz, D., & Drossel, W.-G. (2017). *Sensing and Actuating Functions by Shape Memory Alloy Wires Integrated into Fiber Reinforced Plastics*. 1st Cirp Conference on Composite Materials Parts Manufacturing, cirp-ccmpm2017. Procedia CIRP 66 (2017) pp. 249-253

[14] Songa, G., Maa, N., Lib, H.-N. (2006). *Applications of shape memory alloys in civil structures*. Engineering Structures, Volume 28, Issue 9, July 2006, pp. 1266-1274

[15] Janke, L., Czaderski, C., Motavalli, M., & Ruth, J. (2005). *Applications of shape memory alloys in civil engineering structures — Overview, limits and new ideas*. Materials and Structures, 38(5), pp. 578–592.

[16] Lecce, L., & Concilio, A. (Ed.)(2014). *Shape Memory Alloy Engineering* (1st Edition)(pp. 1-50). Oxford, UK: Butterworth-Heinemann (Elsevier)

[17] SAES Getters S.p.A. *SmartFlex Wire and springs datasheets*, 2009. number: D.SMA.100.0.

[18] Schummer, F., Kale, T., Bachler, J., Amann, R., Langer, M., Roj, R., Langbein, S., Dültgen, P., & Czechowicz, A. (2018). *IRESA - Intelligent Redundant Spacecraft Actuator*. IEEE Aeroconf 2019

[19] Huang, W. (1998). *Shape Memory Alloys and their Application to Actuators for Deployable Structures* (Doctoral dissertation). Retrieved from http://www3.ntu.edu.sg/home/mwmhuang/cambridge/Phd2side.pdf

[20] Huang, W., Pellegrino, S., & Bashford, D. P (1996). *Shape memory alloy actuators for deployable structures.* Spacecraft Structures, Materials and Mechanical Engineering, Proceedings of the Conference held by ESA, CNES and DARA in Noordwijk, 27-29 March 1996. Edited by W.R. Burke. ESA SP-386. Paris: European Space Agency (ESA), 1996., p. 53

[21] Santoni, F., Piergentili, F., Candini, G. P., Perelli M., Negri, A., & Marino, M. (2014). *An orientable solar panel system for nanospacecraft.* Acta Astronautica, Vol. 101, August - September 2014, pp. 120-128

[22] Galatis, G., Guo, J., & Buursink, J. (2017). *Development of a solar array drive mechanism for micro-satellite platforms.* Acta Astronautica, Vol. 139, October 2017, pp. 407-418

[23] Grulich, M., Koop, A., Ludewig, P., Gutsmiedl, J., Kugele, J., Ruck, T., Mayer, I., Schmid, A., & Dietmann, K. (2015). *Smard-Rexus-18: Development and Verification of an SMA Based CubeSat Solar Panel Deployment Mechanism.*

[24] John E. Oberright (2011). Spacecraft Thermal Control. In Wertz, J. R., Everett, D. F., & Puschell, J. J. *Space Mission Engineering: The New SMAD* (pp. 698-699). Space Technology Library (Springer) in association w. Microcosm Press

[25] Bertagne, C. L., Cognata, T. J., Sheth, R. B., Dinsmore, C. E., & Hartl, D. J. (2017). *Testing and analysis of a morphing radiator concept for thermal control of crewed space vehicles.* Applied Thermal Engineering, 124, 986–1002.

[26] Hardt, B., E., Karam, R., D., & Eby, R., J. (2002). Louvers (pp. 331-352). In Gilmore, D. G. (Ed.). *Spacecraft Thermal Control Handbook, Volume I: Fundamental Technologies* (2nd Edition). El Segundo, CA: The Aerospace Press.

[27] Goddard Space Flight Center, NASA (2018). *CubeSat Form Factor Thermal Control Louvers - Passive thermal cooling for CubeSats.* Patent No.: 9862507. Retrieved from https://ntts-prod.s3.amazonaws.com/t2p/prod/t2media/tops/pdf/GSC-TOPS-40.pdf

[28] Isidoro Martinez. *Radiative view factors.* Retrived from http://webserver.dmt.upm.es/ isidoro/tc3/Radiation

[29] John R. Howell, University of Texas at Austin. *A Catalog of Radiation Heat Transfer Configuration Factors.* Retrieved from http://www.thermalradiation.net/tablecon.html

[30] European Cooperation for Space Standardization (15 February 2017). *ECSS-E-ST-33-01C Rev.1 - Space Engineering - Mechanisms* (pp. 28-38). Available from https://ecss.nl/standards/ecss-standards-on-line/active-standards/engineering/